ผลของการเติมโลหะต่อความชอบน้ำของฟิล์มบางไทเทเนียมไดออกไซด์ที่เหนี่ยวนำด้วยแสง

นายปิยพงษ์   พรมสาลี

EFFECT OF METAL LOADING ON PHOTO-INDUCED HYDROPHILICITY OF TITANIUM DIOXIDE THIN FILMS
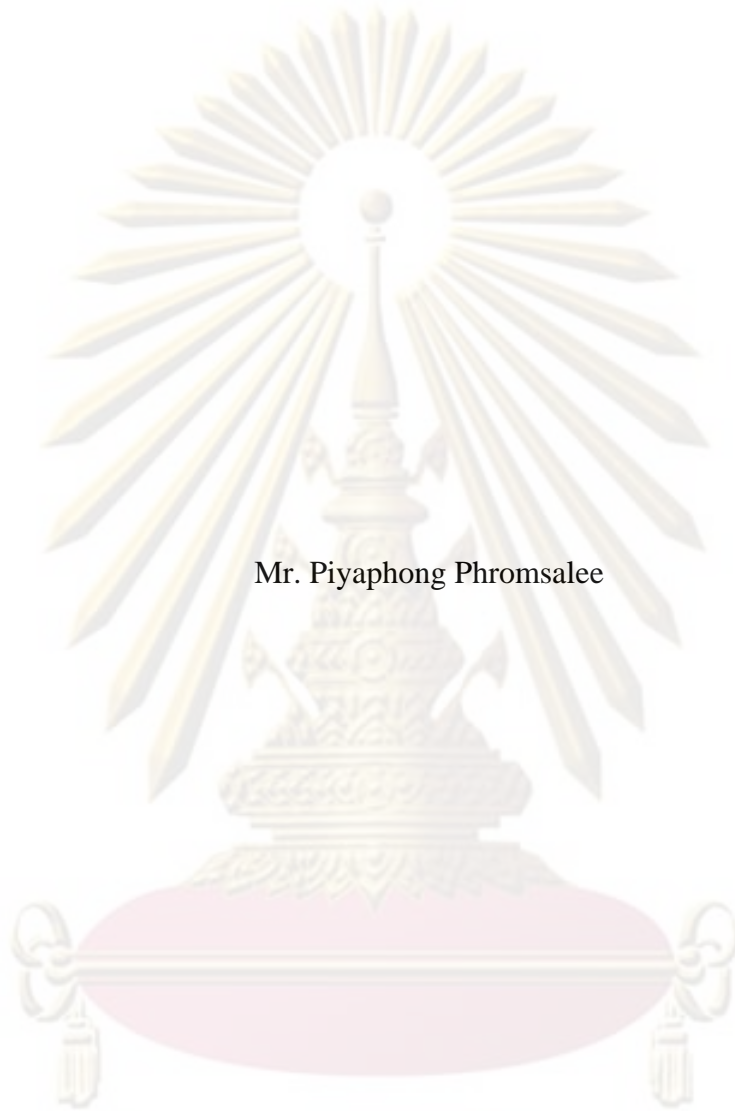
Mr. Piyaphong Phromsalee

A Thesis Submitted in Partial Fulfilment of the Requirements
for the Degree of Master of Engineering Program in Chemical Engineering
Department of Chemical Engineering
Faculty of Engineering
Chulalongkorn University
Academic Year 2008
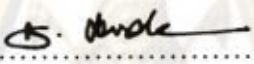
Thesis Title   EFFECT OF METAL LOADING ON PHOTO-INDUCED

HYDROPHILICITY OF TITANIUM DIOXIDE THIN FILMS

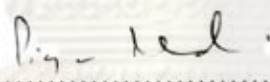By   Mr. Piyaphong Phromsalee
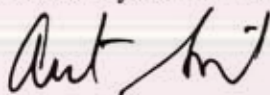
Field of study   Chemical Engineering

Advisor   Akawat Sirisuk, Ph.D.
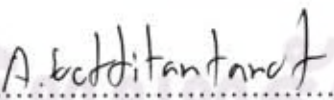
Accepted by the Faculty of Engineering, Chulalongkorn University in Partial
Fulfillment of the Requirements for the Master's Degree
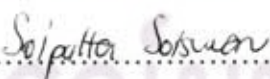
......................................Dean of the Faculty of Engineering

(Associate Professor Boonsom Lerdhirunwong, Dr.Ing.)

THESIS COMMITTEE

......................................Chairman

(Professor Piyasan Praserthdam, Dr.Ing.)

......................................Advisor

(Akawat Sirisuk, Ph.D.)

......................................Examiner

(Apinan Soottitantawat, Ph.D.)

......................................External Examiner

(Soipatta soisuwan, D.Eng.)

ปิยพงษ์   พรมสาลี   :   ผลของการเติมโลหะต่อความชอบน้ำของฟิล์มบางไทเทเนียม
ไดออกไซด์ที่เหนี่ยวนำด้วยแสง. (EFFECT OF METAL LOADING ON PHOTO-
INDUCED HYDROPHILICITY OF TITANIUM DIOXIDE THIN FILMS)
อ. ที่ปรึกษาวิทยานิพนธ์หลัก: อ.ดร.อัครวัต ศิริสุข, 106 หน้า.

ไทเทเนียมไดออกไซด์โซล (TiO_2) สังเคราะห์ด้วยวิธีโซลเจล จากนั้นเติมสารละลาย
ซิลเวอร์ ทังสเตน คอบเปอร์ หรือโมลิบดีนัมลงในไทเทเนียมไดออกไซด์โซลเพื่อเตรียมโลหะผสม
ไทเทเนียมไดออกไซด์โซลของซิลเวอร์ ทังสเตน คอบเปอร์ หรือโมลิบดีนัม แล้วเคลือบโซลที่ได้
บนแผ่นกระจกโดยใช้เทคนิคจุ่มเคลือบเพื่อเตรียมฟิล์มบาง จากนั้นนำฟิล์มไปเผาในที่อุณหภูมิ 350
องศาเซลเซียส เป็นเวลา 2 ชั่วโมง ความชอบน้ำของฟิล์มบางตรวจสอบโดยการวัดมุมสัมผัสของ
หยดน้ำบนพื้นผิวฟิล์มภายใต้การฉายแสงอัลตราไวโอเลต การเติมซิลเวอร์และทังสเตนลงใน
ไทเทเนียมไดออกไซด์ช่วยเพิ่มความชอบน้ำของฟิล์มบาง โดยฟิล์มไทเทเนียมไดออกไซด์ที่เติม
ซิลเวอร์ร้อยละ 3.0 ถึง 5.0 โดยโมล หรือเติมทังสเตนร้อยละ 1.0 ถึง 1.5 โดยโมล
ไม่เพียงมีความชอบน้ำดีที่สุดแต่ยังปรับปรุงความสามารถในการรักษาสภาพความชอบน้ำนั้นไว้
หลังจากการกระตุ้นด้วยแสงได้นานที่สุดอีกด้วย ทั้งนี้เนื่องจากการเติมซิลเวอร์และทังสเตนลงใน
ไทไทเนียมไดออกไซด์ช่วยยับยั้งการกลับมารวมตัวกันของอิเล็กตรอนและโฮลที่เกิดขึ้นหลังจาก
การกระตุ้นด้วยแสง ซึ่งสอดคล้องกับผลของโฟโตลูมิเนสเซนต์ ส่วนการเติมคอบเปอร์ (ร้อยละ 0.1
ถึง 5.0 โดยโมล) หรือโมลิบดีนัม (ร้อยละ 0.1 ถึง 1.0 โดยโมล) ไม่ช่วยปรับปรุงความชอบน้ำของ
ฟิล์มบาง เนื่องจากอิเล็กตรอนที่เกิดขึ้นหลังจากการกระตุ้นด้วยแสงถูกดักจับโดยคอปเปอร์ออกไซด์
หรือโมลิบดีนัมออกไซด์ แทนที่การเกิดออกซิเจนวาแคนซีบนพื้นผิวของไทเทเนียมไดออกไซด์
นอกจากนี้ทั้งคอบเปอร์ออกไซด์และโมลิบดีนัมออกไซด์เป็นสารที่ไม่มีความชอบน้ำ ดังนั้นการเติม
คอบเปอร์และโมลิบดีนัมลงในไทเทเนียมไดออกไซด์ จึงส่งผลให้ความชอบน้ำของฟิล์มบางลดลง

ภาควิชา	วิศวกรรมเคมี	ลายมือชื่อนิสิต	ปิยพงษ์ พรมสาลี	
สาขาวิชา	วิศวกรรมเคมี	ลายมือชื่อ อ.ที่ปรึกษาวิทยานิพนธ์หลัก		
ปีการศึกษา	2551			

5070350521: MAJOR CHEMICAL ENGINEERING

KEYWORDS: TITANIUM DIOXIDE / THIN FILM / HYDROPHILICITY / METAL LOADING

PIYAPHONG PHROMSALEE: EFFECT OF METAL LOADING ON PHOTO-INDUCED HYDROPHILICITY OF TITANIUM DIOXIDE THIN FILMS. ADVISOR: AKAWAT SIRISUK, Ph.D., 106 pp.

Titanium dioxide sol (TiO_2) was synthesized using a sol-gel method. Various amount of silver, tungsten, copper, or molybdenum precursor solution were added to TiO_2 sol to produce Ag-, W-, Cu-, or Mo-TiO_2 sol. Then the modified TiO_2 sol was coated on glass plates using a dip-coating technique to form the thin films. The as-prepared films were calcined at 350 °C for two hours. The hydrophilicity of the thin films was evaluated by measuring the contact angle of water droplet on the film surface under UV irradiation. Addition of silver or tungsten to TiO_2 enhanced hydrophilicities of the mixed oxide films. TiO_2 film containing 3.0-5.0 mol% silver or 1.0-1.5 mol% tungsten not only possessed the best hydrophilic properties but also improved their abilities to retain hydrophilicity after removal of UV irradiation. This was attributed to silver and tungsten inhibiting the recombination of photo-generated electrons and holes, which agreed with the results from photoluminescence spectra. Addition of copper (0.1-5.0 mol%) or molybdenum (0.1-1.0 mol%) to TiO_2 did not improve the hydrophilicity of the thin films because the photo-generated electrons were captured by metal oxide instead of creating surface oxygen vacancies on TiO_2 surface. Furthermore, neither CuO nor MoO_3 possessed hydrophilicity. An increase in the content of copper or molybdenum in TiO_2 worsened the hydrophilic property of the thin film.

Department : __Chemical Engineering__   Student's Signature : _Piyaphong Phromsalee_

Field of Study : _Chemical Engineering_   Advisor's Signature : _____

Academic Year : _____2008_____

ACKNOWLEDGEMENTS

CONTENTS

LIST OF TABLES

LIST OF FIGURES

CHAPTER I

INTRODUCTION

Titanium dioxide (TiO_2) is widely used in many applications such as photocatalyst for environmental purification, solar cells, pigment, UV absorber, gas sensor, catalyst support, self-cleaning, and anti-fogging surface, etc. As for TiO_2 thin films, there are actually two distinct photo-induced phenomena; the first one is the well-known photocatalytic process, which leads to the decomposition of organic pollutants in water and air to CO_2, H_2O, and other small organic compounds; the second one is the hydrophilic property, which occurs after TiO_2 surface is irradiated with UV light (Fujishima et al, 2000). Hydrophilic property of TiO_2 surface allows water to spread completely across the surface rather than remaining as droplets, which can be developed into self-cleaning and anti-fogging glasses and surfaces (Guan, 2005 and Yu et al., 2006). However, this property is not stable. The hydrophilic surface can return to hydrophobic state when being kept away from UV illumination for extended period of time.

The main problems of utilizing TiO_2 as a photocatalyst in photocatalytic process are the fast recombination rate of photo-generated electron-hole pairs, which lead to low photocatalytic activity, and the restriction of light absorption capability in visible region (Xin et al., 2007). In order to slow down the recombination rate and enhance the interfacial charge transfer efficiency, doping of transition metal ion into TiO_2 has been widely investigated. The transition metal including Fe^{3+} (Sonawane et al., 2005 and Xin et al. 2007), Ni^{2+} (Sharma et al., 2006), Co^{2+} (Iwasaki et al., 2000 and Bellardita et al., 2007), W^{6+} (Li et al., 2001; Bellardita et al., 2007 and Ke et al., 2008), Cu^{2+} (Li et al., 2004; Xin et al., 2008, and Xu et al., 2008), and Ag^+ (He et al., 2002 and Xin et al., 2005) have been proven to act as traps for photogenerated electron–hole pairs, thereby prolonging the lifetime of electrons and holes and improving photocatalytic activity of TiO_2 (Sharma et al., 2006). Nevertheless, only few researchers have reported the effect of metal doping on hydrophilicity although

there may be a close correlation between photocatalytic activity and hydrophilic property of TiO_2 (Guan, 2005).

Therefore, in this study various metals (i.e., Ag, W, Cu, and Mo) were added to TiO_2. The effects of metal loading on the hydrophilicity of thin films and their abilities to retain hydrophilic property after removal of UV irradiation were investigated. TiO_2 and metal-loaded TiO_2 sol were prepared by a sol-gel method and then were coated on glass plates using a dip-coating technique.

This thesis is arranged as follows:

Chapter II explains the basic information about TiO_2, principles and applications of photo-induced hydrophilic property and presents the literature reviews of previous works related to this research.

Chapter III describes the synthesis of TiO_2 and metal loaded-TiO_2 using a sol-gel process, preparation of the thin films by a dip-coating technique and characterization of the thin films.

Chapter IV presents experimental results and discussion.

Chapter V presents overall conclusions of this research and recommendations for future research.

CHAPTER II

BACKGROUND INFORMATION

2.1 Information on titanium dioxide

TiO_2 is an n-type semiconductor, which is widely used in many applications owing to its exceptional optical and electronic properties, strong oxidizing power, chemical stability, non-toxicity, good mechanical strength and inexpensive (Litter, 1999). TiO_2 exists in three crystallographic forms of anatase, rutile, and brookite (see Figure 2.1); anatase (tetragonal), generally processes a higher hydrophilicity and photocatalytic activity than the other types of TiO_2; rutile (tetragonal), mostly common in nature and tends to be more stable at higher temperatures, which has higher opacity, greater density and inertness than that anatase. Moreover, it is used as a convertible pigment in paints and dyes industry. (Jiang and Chen, 2004); and brookite (orthorhombic), is a metastable phase, which is scare and usually found only in minerals (Ohara et al., 2008). Moreover, it is difficult to prepare pure phase under laboratory condition.

(a)   (b)   (c)
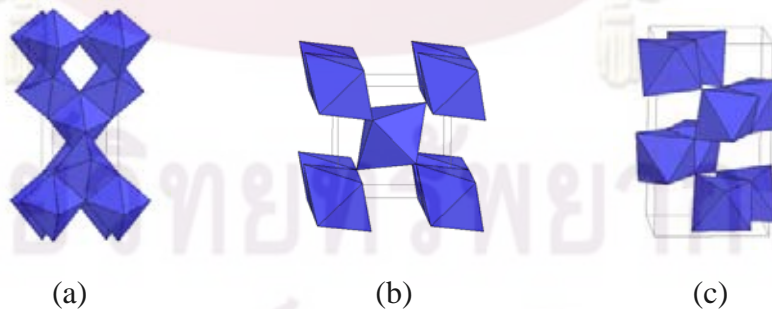
Figure 2.1 Crystal structures of titanium dioxide: (a) anatase (b) rutile and (c) brookite. (http://ruby.colorado.edu/~smyth/min/tio2.html)

2.2 Synthesis of titanium dioxide by a sol-gel method (Su et al., 2004)

The sol-gel process occurs in liquid solution of organometallic precursors such as titanium isoproproxide, tetraethyl orthosilicate and zirconium propoxide. The precursor undergoes hydrolysis and condensation reactions, and form sol according to Equations 2.1 to 2.3.

$$M-O-R+H_2O \longrightarrow M-OH+R-OH \qquad \text{(hydrolysis)} \qquad (2.1)$$

$$M-O-H+HO-M \longrightarrow M-O-M+H_2O \quad \text{(water condensation)} \quad (2.2)$$

$$M-O-R+HO-M \longrightarrow M-O-M+R-OH \text{ (alcohol condensation) } (2.3)$$
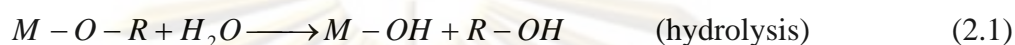
where M and R are metal atom and typically an alkyl group, respectively. The sol is made of solid particles of a diameter of few hundred nanometers suspending in a liquid phase. After that, the particles condense into gel, in which solid macromolecules are immersed in a liquid phase. Drying the gel at low temperature (25-100 ˚C) produces porous solid matrices or xerogels. To obtain a final product, the gel is heated. This heat treatment serves several purposes, i.e., to remove solvent, to decompose anions such as alkoxides or carbonates to give oxides, to rearrange of the structure of the solid, and to allow crystallization to occur.

Using the sol-gel method, one can easily control a stoichiometry of solid solution and a homogeneous distribution of nanoparticles and metal oxides. In addition, the metal oxides can be prepared easily at room temperature and high purity can be obtained.

2.3 Photo-induced hydrophilicity of titanium dioxide thin film

The primary process involving photocatalytic process occurs upon irradiation of a semiconductor. A semiconductor is characterized by an electronic structure, in which a valance band (vb) and a conduction band (cb) are separated by a band gap (Eg). The band gap defines the wavelength sensitivity of the semiconductor to

irradiation. A photon with energy higher than or equal to the band gap energy is absorbed by a semiconductor particle. Then an electron (e^-) from the valance band is promoted to the conduction band with simultaneous generation of an electronic vacancy or hole (h^+) in the valance band. This process is photoexcitation of electrons. Figure 2.2 shows the photocatalytic process occurring on an irradiated semiconductor particle. In metal, two types of charge carriers, electrons and holes, immediately recombine on the surface or the bulk of particle in a few nanoseconds and the accompanying energy is dissipated as heat. In a semiconductor such as TiO_2, however, the charge carriers survive for a longer period of time to allow themselves to be trapped in surface states where they can react with electron donor (D) or acceptor (A) species, which adsorbed on or closed to the surface of the particle (see Equations 2.4 to 2.7) (Litter, 1999). Subsequently, oxidation and reduction can be initiated.

$$TiO_2 \xrightarrow{\;h\upsilon\;} TiO_2(e^- + h^+) \qquad \text{(photoexcitation)} \qquad (2.4)$$

$$TiO_2(e^- + h^+) \longrightarrow TiO_2 + heat \qquad \text{(recombination)} \qquad (2.5)$$

$$TiO_2(e^-) + A \longrightarrow TiO_2 + A^- \qquad \text{(reduction)} \qquad (2.6)$$

$$TiO_2(h^+) + D \longrightarrow TiO_2 + D^+ \qquad \text{(oxidation)} \qquad (2.7)$$
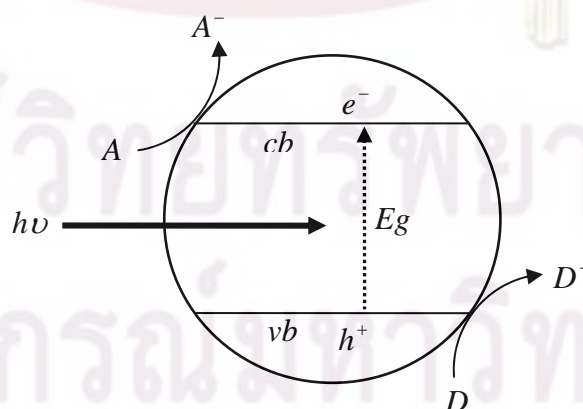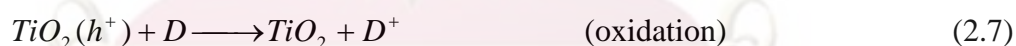
Figure 2.2 Photocatalytic process occurring on an illuminated semiconductor particle (Litter, 1999).

The hydrophilicity of TiO_2 film was actually discovered by accident work that was being carried out at laboratory of TOTO Inc. in 1995. It was found that, if TiO_2 thin film was prepared with certain percentage of SiO_2, it acquired superhydrophilic property with water contact angle of ~0° after UV irradiation. Photo-induced hydrophilicity is different process from the photocatalytic decomposition of organic contaminants. Many researches have been reported such as, strontium titanate ($SrTiO_3$), which has almost the same photocatalytic activity as to TiO_2 but not become hydrophilic surface after UV irradiation (Miyauchi et al., 2000) or WO_3, which shows photo-induced hydrophilicity but not exhibit photocatalytic activity (Miyauchi et al., 2002). Furthermore the hydrophilic surface of TiO_2 after UV irradiation consists of large numbers of closely spaced domains with sizes of several tens of nanometers, which reveled by atomic force microscopic observation (Sakai et al., 2001). Generation of such a domain structure cannot be explained by removal and adsorption of carbon contamination is the only reason causing the surface wettability change on the TiO_2 surface.

Earlier, the present authors considered that this highly hydrophilic conversion originated from the clean surface produced by the decomposition of the contaminants on surface through conventional photocatalytic process. However, after a large number of experimental results which did not suggest the conversion of hydrophilic surface by photocatalytic decomposition was taking place such as, (1) hydrophilic conversion of TiO_2 and $SrTiO_3$ films after applying oleic acid on surface. Before and after applied oleic acid, both TiO_2 and $SrTiO_3$ films had the contact angle about 20° and 70° respectively. After UV irradiation, the water contact angle of $SrTiO_3$ film decreased and reached to initial contact angle about 20°, which surface adsorbed oleic acid was decomposed. But for TiO_2 film, the contact angle decreased to 0°, which was lower than initial contact angle (Miyayushi et al., 2000), (2) treatment of TiO_2 surface by warm concentrated NaOH solution, which strains were completely removed but it still showed hydrophilic conversion after UV irradiation (Sun et al., 2001), (3) sonication of hydrophilic surface of TiO_2 film in pure water back to the original less hydrophilic one. As the hydrophilic surface was sonicated in pure water, the surface strain were removed and highly hydrophilic was enhanced (saki et al., 1998),

and (4) on highly hydrophilic surface, it was found that the reconversion rate in a cleaner pure oxygen atmosphere is much higher than that in ambient condition. If carbon contamination is the only reason that gives rise to an increase of the water contact angle, then it might be reasonable to consider that the hydrophilic-to-hydrophobic conversion rate in an ambient condition should be higher than that in pure oxygen due to the relatively high concentration of carbon containing contaminants in the former condition. However, the result is the reverse (Sun et al., 2001). So the authors came to the conclusion that alternate mechanism for hydrophilic conversion exist other than the removal of organic contaminants on the surface (Irie and hashimoro, 2005).

The mechanism of photo-induced hydrophilicity is proposed on the basis of the reconstruction of the surface hydroxyl groups which occurs by adsorption of water molecules on the photo-generated defective sites of TiO_2 under UV light irradiation, and reach to highly hydrophilic surface. The formation of defective sites on TiO_2 surface can be expressed according to Equations 2.8 and 2.9 (Yu et al., 2002).

$$Ti^{4+} + e^- \longrightarrow Ti^{3+} \tag{2.8}$$

$$O^{2-} + 4h^+ \longrightarrow O_2 + \square \quad \text{(oxygen vacancy)} \tag{2.9}$$
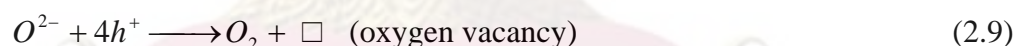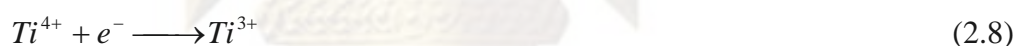
Figure 2.3 presents the mechanism of photo-induced hydrophilivity in TiO_2. When the TiO_2 surface is excited by UV illumination, photo-generated electrons are trapped at the surface of Ti sites as Ti^{3+} and immediately oxidized by adsorbed molecular oxygen, while the holes diffuse to TiO_2 surface, being trapping at lattice oxygen atoms to form O^- and be further oxidized by a second hole to form a neutral $O\bullet$ radical. The trapping of holes weaken the binding energy between Ti atom and the lattice oxygen atoms. Then two oxygen radicals are coupling and release as O_2 molecules, so the oxygen vacancies are created. Subsequently, water molecules can occupy these oxygen vacancies by dissociative adsorption to produce chemisorbed hydroxyl groups and then multiple layers of water molecules by Van der Waals forces and hydrogen bond (Fujishima et al., 2000; Lee et al., 2003 and Guan, 2005). The process gives rise to a hydrophilic surface. The longer the surface is illuminated with

UV light, the smaller the contact angle for water becomes and tendency to spread perfectly across the surface.

During long term storage in the dark place in air, the contact angle of water tends to increase up to certain saturated contact angle. This is ascribed to the gradual replacement of chemisorbed hydroxyl groups by oxygen from the air and the healing of surface defective sites, which return the surface geometric and electronic structures to the native TiO_2 surface (Wang et al., 1999). Consequently, the hydrophilicity is lost and the surface wettability changes from a hydrophilic state to hydrophobic state one. From the viewpoint of practicality and commercialization, it would be more valuable if the hydrophilicity of the TiO_2 films can remain for a long time, through the hydrophilicity could be fully recovered by illumination the TiO_2 surface again with UV light (Wang et al., 2000 and Yu et al., 2006).
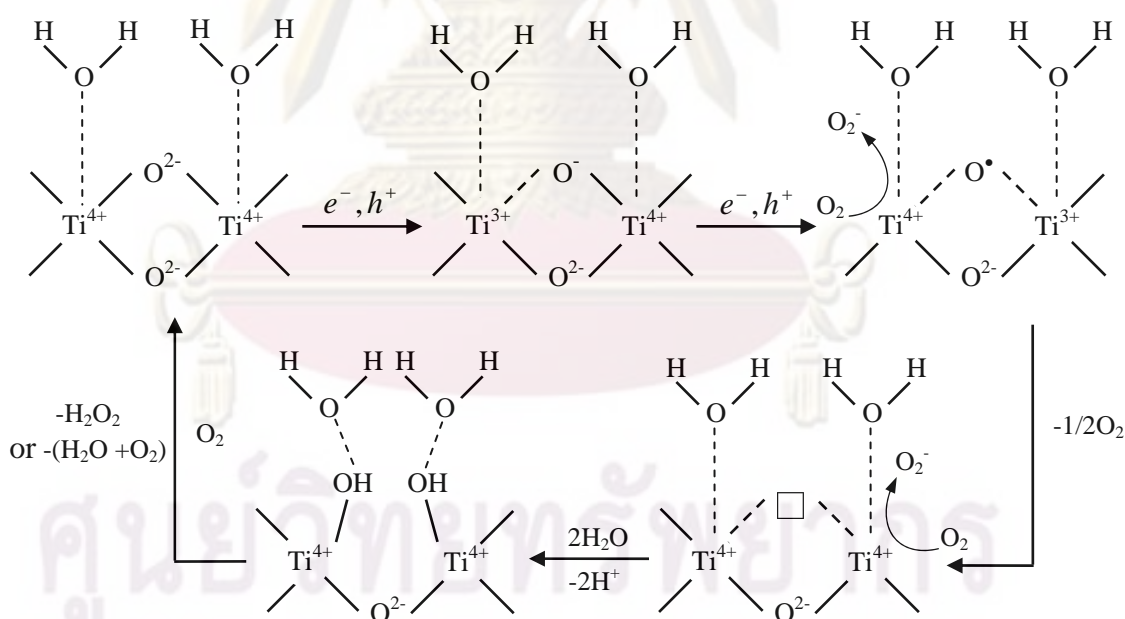
Figure 2.3 Mechanism of photo-induced hydrophilicity of TiO_2 film. ($\square$ denotes oxygen vacancy) (Sakai et al., 2001 and Saki et al., 2003)

2.4 Wettability and contact angle (De Gennes, 1985 and Irie et al., 2005)

Wettability is one of the most important on solid surface. The surface wettability is generally evaluated by the contact angle, which is the angle at which a liquid/vapor interface meets the solid surface. The contact angle is specific for any given system and is determined by the interactions across the three interfaces. Most often the concept is illustrated with a small liquid droplet resting on a flat horizontal solid surface (see Figure 2.4). Ideally, the droplet should be as small as possible because the force of gravity force, for example, can actually change the above-mentioned angle.

The theoretical description of contact angle arises from the consideration of a thermodynamic equilibrium between the three phases, namely, the liquid phase of the droplet (*L*), the solid phase of substrate (*S*), and the gas/vapor phase of the ambient (*V*). At equilibrium, the chemical potential in the three phases should be equal. It is convenient to frame the discussion in term of the interfacial energy or surface tension. The shape of the droplet is determined by the Young-Laplace Equation (see Equation 2.10) which, must be satisfied in equilibrium as follows in Equation 2.10.

$$\cos\theta = \frac{\sigma_{SV} - \sigma_{SL}}{\sigma_{LV}} \tag{2.10}$$

where θ is contact angle

σ_{SV} is surface tension between solid and vapor ambient atmosphere

σ_{SL} is surface tension between solid and liquid

σ_{LV} is surface tension between liquid and vapor ambient atmosphere
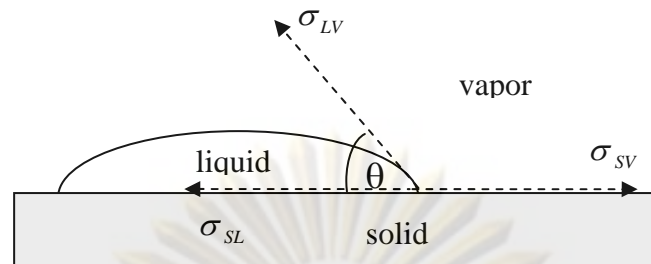
Figure 2.4 The force balance between the three surface tensions for determining the contact angle.

Young's equation is applicable only to an ideal surface, that is, homogeneous, rigid, insoluble and flat. However, real surfaces have surface roughness and surface heterogeneity. Wentzel modified Young's equation considering the surface roughness to obtain the Equation 2.11.

$$\cos\theta' = \gamma\cos\theta \tag{2.11}$$

where θ' is the apparent contact angle

γ is the surface roughness ratio between the actual surface area and the apparent surface area.

This equation indicates that the surface roughness enhances hydrophilicity of hydrophilic surface ($\theta < 90°$) and also enhances the hydrophobicity of hydrophobic surface ($\theta > 90°$).

The wettability of surface can be classified by the contact angle into four regions.

1. When $\theta < 5°$, water can spread completely over substrate surface. This state is called "superhydrophilic".

2. When $5° < \theta < 90°$, the surface allows the substrate to be wetted and the water film is form on its surface. This state is called "hydrophilic".

3. When $90° < \theta < 150°$, the substrate has little or no tendency to adsorb water and tend to bead on the surface. This state is called "hydrophobic".

4. When $\theta > 150°$, water droplets simply rest on the surface, without actually wetting to any significant extent. This state is called "superhydrohydrophobic".

2.5 Relationship between photocatalysis and hydrophilicity (Guan et al., 2005)

In spite of the different mechanisms of photocatalsis and hydrophilicity, the correlation between the two effects is obvious. The photo-induced hydrophilicity of the film closely relates to the photocatalytic removal of organic substances from the film surface. When more hydroxyl groups can be adsorbed on the surface due to hydrophilicity, the photocatalytic activity is enhanced. Therefore, hydrophilicity can enhance photocatalysis. On the other hand, the film surface can adsorb contaminated compounds, which tend to turn the hydrophilic surface into hydrophobic surface. Nonetheless, photocatalysis can decompose the organic compound deposited on the surface into H_2O, CO_2, and other small organic compounds to restore the hydrophilicity. As a result, photocatalysis can improve hydrophilicity and sustain this characteristic for a long time.
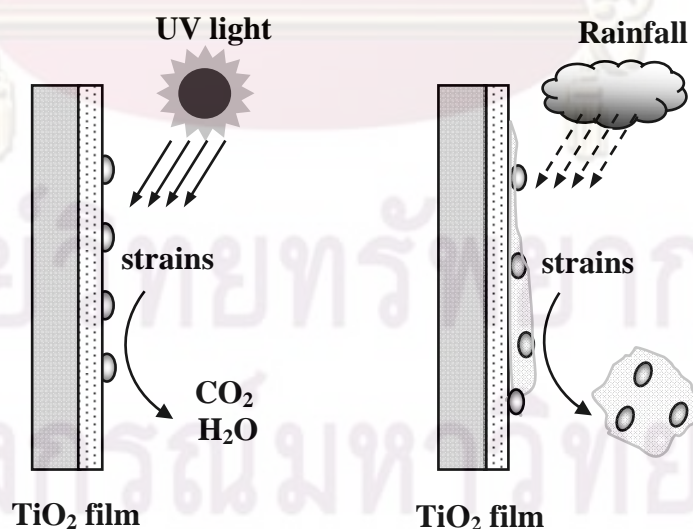
Figure 2.5 Relationship between photcatalytic and hydrophilic properties on TiO$_2$-coted surface. (Irie and Hashimoto, 2005)

2.6 Applications of hydrophilic property of TiO$_2$ film

2.6.1 Self-cleaning surface (Fujishima and Zhang, 2006; Fujishima et al., 2008)

Based on the photocatalytic and hydrophilic properties of TiO$_2$ surface, gradually adsorbed organic contaminates are decomposed by photocatalytic process, while self cleaning of contaminated-surface could be enhanced when the water, such natural rainfall, are applied to the surface, which water penetrated to the space between the strain and hydrophilic surface TiO$_2$ and washed off from surface. This technique is obviously of great value, since it can utilize freely available solar light or waste UV emission from fluorescence lamps, save maintenance cost and reduce the use of detergents. The best use of self-cleaning TiO$_2$ surfaces should be exterior construction materials, since these materials could be exposed to abundant sunlight and natural rainfall. Such materials, including tiles, glass, aluminium siding, plastic films, tent materials, cement, etc. It is not true that a superhydrophilic self-cleaning surface will never turn dirty, since the efficiency of self-cleaning surface was found to be dependent on the relative rate of contamination and decontamination, illumination of sun light and amount of rainfall, which TiO$_2$ photocatalyst can maintain the surface clean only when the photocatalytic decontamination rate is greater than that of contamination. But, it really trues that such a self-cleaning surface retard the rate of contamination.

2.6.2 Anti-fogging surface (Fujishima et al., 2008)

Fogging of the surface of mirrors and glasses occurs when moist air cools down on these surfaces, forming many water droplets. These droplets, ranging from micrometer to millimeter size, tend either to scatter light or simply to reflect or refract it randomly. On a highly hydrophilic surface, no water droplets are formed which spreads evenly across the surface. If the amount of the water is relatively small, the water layer becomes very thin and evaporates quickly. If the amount of water is large, it forms a sheet like-layer that also has high visual clarity. The first commercial application of this phenomenon has been for automobile slide-view mirrors. In

addition, it has marketed adhesive TiO$_2$-coated plastic films or TiO$_2$-coataining sprays for the conversion of existing mirrors.

2.6.3 Heat transfer and heat dissipation (Irie and Hashimoto, 2005 and Fujishima, 2008)

Superhydrophilic surfaces may improve the heat transfer accompanied by liquid-vapor phase transition. Takata and coworkers (2005) studied the heat transfer properties of superhydrophilic TiO$_2$ surfaces. They found that a TiO$_2$-coated Cu cylinder exhibited excellent heat transfer characteristics in the nucleated boiling regime, and its critical heat flux (a condition where liquid cannot rewet the heater wall because of the rate of vapor production impeding the liquid flow back to the hot surface) was about two times higher than that of the uncoated surface. They also compared the falling-film evaporation on a superhydrophilic surface with that on an ordinary surface which, water was sprayed on the heated surface through nozzles to form a water film. On the superhydrophilic surface, a stable water film was formed than those on an ordinary surface. Since the heat transfer rate increases for thinner water films, the superhydrophilic surface is expected to improve the performance of falling-film evaporators. These workers suggested that the superhydrophilic surface could be an ideal heat transfer surface and would be applicable to various heat transfer phenomena that are affected by surface wettability.

On the other hand, when water vapor pressure is lower than saturated vapor pressure, water evaporates, generating latent heat flux, accompanied by a cooling down of the surrounding atmosphere. Sprinkling a very small amount of water continuously onto the highly hydrophilic TiO$_2$ surface, effective cooling can be achieved. A very thin water layer with a thickness of approximately 0.1 mm can cover all of the highly hydrophilic TiO$_2$ material, even though it stands vertically, if only a small amount of water is supplied continuously. This technology is applicable to the building of walls. The TiO$_2$-coated walls become highly hydrophilic through exposure to solar light and thus the sprinkled water will form a thin layer and be evaporated efficiently from the surface. The evaporation of the water generates latent heat flux, which cools the building surfaces and the surrounding atmosphere. The cooling effect

reduces the usage of air conditioning, saves on energy consumption, and reduces the artificial heat emission.

2.7 Effects of various parameters on hydrophilicity of titanium dioxide

This section discusses the effects of several parameters on hydrophilicity of TiO_2. The parameters include TiO_2 phase structure, surface hydroxyl group, specific surface area and surface roughness, surface defective site, recombination of electron and hole, band gap energy and surface acidity.

2.7.1 Effect of titanium dioxide phase structure

Yu and coworkers (2002a) studied light-induced superhydrophilicity of mesoporous TiO_2 thin films. Mesoporous TiO_2 ($MTiO_2$) and TiO_2 thin films were prepared by a modified reverse micellar and a sol-gel method, respectively, followed by dip coating on fused quartz substrate. Both $MTiO_2$ and TiO_2 films were calcined at 500 °C and 900 °C in order to obtained anatase and rutile phase structure, respectively. $MTiO_2$ and TiO_2 films in anatase phase structure became hydrophilic faster than $MTiO_2$ and TiO_2 films in rutile phase structure did. This can be explained by the longer life time of photo-generated electrons and holes in anatase phase structure, resulting in the formation of more oxygen vacancies. Furthermore, the content of hydroxyl groups on the surfaces of $MTiO_2$ and TiO_2 films in anatase phase structure was greater, so their polarity and hydrophilicity was greater.

Yu and coworkers (2002b) studied the effect of calcination temperatures on photo-induced superhydrophilicity of mesoporous TiO_2 thin films, which were prepared on fused quartz substrate by a sol-gel method, followed by dip coating. Mesoporous TiO_2 thin films were calcined at 500, 700, and 900 °C in order to obtain anatase, mixture of anatase and rutile, and rutile phase structure, respectively. The film that was calcined at 700 °C became hydrophilic at the faster rate because the film was composed of anatase and rutile phases, which was beneficial in enhancing the transfer of photo-generated electrons from the anatase to the rutile phases, thereby reducing the recombination of electrons–holes in anatase phase.

Moreover, the films that were calcined at 700 °C possessed high content of surface hydroxyl group (compared with the films calcined at 900 °C) and high surface roughness (compared with the films calcined at 500 °C).

2.7.2 Effect of hydroxyl groups on surface

Yu and Zhao (2001) prepared TiO_2 thin films by a sol-gel method, followed by coating on soda lime glass substrate. Then the films were soaked in 0.2 M HCl for four days. The thickness of TiO_2 thin films did not affect the water contact angle. Results from XPS analysis indicated that the content of surface hydroxyl groups of TiO_2 thin films after HCl treatment increased and led to a decrease in the water contact angle or enhanced hydrophilicity. The increase in surface hydroxyl groups after the treatment was attributed to the proton-exchange action at the interface of Na in nascent TiO_2 layer (from soda lime glass substrate) with proton (H^+) from HCl.

Yu and coworkers (2001) added polyethylene glycol (PEG) to the precursor solution during the preparation of porous TiO_2 films via a sol-gel method on soda lime glass substrate. When amount of PEG increased, pore size and specific surface area of TiO_2 increased, leading to an increase in hydroxyl adsorbed content on TiO_2 surface. The hydrophilicity of the film was enhanced because of increasing van der Waals forces and hydrogen bond interaction between water and hydroxyl groups. However, when the amount of PEG exceeded 0.5 g, the hydroxyl content did not change significantly, and the contact angle remained unchanged.

2.7.3 Effect of band gap energy

Jiang and Chen (2004) studied the hydrophilic properties of V_2O_5–TiO_2 thin films, which were prepared on glass substrates by a sol-gel processing and followed dip-coating method. The results showed that the crystallite size of anatase TiO_2 decreased as increased vanadia contents from 46 nm (TiO_2) to 20 nm (1.81 mol% V_2O_5). Before irradiation, the water contact angles of the films were about 34°. After illuminated by sunlight for 40 minutes, the water contact angles of V_2O_5–TiO_2

films drastically fell to 5°, but TiO_2 film that remained unchanged. The improvement of hydrophilicity was attributed to doping of vanadium ion could produce a visible-light response which may change the band gap energy between the conduction and valence bands. Thus, it acquires the capability of absorbing visible light. Moreover, smaller crystal size of TiO_2 after V_2O_5 adding, photo-generated electrons could easier to move to the surface of film with smaller crystal size and produce more oxygen vacancies and defective sites.

Weng and coworkers (2005) investigated the effect of Fe doping on superhydrophilicity of TiO_2 thin films. TiO_2 and Fe-doped TiO_2 thin films were prepared by spray pyrolysis deposition technique on glass substrate. The hydrophilicity of thin films was evaluated by the contact angle of water under illuminated of Xenon lamp. The doping of Fe enhanced the hydrophilicity of the film, which was attributed to the decrease in the band gap energy of the TiO_2 and, consequently, the increase in ability to absorb photon in visible spectrum.

Li and coworkers (2007) studied the effects of vanadium incorporation on hydrophilic properties of TiO_2 film. $Ti_{1-x}V_xO_2$ (x=0.05-0.2) films were prepared by a sol–gel method and followed dip-coating. After daylight illumination, the contact angle decreases greatly with increasing of the x values, which $Ti_{1-x}V_xO_2$ films with x=0.1–0.2 showed super-hydrophilic property. The increasing of surface roughness, lattice distortion that was caused by partial substitution of V^{4+} ions for Ti sites and V-incorporation narrows band gap of $Ti_{1-x}V_xO_2$ were beneficial to the super-hydrophilicity.

2.7.4 Effects of defective site and inhibition of recombination of photo-generated electrons and holes

Jiang and Gao (2002) investigated the effects of Fe doping on photo-induced hydrophilicity of TiO_2 thin films. TiO_2 and Fe-doped TiO_2 thin films were prepared by a sol-gel method followed dip coating on soda lime glass substrates. The best hydrophilicity was achieved with TiO_2 film that was doped with 5 mol% Fe.

Increasing the amount of Fe doping reduced the hydrophilicity of the film because Fe_2O_3 itself did not exhibit hydrophilicity. An enhancement in hydrophilicity of TiO_2 surface was related to the preferential adsorption of water on the defective site on TiO_2, which increased with Fe doping. Furthermore, photo-generated electrons in the doped film accumulated in the conduction band of Fe_2O_3 whereas holes accumulated in the valance band of TiO_2 effectively. Therefore, the recombination of electrons and holes was retarded and the hydrophilicity was greatly enhanced.

Lee and coworkers (2003) investigated the TiO_2 thin films that were doped with Al, W, and Al + W (1:1) in order to make the photoactivity of the surface suitable for hydrophilicity. TiO_2 thin films were prepared using the dip-coating method on soda lime glass and quartz. Doping of Al + W had the highest resistance to conversion from hydrophilic to hydrophobic state with contact angle of water remaining at 25°. The original hydrophilic state was restored within three hours with contact angle of water at 5°. From XPS analysis, the concentration of Ti^{3+} compared with Ti^{4+} in undoped, Al-doped, W-doped, and Al + W co-doped were 58.63%, 46.45%, 57.19%, and 63.81%, respectively. The concentration of Ti^{3+} on TiO_2 surface was a major factor influencing hydrophilicity. The same trend was observed in both soda lime glass and quartz substrate. Furthermore, hydrophilicity of TiO_2 thin films also depended on traps for electrons or holes and surface acidity.

Du and coworkers (2005) investigated the effects of Mo doping on hydrophilicity of TiO_2 thin films which were induced by high temperature annealing. TiO_2 and Mo-doped TiO_2 thin films were prepared by a sol-gel method and coated on soda lime glass substrates. After calcination at 400 °C for one hour, all the Mo-doped films showed relatively smaller water contact angle than pure TiO_2 film did. The 0.75 wt% Mo-doped TiO_2 film exhibited superhydrophilicity. Regarding the effect of heating time at 400 °C, the 0.75 wt% Mo-doped TiO_2 film reached the contact angle of zero after half an hour, while the contact angle for other films were below 15° but never reached zero even when heating time was increased. Doping of Mo has dual effects on hydrophilicity of TiO_2 films. On the one hand, the number of defect site (Ti^{3+}) increased with Mo doping. As a result, water molecules could occupy those

oxygen vacancies to produce surface hydroxyl groups and make the surface hydrophilic. On the other hand, MoO_3 itself does not exhibit hydrophilicity, so hydrophilicity decreased when the doping content exceeded 0.75 wt%.

Yu and coworkers (2006) studied an enhancement of photo-induced superhydrophilicity of TiO_2 thin films by Fe doping. Fe-doped TiO_2 thin films were prepared on soda lime glass pre-coated with SiO_2 layer by a sol-gel method, followed by dip coating. TiO_2 thin films that were doped with Fe at 0.05-0.2 atomic% showed the best photo-induced superhydrophilicity. This may be due to the fact that a small amount of Fe^{3+} ions acted as traps for both photo-generated electrons and holes and inhibited the recombination of electrons and holes. A lowering of hydrophilization rate was expected when the amount of Fe became too large because Fe mainly acted as recombination centers. When being stored in the dark, all Fe-doped films exihibted slow conversion rate from hydrophilicity to hydrophobicity than pure TiO_2 film because Fe-doped films not only contained highly surface hydroxyl group content but also small crystallite size, favoring the adsorption of water molecules and reducing the rate of conversion from hydrophilic to hydrophobic state.

Sharma and coworkers (2006) studied the effects of Ni doping on photo-inducined hydrophilicity of TiO_2 thin films. Pure and Ni-doped TiO_2 thin films were prepared by a sol-gel method, followed dip coating on soda glass substrates. Pure TiO_2 film reached a contact angle of zero after one hour of illumination. For Ni-doped films, 10 mol% Ni-doped films exhibited the best hydrophilicity by reaching contact angles of zero after 20 minutes of illumination. An enhancement in hydrophilicity of TiO_2 surface was related to the preferential adsorption of water on the defective site on TiO_2, which increased with Ni doping. Furthermore, the recombination of electrons and holes was retarded and the hydrophilicity was greatly enhanced.

Yuan and coworkers (2007) studied the effects of doping of Fe and Cr on hydrophilic properties of anatase TiO_2 films. The TiO_2 films were prepared by a modified sol-gel method and were doped by phodeposition of Fe_2O_3 and Cr_2O_3.

Before illumination, the Fe- and Cr-doped films had smaller contact angle (30° and 35°, receptively) than pure TiO_2 film (60°). After three hours of UV illumination, the contact angle reached 0° for Fe- and Cr-doped films and reached 28° for pure TiO_2 film. That is, the doped films exihibited good hydrophilicity. The improvement in hydrophilicity was a result of the electrons reacting with lattice metal ions (Ti, Fe, and Cr) to form defective site.

2.8 Effect of metal loading to TiO_2 on photocatalytic activity of titanium dioxide

Li and coworkers (2001) studied photocatalytic activity of tungsten-doped TiO_2 which, were prepared by a sol-gel method. The photoactivity was evaluated by photodegradation of methylene blue under visible light irradiation. The activity of tungsten-doped TiO_2 was significantly higher than that of pure TiO_2. The optimal content of WO_x in TiO_2 was found to be 3 mol%. In small amount, doping of tungsten oxide into TiO_2 could hinder the recombination of photo-generated electrons and holes. On the other hand, when the content of tungsten oxide was higher than its optimal amount, tungsten oxide would become a recombination center instead. Furthermore, doping of tungsten oxide into TiO_2 could shift the light absorption band from near UV range to the visible range.

Rampaul and coworkers (2003) reported the photocatalytic activity of titania and tungsten-doped TiO_2 which were prepared by a sol-gel method, followed dip coating on glass substrates. The photoactivity of the films was measured by photodegradation of stearic acid on the film surface. The most active photocatalyst was the 2% tungsten doped TiO_2 film with three coats owing to WO_3 acting as an effective separation center for the electrons and holes, resulting in the photo-generated electron being transferred to the surface rather than undergoing bulk recombination.

Ke and coworkers (2008) studied the photocatalytic activity of WO_3/TiO_2 nanocomposite particles, which were prepared by a hydrothermal method and then were calcined a temperature in the range of 450-900 °C. The activity for RhB photodegrdation of equimolar WO_3/TiO_2 composite that was calcined at 550 °C was

significantly higher than that of pure TiO_2 and just slightly lower than that of Dgussa P25. This may be attributed to the more efficient separation of photo-generated charge carriers, light absorption and higher surface acidity.

Tian and coworkers (2008) studied phocatalytic activity of W-doped TiO_2 photocatalyst. Nanosized of W-TiO_2 photocatalyst were prepared by a hydrothermal method and their photocatalytic activity was evaluated by photodegradation of methyl orange in aqueous solution. The results showed that the photocatalytic activities of W-doped TiO_2 increased as the synthetic temperature was increased from 120-180 °C, but decreased significantly when further to 210 °C. The main reason may be attributed to the influence of surface area, the crystallization and aggregation of crystallites. Moreover, TiO_2 that containing 2.0 mol% and was prepared at synthetic temperature of 150 °C obtained the highest photcatalytic activity because the doping of tungsten helps in trapping of photo-generated electrons. So, the charge recombination was inhibited. However, tungsten could ac as recombination center for electron-hole pairs at too high loading.

He and coworkers (2002) investigated the effects of Ag doping on the microstructure and photocatalytic activity of TiO_2 films, which were prepared by a sol-gel method. With a suitable amount of 2-4 mol%, doping of Ag effectively increased the photocatalytic activity of TiO_2 films. This can be explained in two reasons; firstly, a decrease in anatase grains size and an increase in specific surface area of TiO_2 films. Secondly, an enhancement in the separation of charge pairs and inhibit of their recombination by Ag dopant. On the other hand, when doping of Ag exceeded 2-4 mol%, holes in the interfacial region of TiO_2 films may be trapped by Ag particles with relatively negative charge, so photocatalytic activity of Ag-TiO_2 was depressed.

Xin and coworkers (2005) studied photocatalytic activity of Ag-TiO_2 nanoparticle films. Ag-TiO_2 nanoparticles were synthesized by a sol-gel method and then were prepared in form of organic pastes before fabricated on ITO glass by means of doctor-blade. Photocatalytic activity of Ag-TiO_2 nanoparticle films was evaluated

by photocatalytic degradation of rhodamine B. The highest photocatalytic activity was observed at TiO_2 that containing 3 mol% Ag. This was attributed to appropriately doped and deposited Ag species on the surface of TiO_2 can capture the photo-generated electrons and holes. However, when the content of Ag exceed 3 mol%, the amount of active sites reduced and excessive Ag dopant can overlie on the TiO_2 surface, which lead to decreasing in photocatalytic activity.

Xin and coworkers (2005) studied the simultaneous doping and deposite Ag on photocatalytic activity of TiO_2, which Ag-TiO_2 catalysts were prepared by a sol-gel method. Photocatalytic activity of Ag-TiO_2 was investigated by photocatalytic degradation of rhodamine B solution. The PL and SPS intensities of Ag-TiO_2 photocatalysts were decreased with increasing the Ag content, indicating that the Ag dopant could effectively inhibit the recombination of the photogenerated electrons and holes. The appropriate content of Ag (about 3-5 mol%) could greatly enhance the activity of the photocatalysts. However, the active sites for capturing the photogenerated electrons reduced, while the Ag content exceeded 5 mol%.

Li and coworkers (2004) studied photocatalytic activity of TiO_2-Cu_2O particles, which were prepared by a novel electrochemical method and their photocatalytic activity was tested by photodegradation of brilliant red dye solution. The results were found that the catalytic efficiency increased by Cu_2O depositing on TiO_2 but it decreased at higher Cu_2O loadings, which the highest degradation was obtained for the composite containing 3wt% Cu_2O. This can be explained by Cu_2O can accelerate the transferring of electrons to adsorbed oxygen, which be the rate liming step in photocatalysis. Thus, the recombination of electrons and holes was decrease.

Xia and coworkers (2008) studied the effect of copper loading on photocatalytic activity of rutile TiO_2 which were prepared by a sol-gel method. Photoactivity of Cu-TiO_2 was tested by degradation of aqueous brilliant red X-3b solution. TiO_2 that containing 2% copper showed the best photocatalytic activity, which was 3 times that undoped rutile TiO_2. This was attributed to the decreasing in

the recombination of electrons and holes on TiO_2 surface. Because Cu^{2+} is an effective acceptor for electrons, it contests for electrons with the holes. However, excessive copper was deposited on TiO_2, more $Cu(OH)^{2+}$ would be formed. $Cu(OH)^{2+}$ had a greater adsorption to the incidence light. This high adsorption decreased the light energy irradiating on the surface of TiO_2 and the removal efficiency of X-3B was decreased.

Xin and coworkers (2008) studied the effect of Cu-doped TiO_2 nanoparticles on photocatalytic activity, which were prepared by a sol-gel method. The 0.06 mol% Cu-TiO_2 that was calcined at 400 °C for four hours showed the highest RhB degradation rate because the appropriate amount of oxygen vacancies and doped Cu effectively captured the photo-generated electrons, so the recombination of the electrons and holes was inhibited. At high Cu doping (> 0.06 mol%), the excessive oxygen vacancies and Cu species became the recombination centers of photo-generated electrons and holes. Furthermore, at high Cu doping, excessive p-type Cu_2O also reduced photocatalytic activity of Cu-TiO_2 photocatalyst.

Xu and coworkers (2008) studied copper-deposited TiO_2 photocatalysts, which TiO_2 powders were prepared by a sol-gel method and followed deposition of copper (0-0.32 mol%) on TiO_2 surface by photoreduction method. The photocatalytic activity of Cu_2O-TiO_2 was evaluated by photodegradation of methylene blue under UV light irradiation. The results from XPS and AES revealed that all copper existed in the Cu(I) state. The highest photocatalytic degradation was obtained for 0.16% Cu_2O–TiO_2, this was attributed to Cu_2O can trap electrons and transferred to the surrounding adsorbed O_2, while the holes oxidize OH^-, H_2O, or the organics, and thereby prevent the electron–hole recombination. Thus, the photocatalytic activity of methylene blue was enhanced. However, when copper-deposited content reached to 0.32%, the photocatalytic activity was lower than that TiO_2. Because, the excessive of Cu_2O deposited on TiO_2 may screen the surface of TiO_2 from UV light.

CHAPTER III

MATERIALS AND METHODS

3.1 Chemicals

The details of chemicals used in this study are listed in Table 3.1

Table 3.1 List of chemicals were used in this studied.

Chemicals, Purity	Manufacturers
Titanium isopropoxide, 97 %	Sigma-Aldrich
Nitric acid, 69-70 %	J. T. Baker
Hydrofluoric acid, 49 %	QRëC^{TM}
Silver nitrate, 99+ %	Sigma-Aldrich
Ammonium metatungstate, 99.98 %	Sigma-Aldrich
Copper nitrate, 98-103 %	Fluka
Ammonium molybdate, 99.98 %	Sigma-Aldrich
Ethanol, 99.9 %	Merk
Acetone, 99.5 %	QRëC^{TM}

3.2 Preparation of the thin films

This section describes the synthesis of TiO_2 and metal loaded-TiO_2 sol using a sol-gel processes and preparation of the thin films by a dip-coating technique.

3.2.1 Preparation of TiO$_2$ sol

Titanium dioxide sol was synthesized using a sol-gel process, and titanium isopropoxide was employed as a precursor. Firstly, 7.33 mL of 70% nitric acid was added to 1000 mL of distilled water. While the acidic solution was stirred, 83.5 mL of titanium isopropoxide was slowly added. After that, the white suspension was immediately occurred. The suspension was continuously stirred at room temperature for about 3 days until clear sol was obtained. The sol was placed in dialysis tubing (cellulose membrane, Spectrum Laboratories Inc, USA) and then was submerged in distilled water using a ratio of 100 mL of sol per 700 mL of distilled water. The water was changed daily until the pH of permeate reached to 3.3. The resulting product was dialyzed TiO$_2$ sol which was kept at low temperature.

3.2.2 Preparation of metal-loaded TiO$_2$ sol

The amount of metal in the sample was in a term of a molar percentage of metal. The concentration of TiO$_2$ particles in the sol was obtained after TiO$_2$ sol was dried at 110 °C for 24 hours and calcined at 350 °C for two hours.

To prepare Ag-TiO$_2$ sol, the desired amount of silver nitrate was dissolved in 10 mL of deionized water and was then added dropwise to 140 mL of TiO$_2$ sol (pH 3.3) under vigorous stirring for one hour. The amount of silver added was in the range of 0.1-5.0 mol% silver.

To prepare W-TiO$_2$ sol, the pH of TiO$_2$ sol was adjusted to 1.0 by 1 M nitric acid. The desired amount of 0.2 M ammonium metatungstate solution (pH 2.5) was added dropwise to 140 mL of TiO$_2$ sol under vigorous stirring and the stirring continued for six hours. The amount of tungsten added was in the range of 0.1-1.5 mol% tungsten.

To prepared Cu-TiO$_2$ sol, the pH of TiO$_2$ sol was adjusted to 2.5 by 1 M nitric acid. The desired amount of 0.2 M copper nitrate solution (pH 2.5) was added dropwise to 140 mL of TiO$_2$ sol under vigorous stirring and the stirring

continued for one hour. The amount of copper added was in the range of 0.1-5.0 mol% copper.

To prepared Mo-TiO$_2$ sol, the pH of TiO$_2$ sol was adjusted to 2.0 by 1 M nitric acid. The desired amount of 0.2 M ammonium molybdate solution (pH 2.5) was added dropwise to 140 mL of TiO$_2$ sol under vigorous stirring and the stirring continued for two hours. The amount of molybdenum added was in the range of 0.1-1.0 mol% molybdenum.

For a comparison the pH, TiO$_2$ sol without metal loading was adjusted to the same value for each metal. The sol was dried and the powder was fired in order to obtain the reference samples.

3.2.3 Preparation of TiO$_2$ and metal-loaded TiO$_2$ thin films

TiO$_2$ and metal loaded-TiO$_2$ thin films were coated on soda lime glass plates (Menzel-Glaser, Germany) using a dip-coating technique. Prior to coating, glass plates were cleaned with a detergent solution in an ultrasonic bath for 30 minutes, and were washed with ethanol and then acetone. The glass plates were submerged in the sol and were held for 5 minutes. Then a motor withdrew the plates at a speed of 3.67 cm/min. The as-prepared films were calcined in a box furnace under stagnant air at 350 °C with a heating rate of 10 °C/min for two hours. The as-calcined films had a hydrophilic surface with a water contact angle of ca. 5°. Before further experiment, the films were stored in the dark place for four weeks in order to increase the water contact angle on the surface.

3.3 Characterization of the thin films

In order to determine physical and chemical properties of the films, various characterization techniques were employed and the results were discussed in this section.

3.3.1 X-ray diffractometry (XRD)

XRD was employed to identify crystal phase and crystallinity of sample. The equipment was a SIEMENS D5000 X-ray diffractometer with Cu Kα radiation using Ni filter and operating at 20 kV and 20 mA. The amount of the sample used was calculated in order to obtain the same amount of TiO_2 in each sample. The diffraction patterns were scanned in the 2θ range of 20-80° with a resolution of 0.02°. The average crystallite sizes of TiO_2 were calculated by Debye-Sherrer's formula from the line broadening of anatase (110) peak according to Equation 3.1

$$D = \frac{K\lambda}{\beta\cos\theta} \qquad\qquad (3.1)$$

where D is crystallite size (Å)

      K is crystallite shape factor (0.9)

      λ is X-ray wavelength (1.5418 Å for Cu K_α)

      θ   is the diffraction angle of crystal plane (degree)

      β is X-ray diffraction broadening (radian)

3.3.2 X-ray photoelectron spectroscopy (XPS)

XPS surface analysis was performed using a Kratos Amicus X-ray photoelectron spectroscope. The XPS spectra was obtained using Mg Kα X-ray source at 20 mA and 10 keV with a resolution of 0.1 eV. The operating pressure was approximately 5×10^{-6} Pa. A wide-scan survey spectrum was collected for each sample in order to determine the elements present on surface. All binding energies were calibrated for the correction of charging shift with C 1s photoemission peak at 284.6 eV. Photoemission peak area was determined after smoothing and background subtraction using a linear routine. Deconvolution of complex spectra were performed by fitting with Gaussian (70%)-Lorentzian (30%) shape using VISION 2 software equipped with the XPS system.

3.3.3 Inductively coupled plasma optical emission spectroscopy (ICP-OES)

The metal content in a sample was measured with a Perkin Elmer Optima 2100 DV spectrometer. To digest the samples, approximately 0.01 grams of the sample was dissolved with 8 mL of 49% hydrofluoric acid in a plastic beaker. The mixture was stirred for two hours and then diluted to 100 mL with deionized water in a plastic volumetric flask. Blank sample was prepared from a solution of 49% hydrofluoric acid that underwent the same dilution procedure as the sample.

3.3.4 Nitrogen physisorption

Specific surface area was measured by nitrogen adsorption in a continuous flow method at liquid nitrogen temperature using Micromeritics ChemiSorb 2750 Pulse Chemisorption System instrument. A mixture of 30 vol% N_2 in helium was employed as the carrier gas. Before each experiment, approximately 0.2 gram of samples was placed in a glass tube and was heated at 200 °C for one hour under helium gas with a flow rate of 15 mL/min to remove moisture.

3.3.5 Atomic force microscope (AFM)

The surface morphology and roughness of the film sample was characterized using a MultiMode atomic force microscope from Digital Instruments, which operated in the tapping mode at room temperature. AFM analysis permitted the quantification of the roughness in terms of the root mean square values (RMS).

3.3.6 UV-Visible spectroscopy (UV-Vis)

The light absorption characteristics of the films were measured using a lampda 650 UV–Vis spectrophotometer from Perkin Elmer in transmittance mode. The transmission spectra were scanned in the range of 300–700 nm with a step size of 1 nm. A clean glass plate was used as a background for reference.

3.3.7 Temperature-programmed desorption (NH₃-TPD)

Temperature programmed desorption (TPD) using NH_3 as a probe molecule was performed by a Micromeritic ChemiSorb 2750 automated system attached with ChemiSoft TPx software. The amount of NH_3 adsorbed on the surface was determined by a thermal conductivity detector. Approximately 0.1 gram of a sample was put in a quartz tube, which was placed in a temperature-controlled furnace. Helium gas was fed through sample at a flow rate of 15 mL/min. The sample was heated to 350 °C with a heating rate of 10 °C/min and the temperature was held for two hours to remove moisture. Then the sample was cooled down to 30 °C. After that, 15 vol% NH_3 in helium was fed through sample at a flow rate of 15 mL/min instead of helium, and the flow was held for one hour. Subsequently, helium gas was fed through the sample for two hours. Finally, the sample was heated from 30 °C to 600 °C with a heating rate of 10 °C/min. The signal from this step was recorded every one second.

3.3.8 Photoluminescence spectroscopy (PL)

To study the recombination behavior of photo-generated electron and holes, photoluminescence spectra were carried out at room temperature by a Perkin Elmer LS55 fluorescence spectrophotometer using a Xenon lamp as an excitation light source. The sample (0.14 g) was compressed in a holder. The scan was performed in the range of 350-550 nm using an excitation wavelength of 300 nm with emission and excitation slit widths of 5.0 nm.

3.3.9 Photo-induced hydrophilicity of thin films

The hydrophilicity of the films was evaluated by measuring the contact angle of a water droplet on the film surface by a contact angle meter (TANTEC Inc., USA). Two backlight fluorescence bulbs (15 W PHILIPS, Thailand) were used as a light source with average light irradiance of 0.67 mW/cm^2. The distance between a light source and the film surface was 15 cm. To measure the contact angle, the film was placed on a state. Then the state was raised to bring the film into contact with a

water droplet (approximately 0.3 μL). After that, the CCD video camera captured the picture of a water droplet on the film surface. The contact angle was calculated using trigonometry formula with TANTEC program. Five points of water droplet were place in different positions on the film surface and used as average contact angle. To study the ability to retain the hydrophilic properties of the films after removal of UV irradiation, the films were kept in the dark place and take out to measurement contact angle at any times.

3.3.10 Temperature programmed reduction (TPR)

To study the reduction behavior of a sample, temperature programmed reduction (TPR) was performed by a Micromeritic ChemiSorb 2750 automated system attached with ChemiSoft TPx software. Approximately 0.05 gram of the sample was put in a quartz tube, which was placed in a temperature-controlled furnace. Nitrogen gas was fed through sample at a flow rate of 25 mL/min. The sample was heated to 200 °C with a heating rate of 10 °C/min and the temperature was held for one hour to remove moisture. Then the sample was cooled down to 30 °C and 10 vol% H_2 in argon was fed through sample at a flow rate of 25 mL/min instead of nitrogen. The sample was heated from 30 °C to 800 °C with a heating rate of 10 °C/min. The hydrogen consumption was measured quantitatively by a thermal conductivity detector and the signal from this step was recorded every one second.

CHAPTER IV

RESULT AND DISCUSSION

This chapter presents the results and discussion on the effect of loading of silver, tungsten, copper, and molybdenum on properties of TiO_2 thin film.

4.1 Effect of silver loading to TiO_2 thin film

4.1.1 Phase structures of Ag-TiO_2

The bulk crystalline phase of Ag-TiO_2 samples were investigated using X-ray diffractometer (XRD). In Figure 4.1 presents XRD patterns of Ag-TiO_2 powder after calcined at 350 °C under stagnant air for 2 hours. The amounts of silver loading were 0.1, 0.5, 1.0, 3.0, and 5.0 mol% respectively. The major phase structure of TiO_2 was anatase, which were observed at 2θ of about 25.3° (101), 37.9° (004), 47.9° (200), 54.0° (105), 62.8 (204) and 69.2° (116) respectively. Small amount of rutile phase was observed at 2θ of about 27.3° (110) and 33.6° (101). The weak peak at 2θ of about 30° was assigned to brookite phase (121), which was a transitional phase from anatase to rutile in the healing processes (Shen et al., 2008). After silver loading, the main phase structure of TiO_2 still unchanged but the intensity of the diffraction patterns decreased remarkably, which correlated with crystallinity of TiO_2. This was indicated that the loading of silver suppressed the crystallization of TiO_2. Furthermore, no diffraction peak corresponding to silver oxide or metallic silver were detected in any samples, this may be due to low amount of silver species or uniformly dispersed on TiO_2 surface.
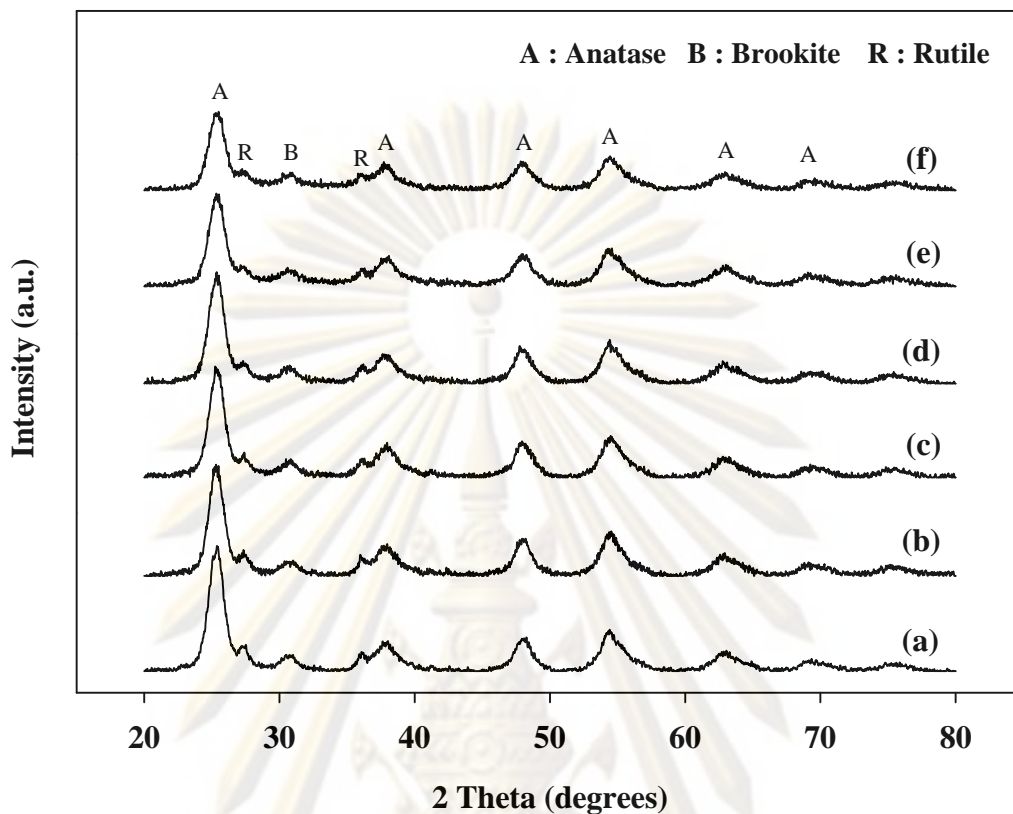
Figure 4.1 X-ray diffraction patterns of Ag-TiO$_2$ at various amount of silver loading when (a) 0.0 mol%, (b) 0.1 mol%, (c) 0.5 mol%, (d) 1.0 mol%, (e) 3.0 mol%, and (f) 5.0 mol% Ag.

Average cryatallite size of anatase was calculated from the strongest peak of XRD pattern at 2θ about 25.3° (101) using Scherrer's formula. The results were listed in Table 4.1. The crystallite size of TiO$_2$ slightly decreased with increasing of silver loading, which indicating that silver species affect on the grain growth of anatase TiO$_2$. This was described that, the radius of Ag$^+$ (126 pm) is much larger than that of Ti^{4+} (68 pm). So, silver ions unable enter into the lattice of TiO$_2$ to form a stable solid solution and dispersed on TiO$_2$ surface. In the other word TiO$_2$ particles will be separated by Ag$^+$ ions (He et al., 2002 and Zheng et al., 2007). During calcination process, the silver species became a barrier for rearrangement of Ti^{4+} and O^{2-} ions in anatase grain boundaries (Yu et al., 2005). Therefore, the anatase growth rate was suppressed and led to smaller crystallite size.

Table 4.1 Crystallite size of anatase in Ag-TiO$_2$ at various amount of silver loading.

Amount of silver loading (mol%)	Crystallite size (nm)
0.0	6.4
0.1	6.5
0.5	6.2
1.0	6.3
3.0	5.8
5.0	4.9

4.1.2 Oxidation state of silver species in Ag-TiO$_2$

Figure 4.2 shows Ag 3d XPS spectra of Ag-TiO$_2$ that contained 5.0 mol% Ag. It was observed that, the Ag 3d spectra consisted of two peaks spin-orbital splitting photoelectron, which corresponds to Ag 3d$_{3/2}$ and Ag 3d$_{5/2}$. As in previous studied, the binding energy of Ag 3d$_{5/2}$ for AgO, Ag$_2$O, and Ag are 367.0, 367.7, and 368.2 eV respectively (Xin et al., 2005). As seen in Figure 4.2, after the Ag 3d$_{5/2}$ peak was deconvoluted, two components of silver species were revealed at the binding energies of 367.6 eV and 368.1 eV. These were assigned to Ag$^+$ and Ag^0. Therefore, it was clearly indicated that, Ag$^+$ and Ag^0 were existence in form of Ag$_2$O and metallic silver.

4.1.3 Silver content in Ag-TiO$_2$

The amount of silver contents in Ag-TiO$_2$ samples were determined using inductively coupled plasma optical emission spectroscopy (ICP-OES) and the results were listed in Table 4.2. As seen in Table 4.2, the real mole percentages of silver were found in Ag-TiO$_2$ samples was lower than that the expected values.
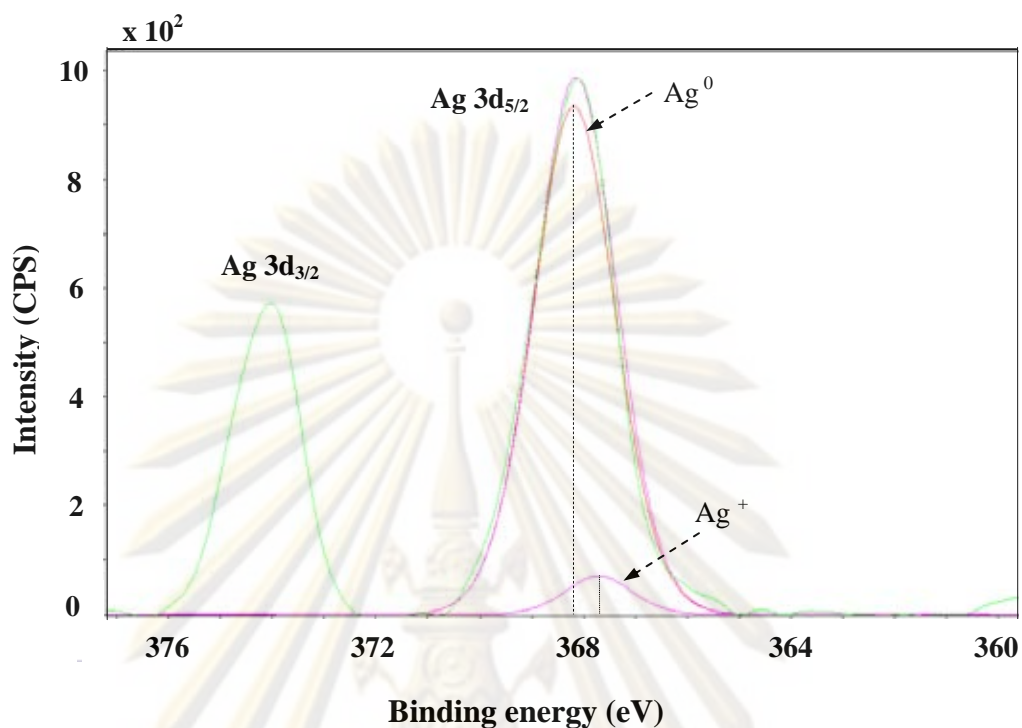
Figure 4.2 Ag 3d XPS spectra of Ag-TiO$_2$ that contained 5.0 mol% Ag.

Table 4.2 The amount of silver contents in Ag-TiO$_2$.

Amount of silver loading (mol%)	Amount of silver from ICP (mol%)
0.1	0.033
0.5	0.226
1.0	0.618
3.0	2.717
5.0	5.033

4.1.4 Specific surface area of Ag-TiO$_2$

The most common procedure for determining surface area of a solid is based on adsorption and condensation of nitrogen at liquid nitrogen temperature using static vacuum procedure. This method is also called BET (Brunauer Emmett Teller) method. Specific surface areas of Ag-TiO$_2$ at various amount of silver loading were listed in Table 4.3. Surface areas of Ag-TiO$_2$ were in the range of 98.6-109.0 m^2/g. The loading of silver did not have a significant effect on the specific surface area of Ag-TiO$_2$.

4.1.5 Surface morphology of Ag-TiO$_2$ thin films

AFM was used to characterize the morphology and uniformity of film surface. Figure 4.3 shows AFM images of Ag-TiO$_2$ film surface that contained various amount of silver. It was observed that, all films had a uniform surface. The loading of silver into TiO$_2$ did not have a significant effect on the grain size of TiO$_2$. Analysis of AFM images revealed that, the average roughness of the Ag-TiO$_2$ films surface appeared in the range of 2.303-2.807 nm (see Table 4.4).

Table 4.3 Specific surface area of Ag-TiO$_2$ at various amount of silver loading.

Amount of silver loading (mol%)	Specific surface area (m^2/g)
0.0	107.5
0.1	106.1
0.5	109.0
1.0	104.9
3.0	107.5
5.0	98.6
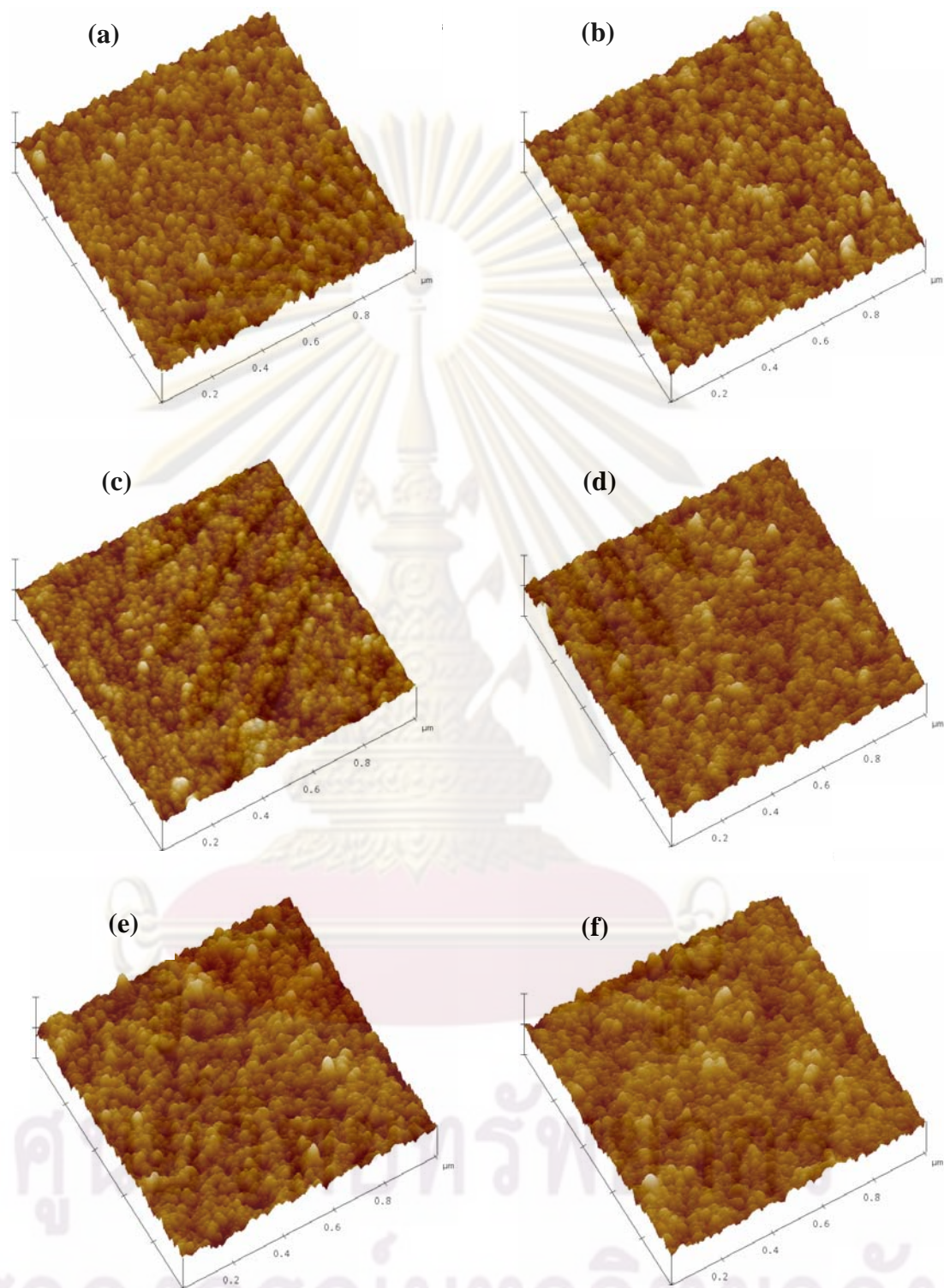
Figure 4.3 AFM images of Ag-TiO$_2$ film surface that contained (a) 0.0 mol%,
(b) 0.1 mol%, (c) 0.5 mol%, (d) 1.0 mol%, (e) 3.0 mol%, and
(f) 5.0 mol% Ag.

Table 4.4 Average roughness of Ag-TiO$_2$ films as determined from AFM images.

Amount of silver loading (mol%)	Average roughness (RMS) (nm)
0.0	2.429
0.1	2.373
0.5	2.443
1.0	2.303
3.0	2.618
5.0	2.807

4.1.6 Light absorption characteristic of Ag-TiO$_2$ thin films

Figure 4.4 shows UV-Vis absorption spectra of Ag-TiO$_2$ films deposited on glass surface in wavelength range of 300-700 nm. All films showed transmittance of light over 70 % entire visible region. The fast decreased in transmittance below 380 nm was due to absorption of light, which was caused by the excitation of electrons from the valance band to conduction of TiO$_2$ (Yu et al., 2002). When increased of silver loading, the transmittance of Ag-TiO$_2$ films decreased which was caused by the scatting of light from silver species. To calculate the band gap energy of Ag-TiO$_2$ film, the graph of $(-2.303h\upsilon \log T)^{1/2}$ versus $h\upsilon$ was plotted and extrapolated in a linear part leading to the band gap energy (see in APPENDIX D). It was found that the band gap energies of TiO$_2$ and TiO$_2$ films that contained silver of 0.1, 0.5, 1.0, 3.0, and 5.0 mol% were 3.24, 3.22, 3.20, 3.22, 3.44, and 3.42 respectively.
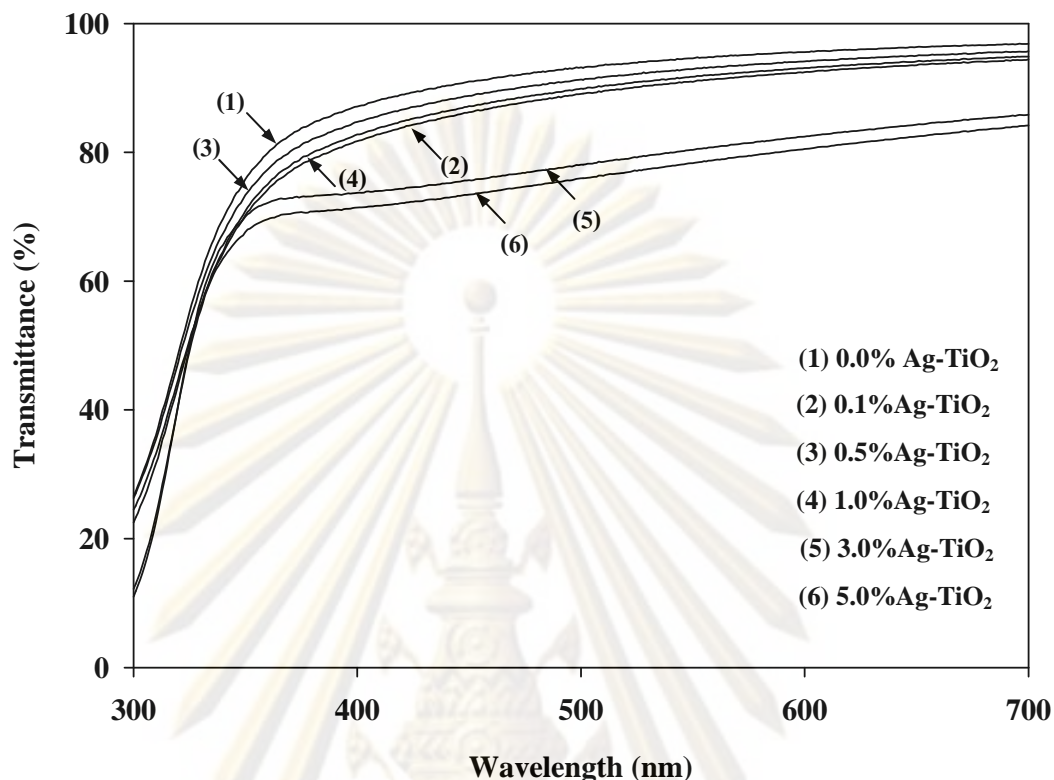
Figure 4.4 UV-Vis spectra of Ag-TiO$_2$ thin films deposited on glass surface.

4.1.7 Surface acidity of Ag-TiO$_2$

Temperature-programmed desorption (TPD) of probe molecules like ammonia and pyridine is a popular method for determining the acidity of solid catalysts as well as acid strength sites (Yang et al, 2005). In this investigation, the acidity measurement was carried out using NH$_3$-TPD. In Figure 4.5 presents NH$_3$-TPD profiles of Ag-TiO$_2$ at various amount of silver loading. There was only one asymmetric broad peak on the NH$_3$-TPD profiles of all the samples and the peak temperatures were ranged between 50 and 600 °C, indicating that the acid sites on surface were the weak and strong strength (Yang et al, 2005 and Yoon et al., 2007). Analysis the total acid sites of Ag-TiO$_2$ from NH$_3$-TPD profiles were listed in Table 4.5. The loading of silver reduced the total number of acid sites on Ag-TiO$_2$ surface.
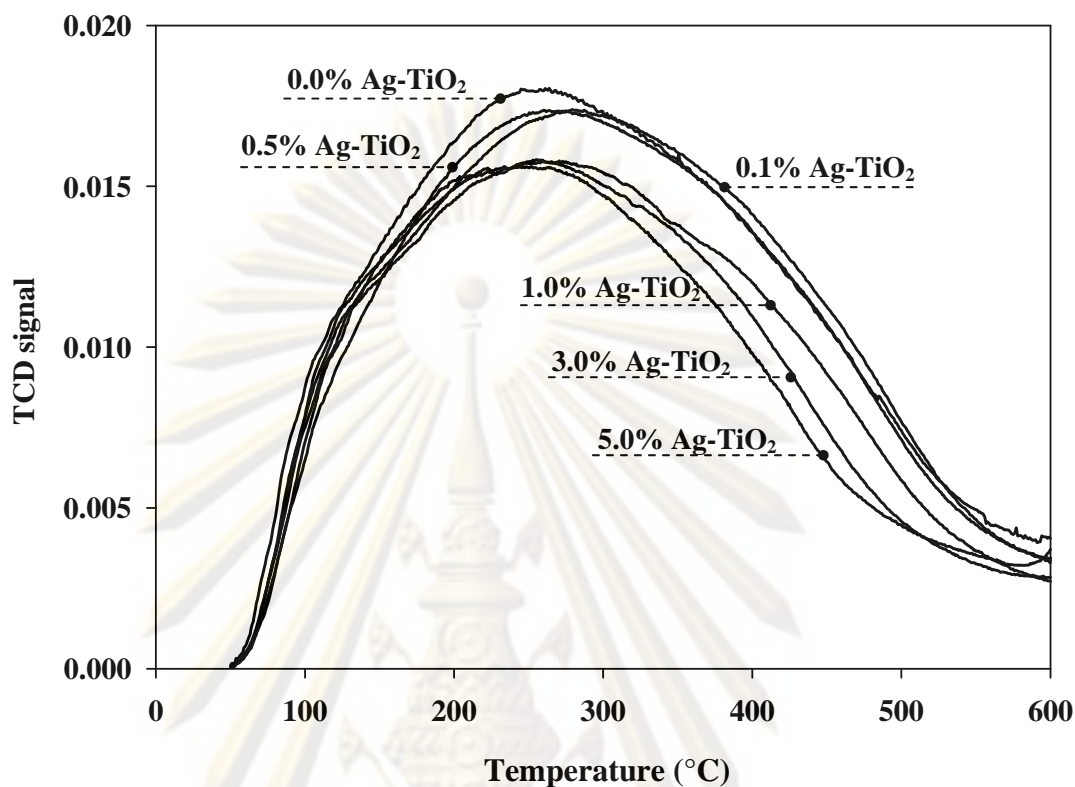
Figure 4.5 NH$_3$-TPD profiles of Ag-TiO$_2$ at various amount of silver loading.

Table 4.5 Surface acidity of Ag-TiO$_2$ as determined from NH$_3$-TPD profiles.

Amount of silver loading (mol%)	Total acid site (mmol NH$_3$/g)
0.0	23.79
0.1	23.48
0.5	23.88
1.0	22.21
3.0	21.04
5.0	19.45

4.1.8 Photoluminescence spectra of Ag-TiO$_2$

The photoluminescence (PL) emission spectra have been widely used to investigate the efficiency of charge carrier trapping, immigration and transfer, and to understand the fate of electron-hole pairs in semiconductor particles (Li et al., 2001). Since PL emission mainly results from the recombination of photo-generated electros and holes (Yu et al., 2003). The lower PL intensity indicated that the decreasing in the recombination rate. In Figure 4.6 shows PL spectra of Ag-TiO$_2$ at various amount of silver loading. It was observed that, PL spectra exhibited two emission peaks at the wavelength of about 420 and 485 nm. The former peak was due to free excitation emission of TiO$_2$ and the latter peak was due to the surface state such as Ti^{4+}-OH (Nagaveni et al., 2004). With increased silver loading, PL intensity significantly decreased. This was described on the basis of metal/semiconductor heterojunctions that, Schottky barriers are formed at contact region of two materials (see Figure 4.7) (Linsebigler et al., 1995). After Ag-TiO$_2$ being irradiated, Schottky barriers facilitate the electron transfer from TiO$_2$ (with high Fermi level) to Ag (with low Fermi level) (Hou et al., 2008 and Zheng et al., 2008). Therefore, the photo-generated electron-hole pairs were effectively separated rather than undergoing recombination. This reason was caused the decreasing in PL intensity after the loading of silver to TiO$_2$.
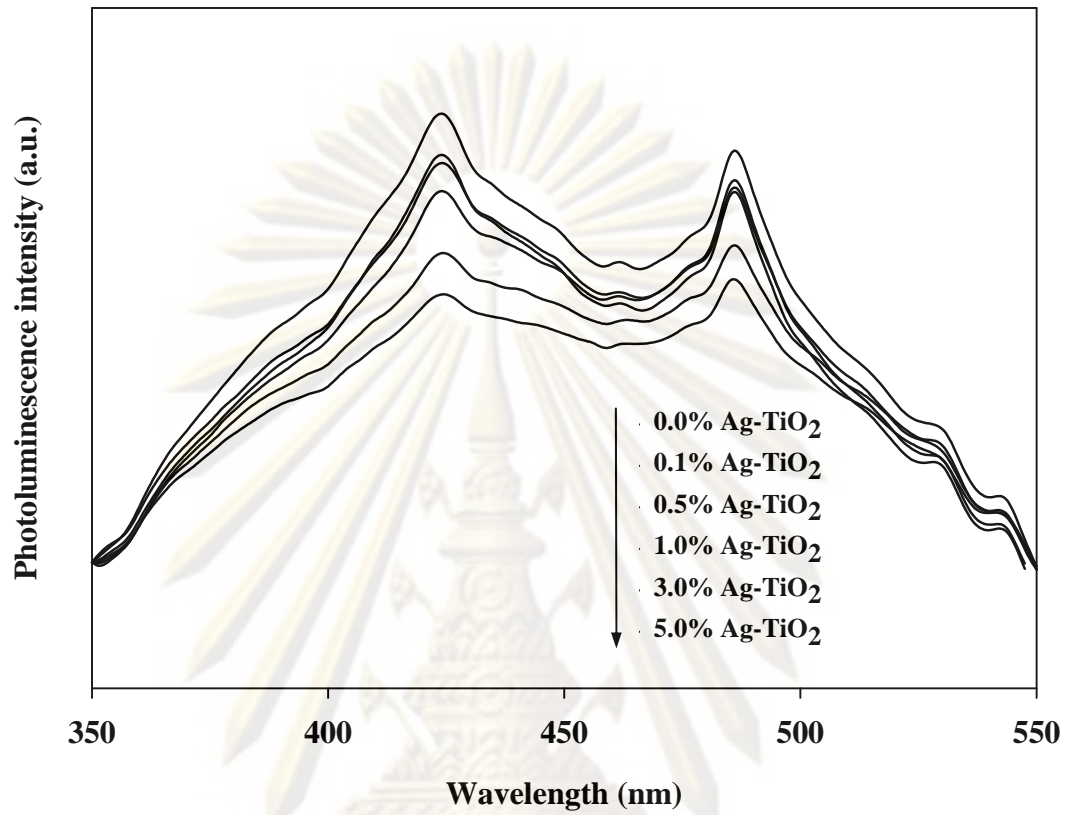
Figure 4.6 PL spectra of Ag-TiO$_2$ at various amount of silver loading.
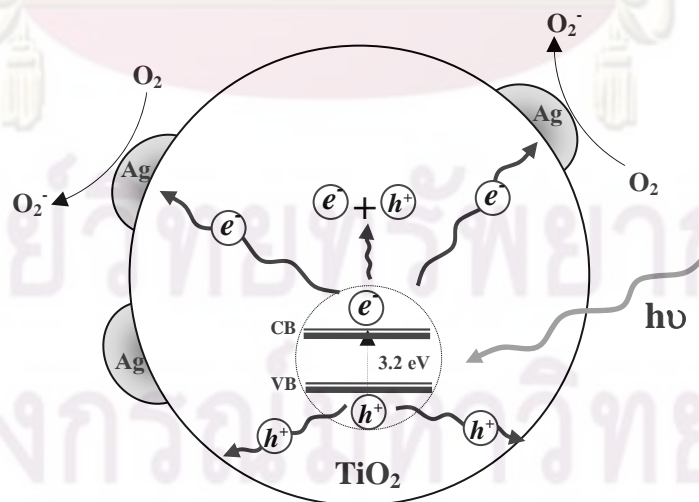
Figure 4.7 Charges separation at interfacial of Ag-TiO$_2$.

4.1.9 Photo-induced hydrophilicity of Ag-TiO$_2$ films

In Figure 4.8 shows the changes in water contact angle of Ag-TiO$_2$ films after UV irradiation for 3 hours. Before irradiation, all films had the initial contact angle about 17-21 degrees. In order to compare the effect of silver loading to the change of water contact angle, the initial contact angle of the films should be identical. Thus, the normalized contact angle, which is the angle of water droplet at any times to the initial contact angle of own films was used to consider. In Figure 4.9 shows the changes in normalized contact angle of Ag-TiO$_2$ films after UV irradiation for 3 hours. As seen in Figure 4.9, when increased silver loading, the decreasing of water contact angle of Ag-TiO$_2$ films faster than that TiO$_2$ film. Especially for 3.0-5.0% Ag-TiO$_2$ films showed the fastest time to decrease the water contact angle. Thus, TiO$_2$ films that contained 3.0-5.0 mol% silver possessed the best hydrophilic property.
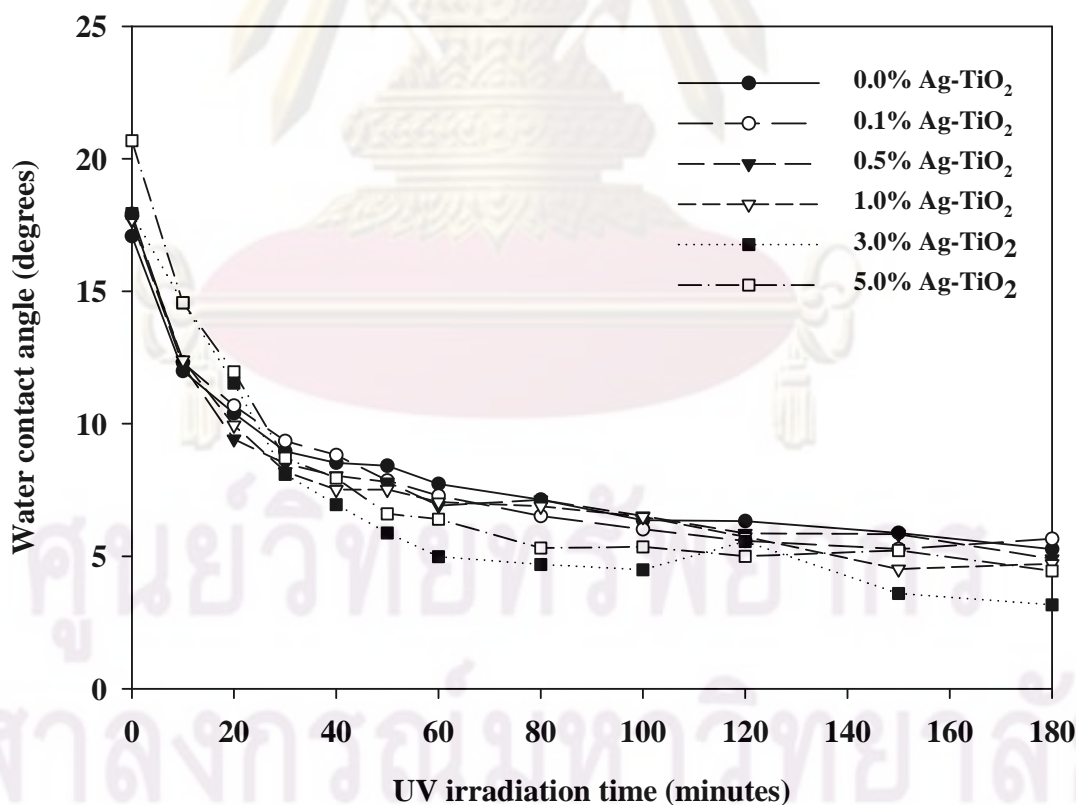
Figure 4.8   Change in contact angle of water droplet on the surface of various Ag-TiO$_2$ thin films.
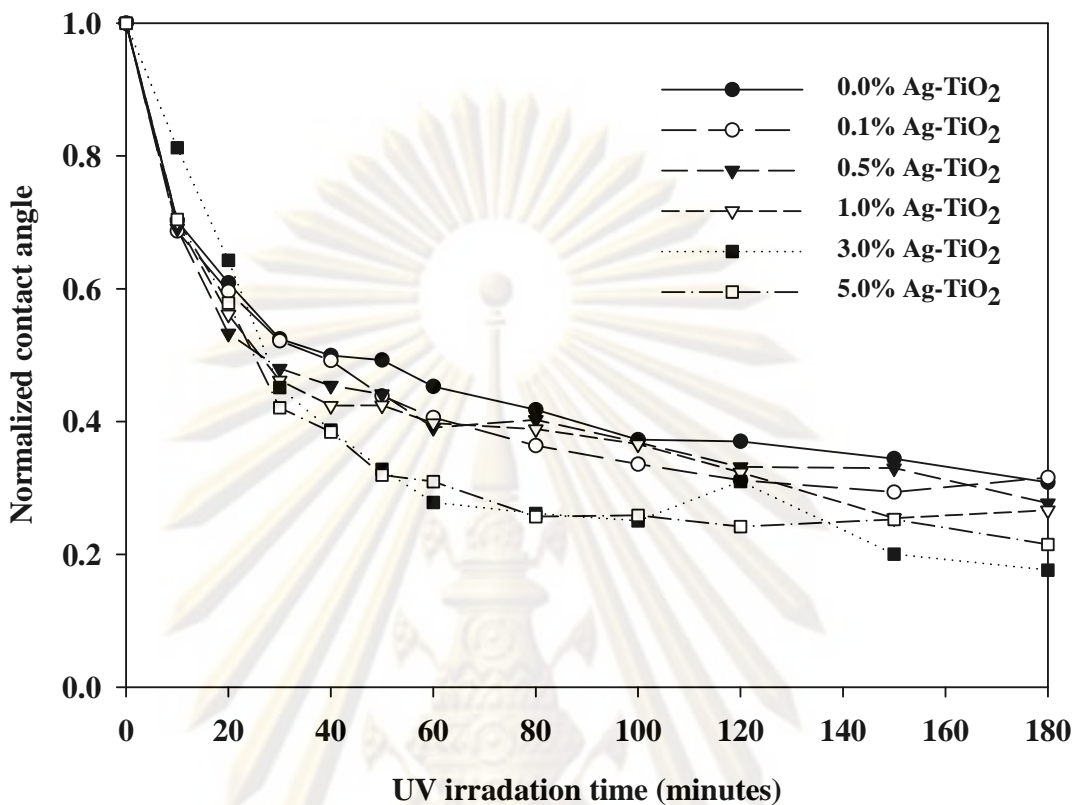
Figure 4.9 Change in normalized contact angle of water droplet on the surface of various Ag-TiO$_2$ thin films.

The role of silver species to the beneficial for hydrophilicity can be described as follow. After TiO$_2$ film was being irradiated, electrons and holes were generated as in Equation 2.4. The photo-generated electrons and holes will diffuse to the TiO$_2$ surface to created the surface oxygen vacancies (defective sites), according to mechanism of photo-induced hydrophilicity as seen in Equation 2.8 and 2.9 or undergo to recombine as in Equation 2.5. For Ag-TiO$_2$ films, photo-generated electrons were captured by Ag species and subsequently transferred to O$_2$ adsorbed on the surface to form O$_2^-$ (Sakthivel et al., 2004 and Yang et al., 2008) as seen in Equation 4.1 and 4.2. Thus, the recombination of photo-generated electrons and holes in Equation 2.5 were effectively inhibited. Therefore, the separation of photo-generated electron-hole pairs increases the ability of holes transferring to TiO$_2$ surface and created more surface oxygen vacancies, which brought about higher hydrophilic properties of Ag-TiO$_2$ films. This result agreed with the result from PL spectra.

$$TiO_2 \xrightarrow{\ h\upsilon\ } TiO_2(e^- + h^+) \tag{2.4}$$

$$Ti^{4+} + e^- \longrightarrow Ti^{3+} \tag{2.8}$$

$$2O^{2-} + 4h^+ \longrightarrow O_2 + \square \text{ (oxygen vacancy)} \tag{2.9}$$

$$TiO_2(e^- + h^+) \longrightarrow TiO_2 + heat \tag{2.5}$$

$$Ag + e^- \longrightarrow Ag^- \tag{4.1}$$

$$Ag^- + O_2 \longrightarrow O_2^- + Ag \tag{4.2}$$
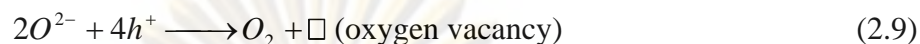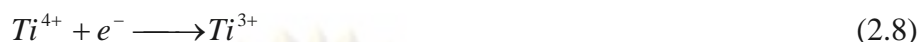
However, according to the results from PL spectra, the slowest recombination rate was found in TiO_2 films that contained 5.0 mol% silver (see Figure 4.6), but the changes in normalized contact angle of 5.0% Ag-TiO_2 film was almost identical to 3.0% Ag-TiO_2 film. This was attributed to, at 5.0 mol% of silver loading, the excessive amount of silver species on TiO_2 surface might be prevent the spreading of water droplets on film surface.

4.1.10 The sustainability of hydrophilicity of Ag-TiO_2 films after removal of UV irradiation

In order to assess the sustainability of hydrophilic property of Ag-TiO_2 film, the films were placed in a dark place with no exposure to light. As seen in Figure 4.10, the Ag-TiO_2 thin films that was able to retain the hydrophilic properties for the longest time was the films that contained 3.0-5.0 mol% silver. These observations suggested that the Ag-TiO_2 films that were able to retain the hydrophilicity for the longest time appeared to be the films that possessed the best hydrophilic property (i.e., 3-5 mol% Ag) to begin with.
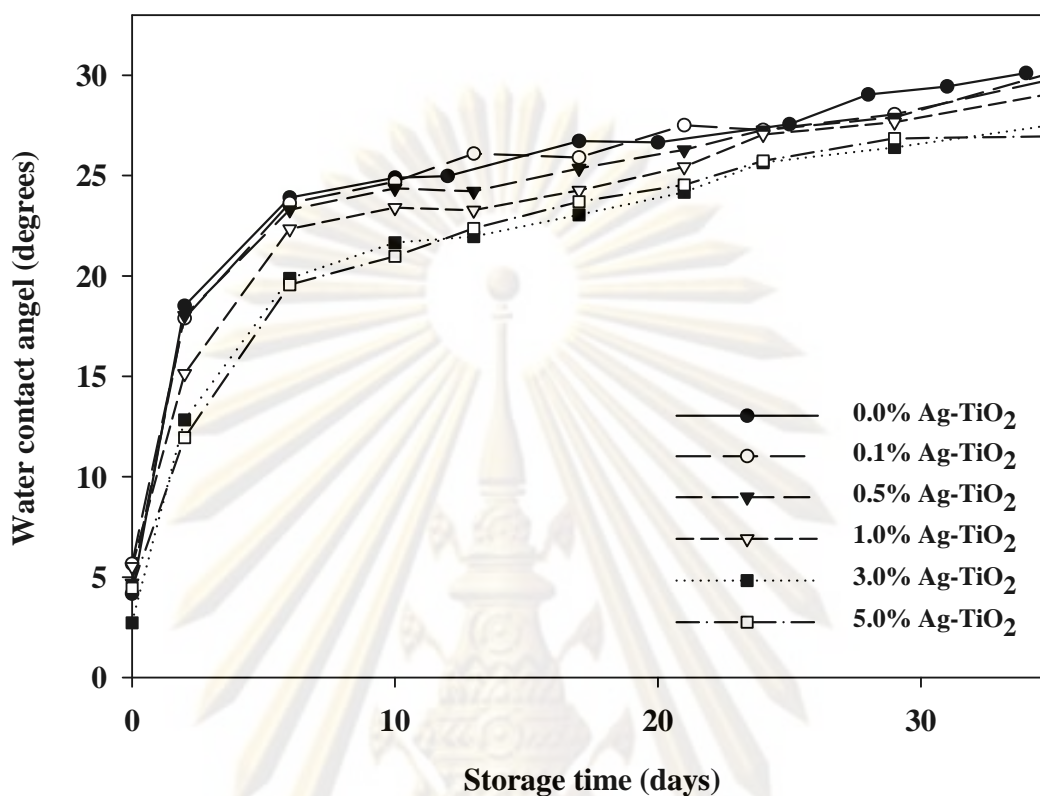
Figure 4.10 Change in contact angle of water droplet on the surface of various Ag-TiO$_2$ films in the absence of UV irradiation.

4.2 Effect of tungsten loading to TiO$_2$ thin films

4.2.1 Phase structures of W-TiO$_2$

The bulk crystalline phases of W-TiO$_2$ samples were investigated using X-ray diffractometer (XRD). In Figure 4.11 presents XRD patterns of W-TiO$_2$ powder after calcined at 350 °C under stagnant air for 2 hours. The amounts of tungsten loading were 0.1, 0.5, 1.0, and 1.5 mol% respectively. The major phase structure of TiO$_2$ was anatase, which were observed at 2θ of about 25.3° (101), 37.9° (004), 47.9° (200), 54.0° (105), 62.8 (204), and 69.2° (116). Small amount of rutile phase was observed at 2θ of about 27.3° (110) and 33.6° (101). The weak peak at 2θ of about 30° was assigned to brookite (121) phase which was a transitional phase from anatase to rutile in the healing processes (Shen et al., 2008). After tungsten

loading, the major phase structure of TiO_2 slightly changed. As seen at the diffraction peak of rutile phase at 2θ of $27.3°$ and $33.6°$, their gradually disappeared when increased tungsten loading. This indicates that, tungsten species hindered the phase transformation of anatase to rutile during calcination process. This result agrees with the reports of Li and coworkers (2001) and Song and coworkers (2006). Furthermore, no diffraction peak corresponding to tungsten oxide were detected in any samples, this may be due to low amount of tungsten species or uniformly dispersed on TiO_2 surface.

Average cryatallite size of anatase was calculated from the strongest peak of XRD patterns at 2θ about $25.3°$ (101) using Scherrer's formula. The results were listed in Table 4.6. The crystallite sizes of anatase TiO_2 decreased with increasing of tungsten loading, which corresponding with the broad of the diffraction peak. This indicated that tungsten species affect on the grain growth of anatase.

4.2.2 Oxidation state of tungsten in W-TiO$_2$

Figure 4.10 shows W 4f XPS spectra of W-TiO_2 that contained 1.5 mol% W. It was observed that, W 4f showed the broad peak, which was resulted by the overlap from two peaks spin-orbital splitting photoelectron of W $4f_{5/2}$ and W $4f_{7/2}$. As seen in Figure 4.12, after W 4f peak was deconvoluted, two components of tungsten species were revealed at binding energy of 35.2 eV and 36.8 eV respectively. These were assigned to W^{4+} and W_xO_y (mixed valance of W^{6+} and W^{5+}). Therefore, it was clearly indicated that, W^{4+}, W^{5+}, and W^{6+} were existence in form of WO_2, WO_3, and W_xO_y (Song et al. 2006).
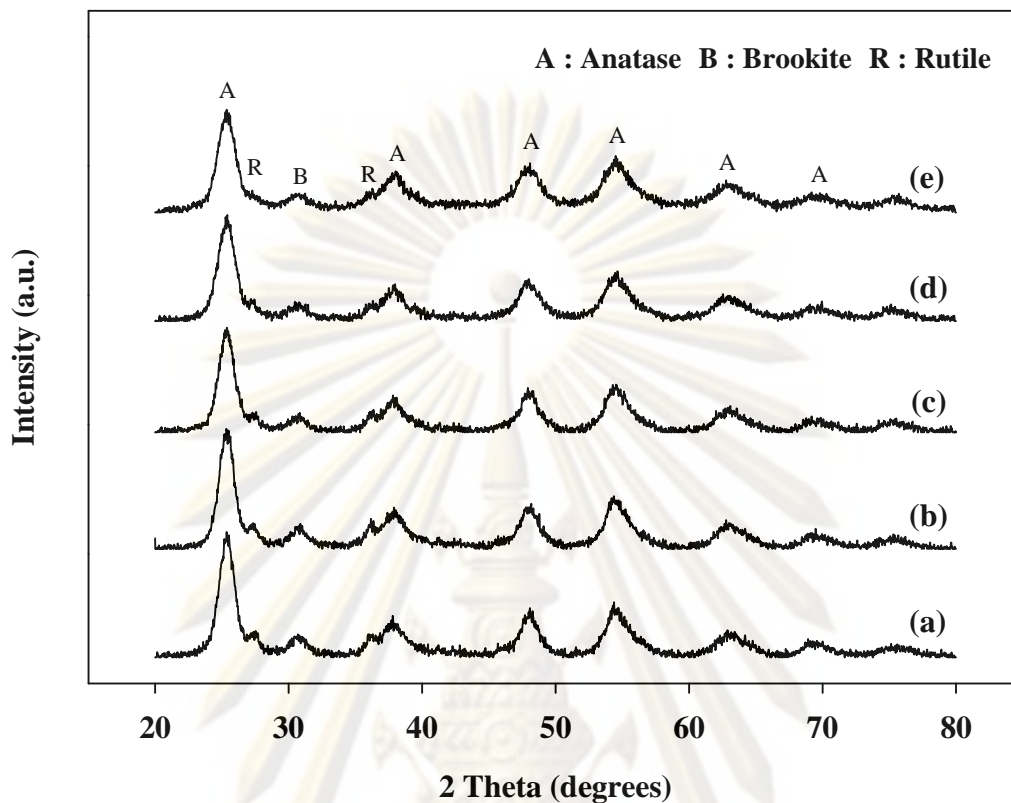
Figure 4.11 X-ray diffraction patterns of W-TiO$_2$ at various amount of tungsten loading when (a) 0.0 mol%, (b) 0.1 mol%, (c) 0.5 mol%, (d) 1.0 mol%, and (e) 1.5 mol% W.

Table 4.6 Crystallite size of anatase in W-TiO$_2$ at various amount of tungsten loading.

Amount of tungsten loading (mol%)	Crystallite size (nm)
0.0	6.2
0.1	6.2
0.5	6.3
1.0	5.5
1.5	5.4
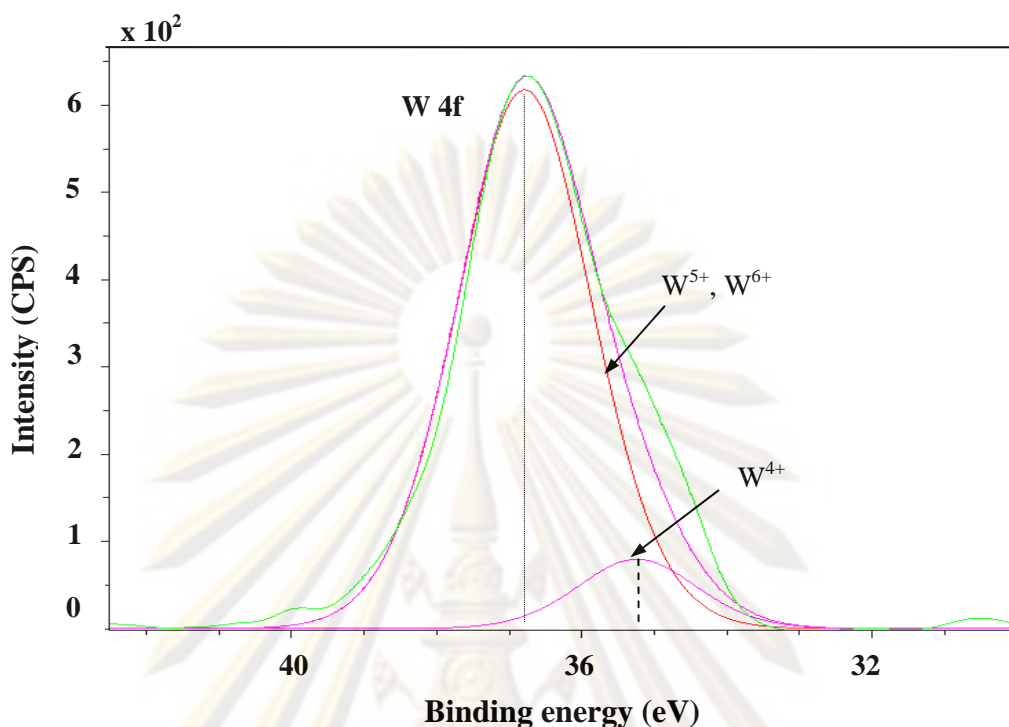
Figure 4.12 W 4f XPS spectra of W-TiO$_2$ that contained 1.5 mol% W.

4.2.3 Tungsten content in W-TiO$_2$

The amount of tungsten contents in W-TiO$_2$ sample was determined using inductively coupled-plasma optical emission spectroscopy (ICP-OES) and the results are shown in Table 4.7. As seen in Table 4.7, the real mole percentages of tungsten were found in W-TiO$_2$ was higher than that the expected values only slightly.

4.2.4 Specific surface area of W-TiO$_2$

The most common procedure for determining surface area of a solid is based on adsorption and condensation of nitrogen at liquid nitrogen temperature using static vacuum procedure. This method is also called BET (Brunauer Emmett Teller) method. Specific surface areas of W-TiO$_2$ with various amount of tungsten loading were listed in Table 4.8. The loading of tungsten have a significant effect on the specific surface area, which surface area increased with increasing the amount of tungsten loading, this was due to decreasing of crystallite size of TiO$_2$ (see Table 4.8).

Table 4.7 The amount of tungsten contents in W-TiO$_2$.

Amount of tungsten loading (mol%)	Amount of tungsten from ICP (mol%)
0.1	0.128
0.5	0.599
1.0	1.139
1.5	1.706

Table 4.8 Specific surface area of W-TiO$_2$ at various amount of tungsten loading.

Amount of tungsten loading (mol%)	Specific surface area (m^2/g)
0.0	92.5
0.1	91.2
0.5	94.8
1.0	100.0
1.5	108.5

4.2.5 Surface morphology of W-TiO$_2$ thin films

AFM was used to characterize the morphology and uniformity of surface. Figure 4.13 shows AFM images of W-TiO$_2$ thin film at various amount of tungsten loading. It was observed that, the surface topography of the films at various tungsten loading were obviously different. With increased tungsten loading, the smaller grain size was observed. This was suggested that, introducing of tungsten into TiO$_2$ suppressed the grain growth of TiO$_2$. Moreover, the average roughness of the W-TiO$_2$ film surface decreased with increasing the amount of tungsten loading from about 7.8 to 2.4 nm (see Table 4.9).
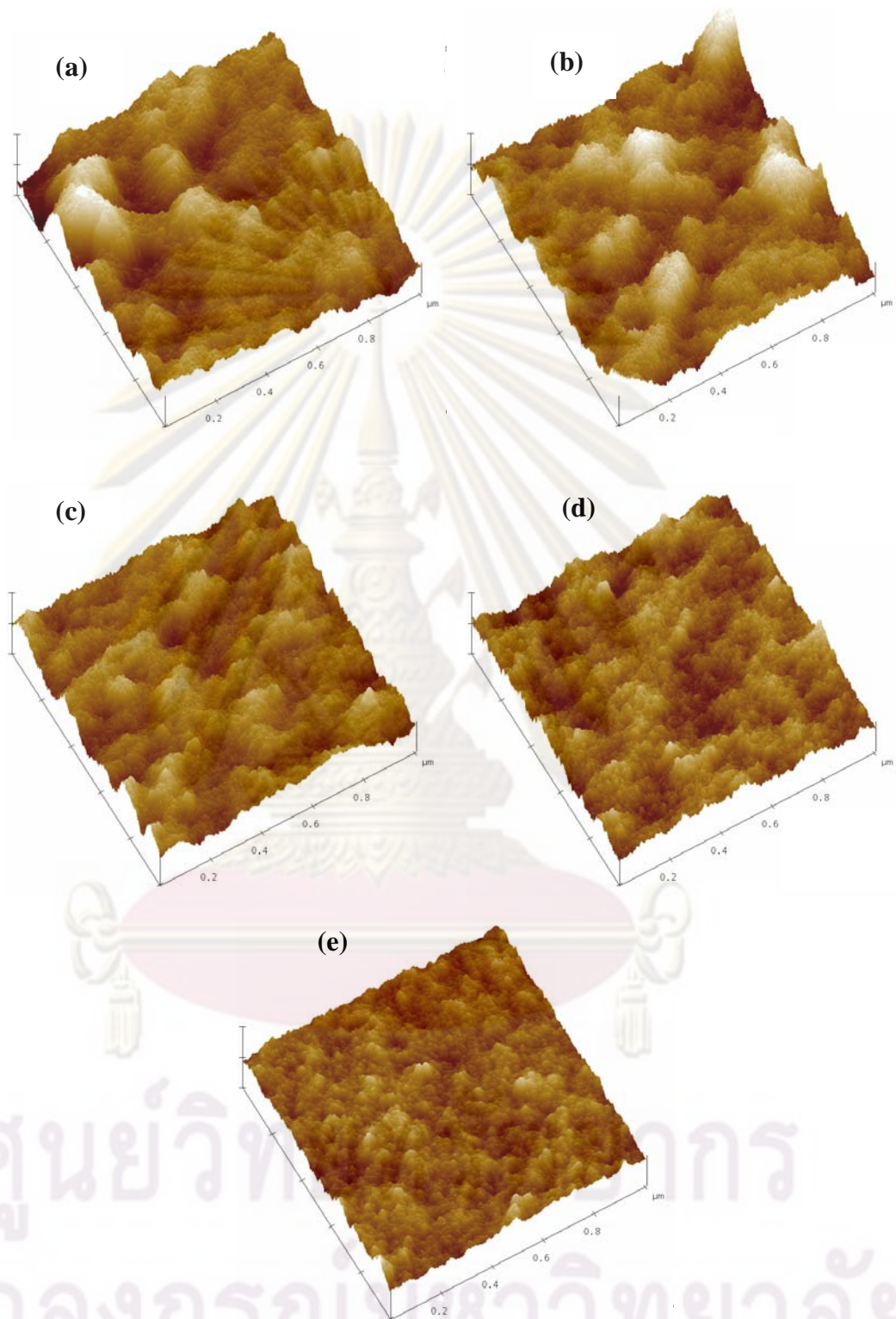
Figure 4.13 AFM images of W-TiO$_2$ film surface that contained (a) 0.0 mol%, (b) 0.1 mol%, (c) 0.5 mol%, (d) 1.0 mol%, and (f) 1.5 mol% W.

Table 4.9 Average roughness of W-TiO$_2$ films as determined from AFM images.

Amount of tungsten loading (mol%)	Average roughness (RMS) (nm)
0.0	7.796
0.1	7.801
0.5	4.987
1.0	4.121
1.5	2.419

4.2.6 Light absorption characteristic of W-TiO$_2$ thin films

Figure 4.14 show UV-Vis absorption spectra of W-TiO$_2$ films deposited on glass surface in wavelength range of 300-700 nm. All films showed transmittance of light over 80 % entire visible region. The fast decreased in transmittance below 380 nm is due to absorption of light, which was caused by the excitation of electrons from the valance band to conduction of TiO$_2$ (Yu et al., 2002). When increased tungsten loading, the absorption edge of W-TiO$_2$ films shifted toward longer wavelength (red-shifted), this indicated that decreasing in band gap energy. To calculate the band gap energy of W-TiO$_2$ film, the graph of $(-2.303h\upsilon \log T)^{1/2}$ versus $h\upsilon$ was plotted and extrapolated in a linear part leading to the band gap energy (see in APPENDIX D). It was found that the band gap energies of TiO$_2$ and TiO$_2$ that contained tungsten of 0.1, 0.5, 1.0, and 1.5 mol% were 3.24, 3.18, 3.17, 3.17, and 3.16 respectively.
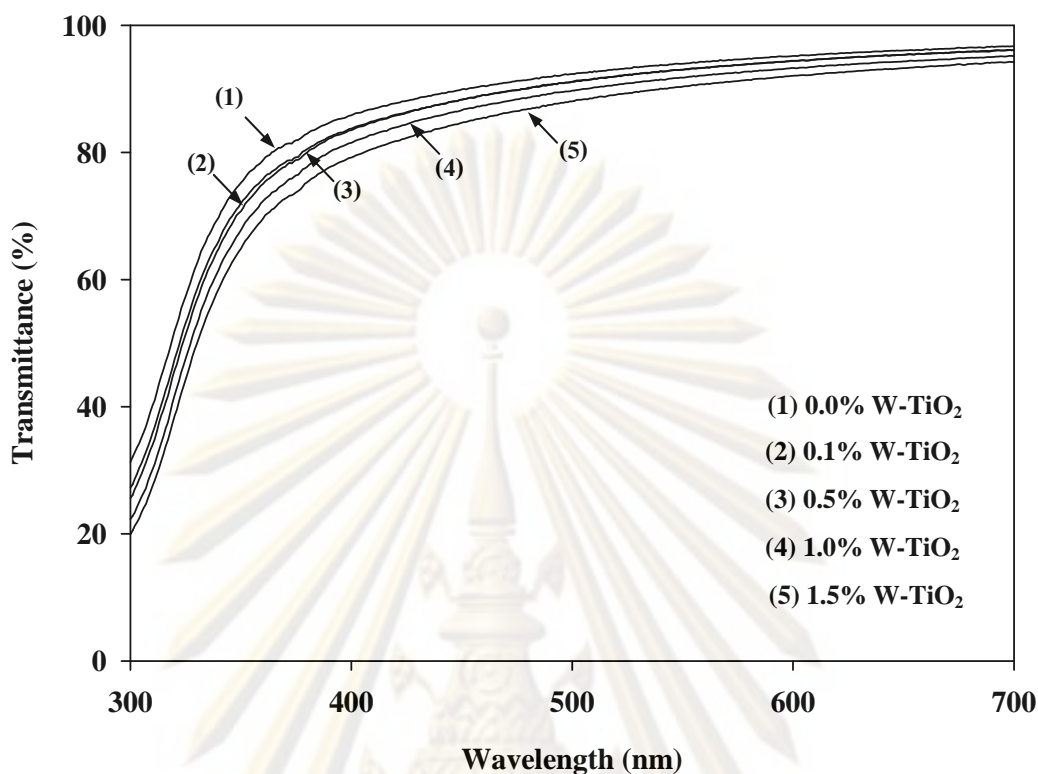
Figure 4.14 UV-Vis spectra of W-TiO$_2$ thin films deposited on glass surface.

4.2.7 Surface acidity of W-TiO$_2$

Temperature-programmed desorption (TPD) of probe molecules like ammonia and pyridine is a popular method for determining the acidity of solid catalysts as well as acid strength sites (Yang et al, 2005). In this investigation, the acidity measurement was carried out using NH$_3$-TPD. In Figure 4.15 presents NH$_3$-TPD profiles of W-TiO$_2$ at various amount of tungsten loading. There was only one asymmetric broad peak on the NH$_3$-TPD profiles of all the samples, and the peak temperatures are ranged between 50 and 600 °C, indicating that the acid sites on surface were the weak and strong strength (Yang et al, 2005 and Yoon et al., 2007). The overall surface acidity of W-TiO$_2$ increased as the amount of increased (see Table 4.10). It is well known that tungsten trioxide has Lewis acid sites (Yang et al, 2005). Furthermore, Tian and coworkers (2008) reported that WO$_3$/TiO$_2$ catalysts would exhibit surface acidity issued from the presence of Lewis and Bronsted acidic sites related to W^{6+} species.
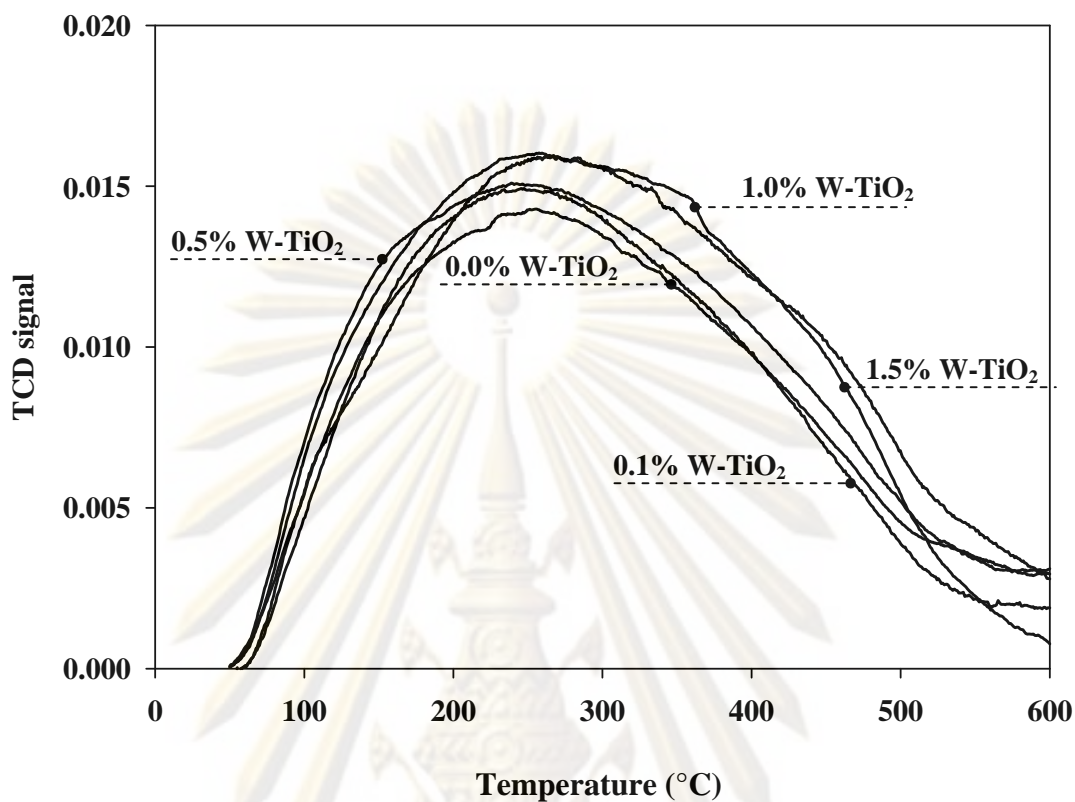
Figure 4.15 NH$_3$-TPD profiles of W-TiO$_2$ at various amount of tungsten loading.

Table 4.10 Surface acidity of W-TiO$_2$ samples as determined from NH$_3$-TPD profiles.

Amount of tungsten loading (mol%)	Total acid site (mmol NH$_3$/g)
0.0	17.83
0.1	19.15
0.5	20.44
1.0	21.46
1.5	25.32

4.2.8 Photoluminescence spectra of W-TiO$_2$

The photoluminescence (PL) emission spectra have been widely used to investigate the efficiency of charge carrier trapping, immigration and transfer, and to understand the fate of electron-hole pairs in semiconductor particles (Li et al., 2001). Since PL emission mainly results from the recombination of photo-induced electros and holes. The lower PL intensity indicates that the decreasing in recombination rate. In Figure 4.16 shows photoluminescence of W-TiO$_2$ at various amount of tungsten loading. It was observed that, PL spectra exhibited two emission peaks at the wavelength of about 420 and 485 nm. The former peak was due to free excitation emission of TiO$_2$ and the latter peak was due to the surface state such as Ti^{4+}-OH (Nagaveni et al., 2004). With increased silver loading, PL intensity significantly decreased. This was described on the coupling of two kind semiconductors that (see Figure 4.17), the Schottky barrier at between two semiconductors can be formed because of their different Fermi level and electronic band structure (Linsebigler et al., 1995 and Liqiang et al., 2006). On the basis of the relevant band position of WO$_3$ and TiO$_2$, both the conduction and valance band of WO$_3$ have larger positive potentials than that TiO$_2$. After W-TiO$_2$ being irradiated, photo-generated electrons are transferred to the lower conduction band of WO$_3$, while the holes will accumulate in the valance band of TiO$_2$ and further transferred to surface. Moreover, the photo-generated holes are transferred to valance band of WO$_3$ to valance of TiO$_2$ (Li et al., 2001 and Chai et al., 2006). Therefore, the photo-generated electron-hole pairs were effectively separated rather than undergoing recombination. This reason caused the decreasing in PL intensity after loading of tungsten to TiO$_2$.
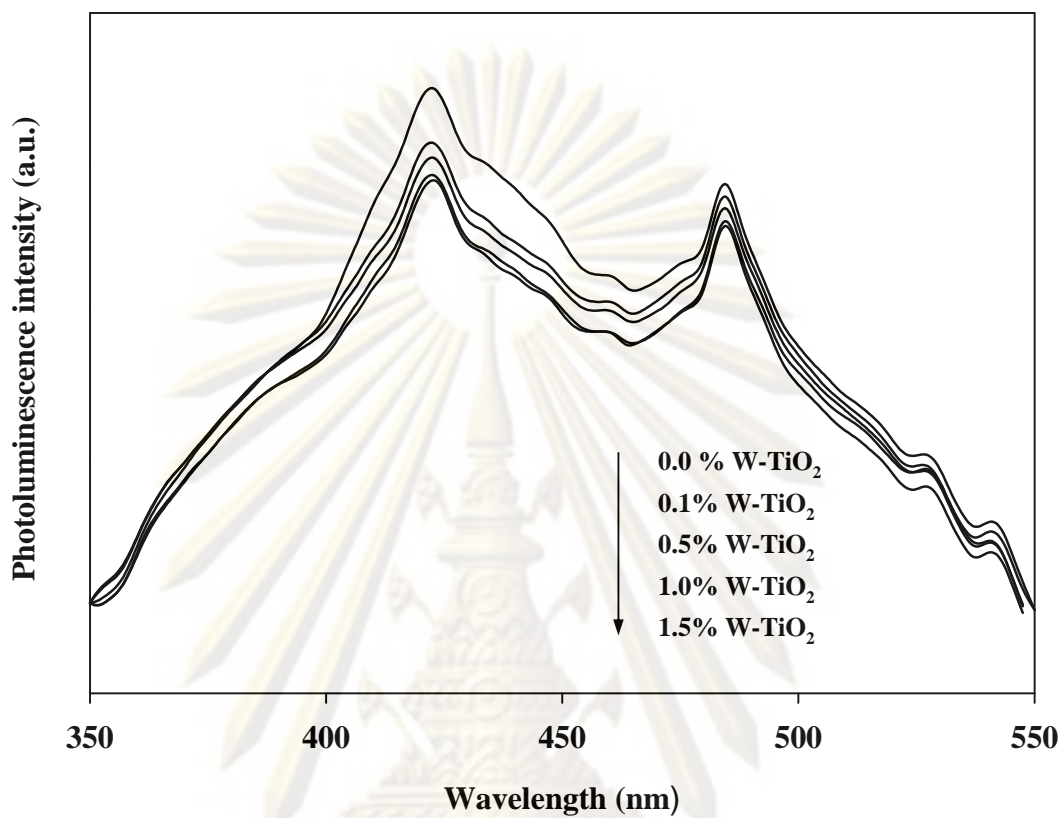
Figure 4.16 PL spectra of W-TiO$_2$ at various amount of tungsten loading.

Inside the figure (legend):

0.0 % W-TiO$_2$
0.1% W-TiO$_2$
0.5% W-TiO$_2$
1.0% W-TiO$_2$
1.5% W-TiO$_2$

Axis labels: Photoluminescence intensity (a.u.); Wavelength (nm)
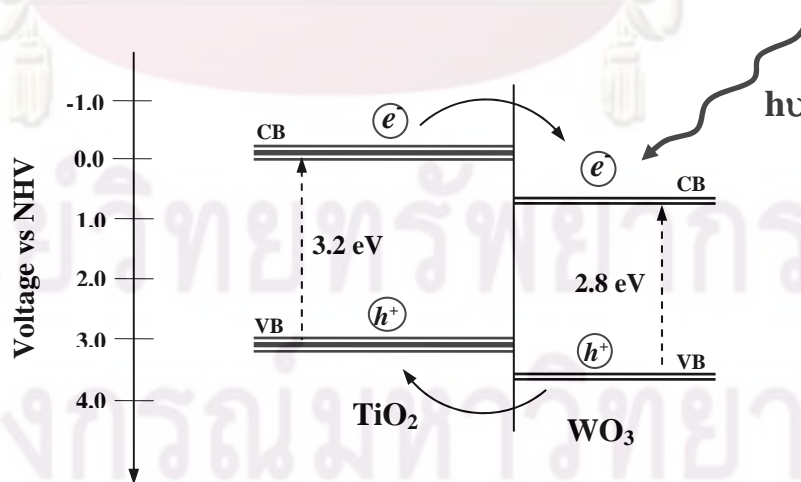
Figure 4.17 Energy diagram at interfacial for W-TiO$_2$.

Inside the figure: Voltage vs NHV; -1.0, 0.0, 1.0, 2.0, 3.0, 4.0; CB, VB; e, h^+; 3.2 eV; 2.8 eV; TiO$_2$; WO$_3$; hυ

4.2.9 Photo-induced hydrophilicity of W-TiO$_2$ films

In figure 4.18 shows the change in water contact angle of W-TiO$_2$ films after UV irradiation for 3 hours. Before irradiation, all films had the initial contact angle about 18 degrees. When the films were being irradiated, the contact angle gradually decreased until the angle reached to a steady state value, called saturated contact angle about 5 degrees. For TiO$_2$ film, the time needed to reach a saturated contact angle approximately 120 minutes. When increased tungsten loading, the time needed to reach a saturated contact angle were shorter than that TiO$_2$. Especially for 1.0 and 1.5% W-TiO$_2$ films showed the shortest time to reach a saturated contact angle approximately 50 minutes. Therefore, TiO$_2$ films that contained 1.0-1.5 mol% W possessed the best hydrophilic properties (or the shortest time to reach a saturated contact angle).

According to the results from PL spectra, the slowest recombination rates were also found in TiO$_2$ films that contained 1.0 and 1.5 mol% W too (see Figure 4.16). Therefore, the separation of photo-generated electron-hole pairs increases the ability of holes transferring to TiO$_2$ surface and created more surface oxygen vacancies (defective sites), which brought about higher hydrophilic properties of W-TiO$_2$ films. In addition, the adsorption sites for anions and cations are charged surface groups resulting from the protonation–deprotonation equilibria of the surface hydroxyl groups (Paola et al., 2004). The acidic surface has a higher affinity for species with unpaired electrons (Tian et al., 2008). According results from NH$_3$-TPD profile, the total acid sites increased after tungsten loading (see Table 4.10). Therefore, more acid sites on W-TiO$_2$ surface can adsorb a greater amount of hydroxyl groups or water molecule, which is led to increase the hydrophilic property of TiO$_2$ surface.
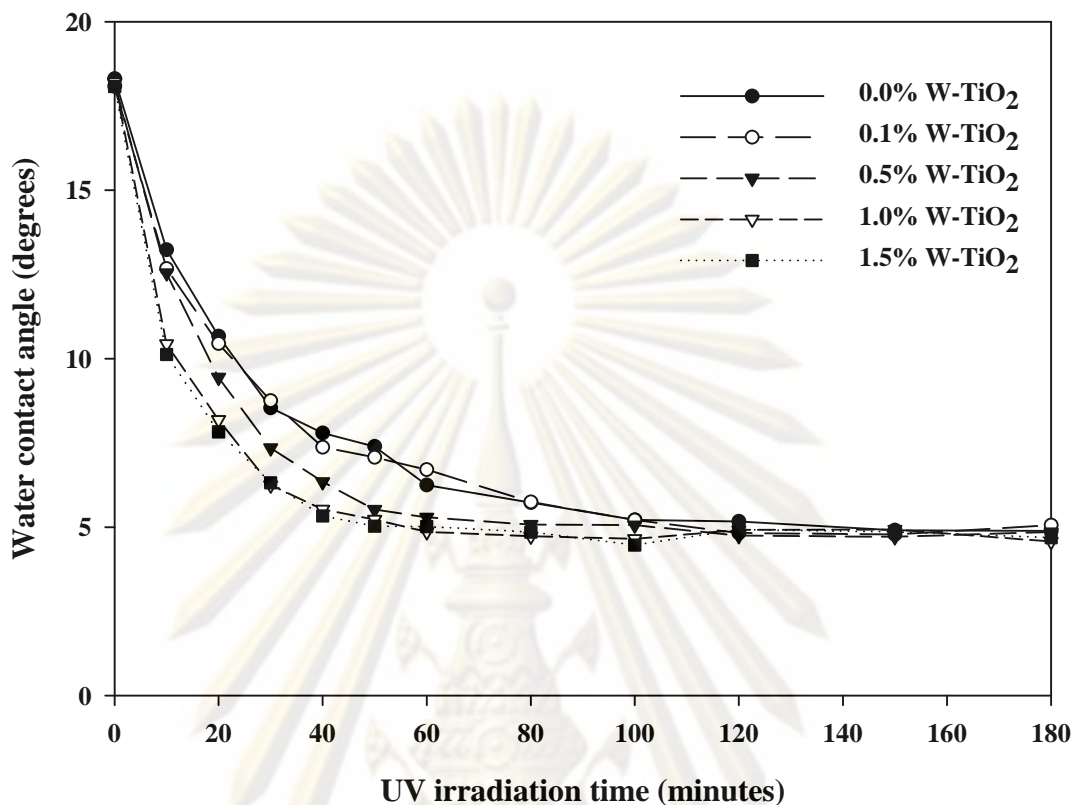
Figure 4.18 Change in contact angle of water droplet on the surface of various W-TiO$_2$ films.

4.2.10 The sustainability of hydrophilicity of W-TiO$_2$ films after removal of UV irradiation

In order to assess the sustainability of hydrophilic property of W-TiO$_2$ film, the films were placed in a dark place with no exposure to light as seen in Figure 4.19, the W-TiO$_2$ thin films that was able to retain the hydrophilic properties for the longest time was the films that contained 1.0-1.5 mol% W. These observations suggested that the W-TiO$_2$ films that were able to retain the hydrophilicity for the longest time appeared to be the films that possessed the highest hydrophilic properties (i.e., 1.0-1.5 mol% W) to begin with.
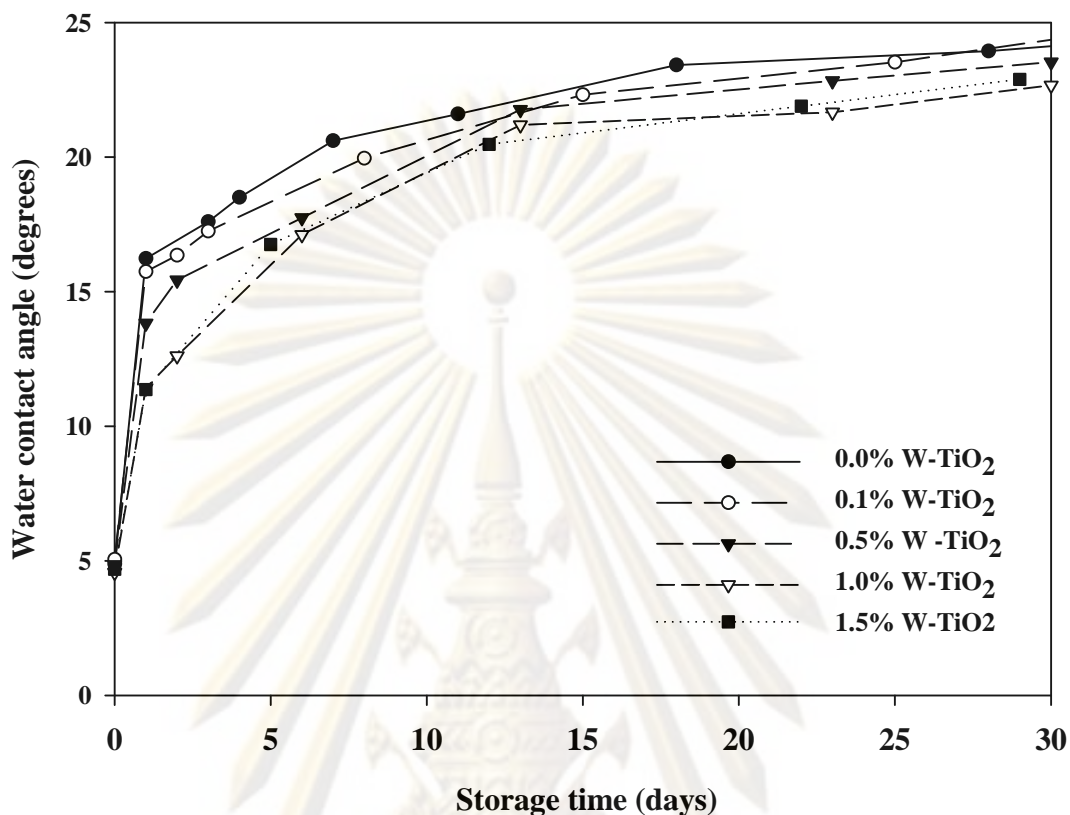
Figure 4.19 Change in contact angle of water droplet on the surface of various W-TiO$_2$ films in the absence of UV irradiation.

4.3 Effect of copper loading to TiO$_2$ thin film

4.3.1 Phase structures of Cu-TiO$_2$

The bulk crystalline phase of Cu-TiO$_2$ samples were investigated using X-ray diffractometer (XRD). In Figure 4.20 presents XRD patterns of Cu-TiO$_2$ powder after calcined at 350 °C under stagnant air for 2 hours. The amounts of copper loading were 0.1, 0.5, 1.0, and 5.0 mol% respectively. The major phase structure of TiO$_2$ was anatase, which were observed at 2θ of about 25.3° (101), 37.9° (004), 47.9° (200), 54.0° (105, 211), 62.8 (204) and 69.2° (116). Small amount of rutile phase was observed at 2θ of about 27.3° (110) and 33.6° (101). The weak peak at 2θ of about 30° was assigned to brookite (121) phase, which was a transitional phase from anatase to rutile in the healing processes (Shen et al., 2008). After copper loading, the major

phase structure and crystallinity of TiO_2 still unchanged, indicated that loading of copper did not affect to the crystallization of TiO_2. Furthermore, no diffraction peak corresponding to copper oxide were detected in any samples, this may be due to the amount of copper species very low or uniformly dispersed on TiO_2 surface.

Average cryatallite size of anatase was calculated from the strongest peak of XRD patterns at 2θ about $25.3°$ (101) using Scherrer's formula. The results were listed in Table 4.11. The loading of copper to TiO_2 did not have an effect on the average crystallite size of anatase.

4.3.2 Oxidation state of copper in Cu-TiO$_2$

Figure 4.21 shows XPS spectra of Cu 2p for Cu-TiO$_2$ that contained 15 mol% Cu. A major difference between Cu^+ and Cu^{2+} is the prominent satellite structure on the high biding energy side of the copper core line for Cu^{2+} species. These satellites have been attributed to shake-up transition by ligand-to-metal 3d charge transfer. This charge transfer cannot occur in Cu^+ (Colon et al., 2006). As seen in Figure 4.21, the Cu $2p_{3/2}$ and Cu $2p_{1/2}$ spin-orbital splitting photoelectron were located at binding energies of 933.6 eV and 953.3 eV and together with the characteristic shake-up feature at binding energy of 942.3 eV and 961.9 eV respectively. This was clearly indicated that, the existence of copper species were form in Cu^{2+} (CuO) (Colon et al., 2006 and Xu et al. 2008).
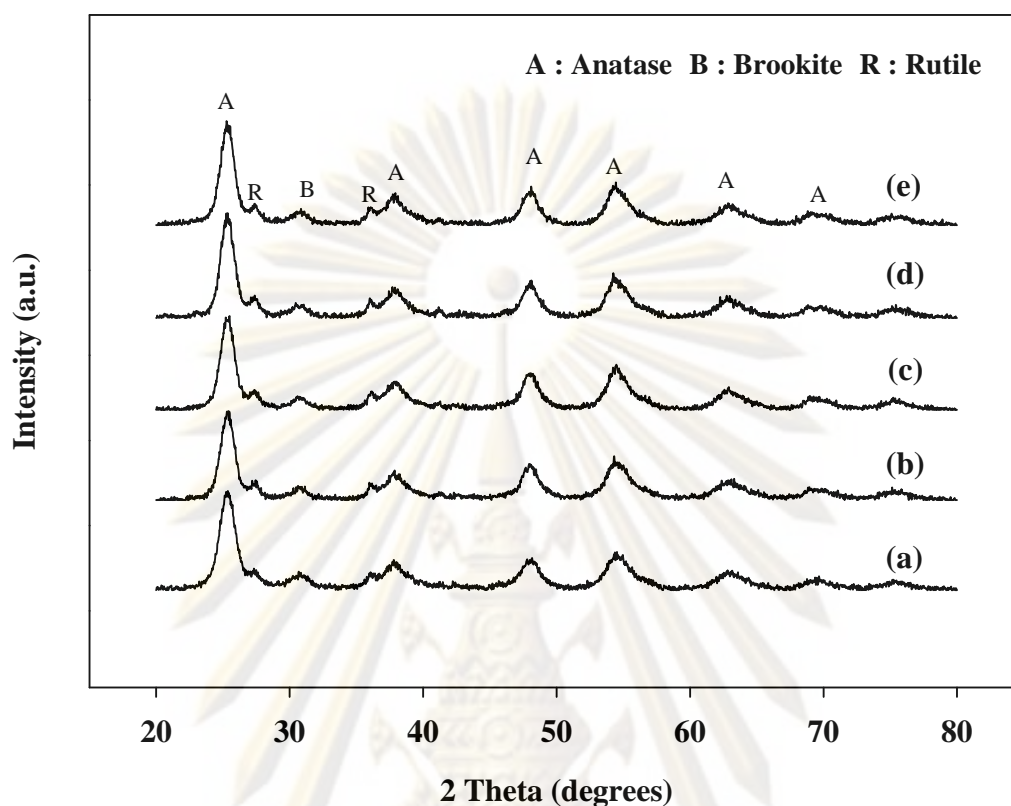
Figure 4.20 X-ray diffraction patterns of Cu-TiO$_2$ with various copper loading when (a) 0.0 mol%, (b) 0.1 mol%, (c) 0.5 mol%, (d) 1.0 mol%, and (e) 5.0 mol% Cu.

Table 4.11 Crystallite size of anatase in Cu-TiO$_2$ at various amount of copper loading.

Amount of copper loading (mol%)	Crystallite size (nm)
0.0	6.4
0.1	6.6
0.5	6.5
1.0	6.9
5.0	6.0
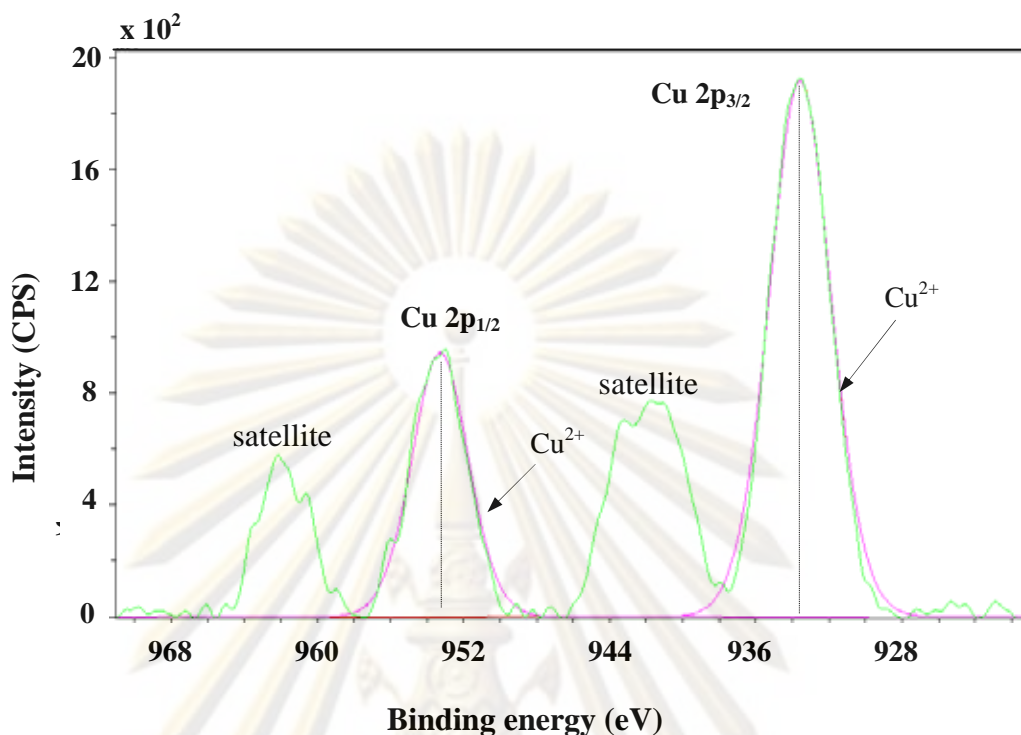
Figure 4.21 XPS spectra of Cu 2p for Cu-TiO$_2$ that contained 15 mol% Cu.

4.2.3 Copper content in Cu-TiO$_2$

The amount of tungsten contents in Cu-TiO$_2$ sample was determined using inductively coupled-plasma optical emission spectroscopy (ICP-OES) and the results are shown in Table 4.12. As seen in Table 4.12, the real mole percentages of copper were found in Cu-TiO$_2$ was higher than that the expected values only slightly.

Table 4.12 The amount of copper contents in Cu-TiO$_2$.

Amount of copper loading (mol%)	Amount of copper from ICP (mol%)
0.1	0.134
0.5	0.678
1.0	1.295
5.0	5.891

4.3.4 Specific surface area of Cu-TiO₂

The most common procedure for determining surface area of a solid is based on adsorption and condensation of nitrogen at liquid nitrogen temperature using static vacuum procedure. This method is also called BET (Brunauer Emmett Teller) method. Specific surface areas of Cu-TiO₂ at various amount of copper loading were listed in Table 4.13. Specific surface area of TiO₂ was 104.4 m²/g. After copper loading, surface areas were decreased. However, the amount of copper loading did not have a significant effect on the specific surface area, which was appeared in the range of 94.4-104.4 m²/g.

Table 4.13 Specific surface area of Cu-TiO₂ at various amount of copper loading.

Amount of copper loading (mol%)	Specific surface area (m²/g)
0.0	104.4
0.1	97.9.
0.5	95.9
1.0	94.4
5.0	96.9

4.3.5 Surface morphology of Cu-TiO₂ thin films

AFM was used to characterize the morphology and uniformity of surface. Figure 4.22 shows AFM images of Cu-TiO₂ film surface that contained various amount of copper. It was observed that, all films had a uniform surface. The loading of copper into TiO₂ did not have a significant effect on the grain size of TiO₂. Analysis of AFM images revealed that the average roughness of the Cu-TiO₂ films surface appeared in the range of 1.663-2.534 nm (see Table 4.14).
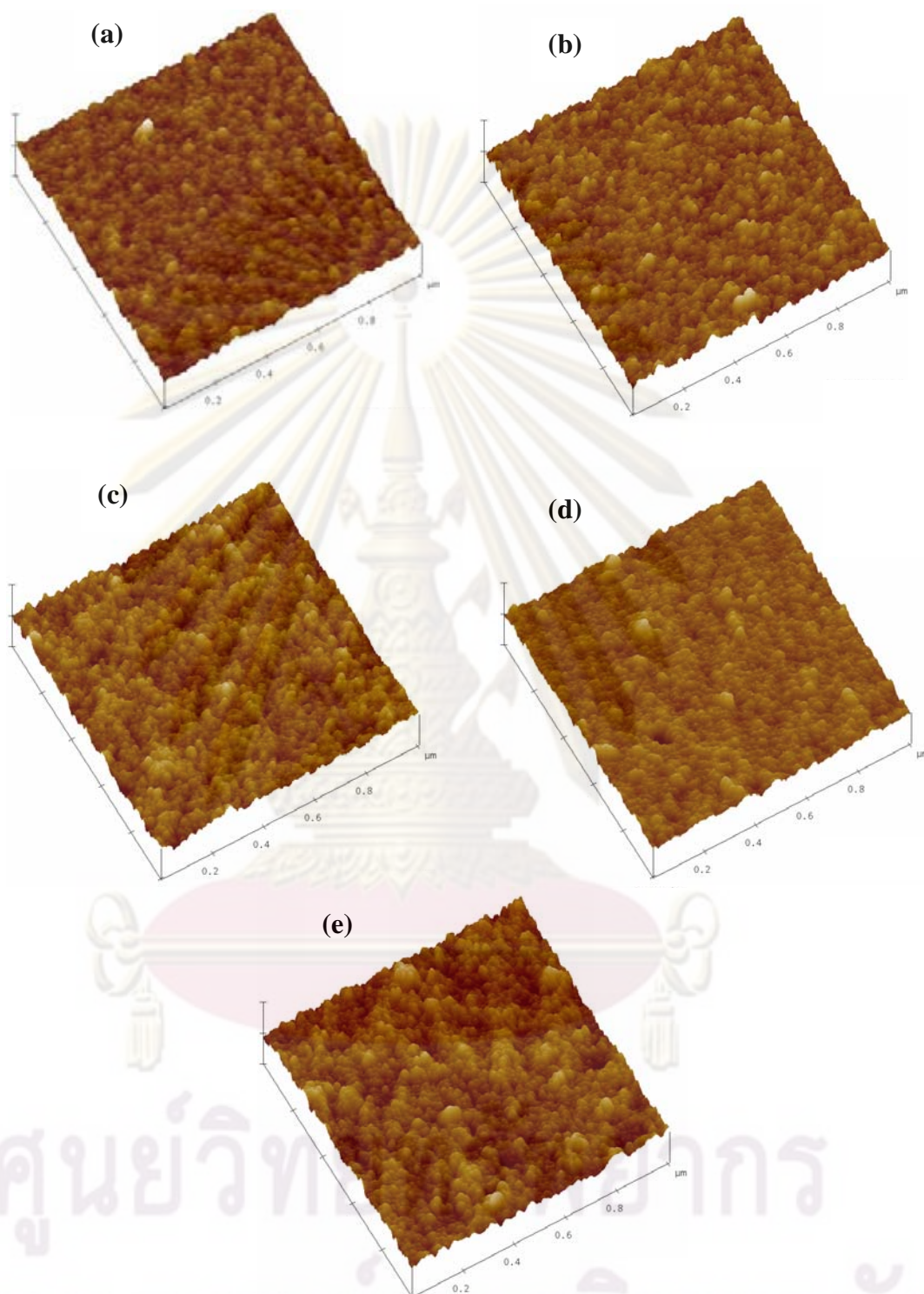
Figure 4.22 AFM images of Cu-TiO$_2$ film surface that contained (a) 0.0 mol% (b) 0.1 mol% (c) 0.5 mol% (d) 1.0 mol% and (f) 5.0 mol% Cu.

Table 4.14 Average roughness of Cu-TiO$_2$ films as determined from AFM images.

Amount of copper loading (mol%)	Average roughness (RMS) (nm)
0.0	1.663
0.1	2.199
0.5	2.126
1.0	2.061
5.0	2.534

4.3.6 Light absorption characteristic of Cu-TiO$_2$ thin films

Figure 4.23 shows UV-Vis absorption spectra of Cu-TiO$_2$ films deposited on glass surface in wavelength range of 300-700 nm. All films showed transmittance of light over 80 % in visible region. The fast decreased in transmittance below 380 nm was due to absorption of light, which was caused by the excitation of electrons from the valance band to conduction of TiO$_2$ (Yu et al., 2002). When increased copper loading, the absorption edge of Cu-TiO$_2$ films were shifted toward longer wavelength (red-shifted), this indicated that decreasing in band gap energy. To calculate the band gap energy of Cu-TiO$_2$ film, the graph of $(-2.303 h\upsilon \log T)^{1/2}$ versus $h\upsilon$ was plotted and extrapolated in a linear part leading to the band gap energy (see in APPENDIX D). It was found that the band gap energies of TiO$_2$ and TiO$_2$ that contained copper of 0.1, 0.5, 1.0, and 5.0 mol% were 3.24, 3.22, 3.24, 3.21, and 3.18 respectively.
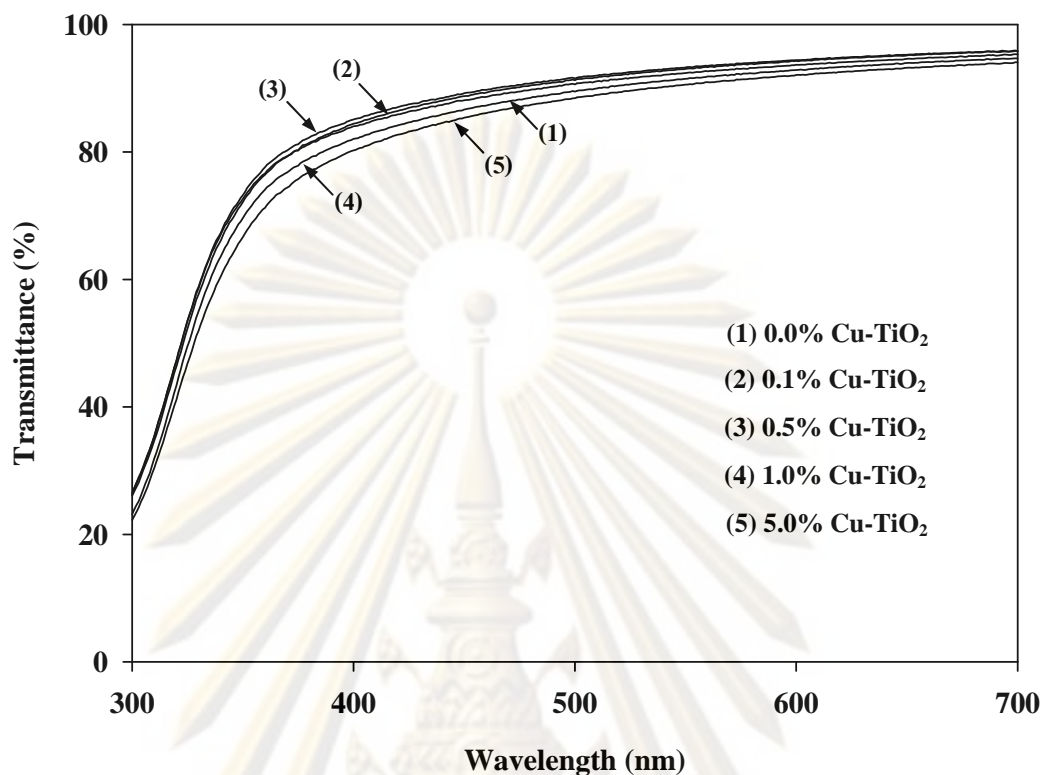
Figure 4.23 UV-Vis spectra of Cu-TiO$_2$ thin films deposited on glass surface.

4.3.7 Surface acidity of Cu-TiO$_2$

Temperature-programmed desorption (TPD) of probe molecules like ammonia and pyridine is a popular method for determining the acidity of solid catalysts as well as acid strength sites (Yang et al, 2005). In this investigation, the acidity measurement was carried out using NH$_3$-TPD. In Figure 4.24 presents NH$_3$-TPD profiles of Cu-TiO$_2$ with various amount of copper loading. There was only one asymmetric broad peak on the NH$_3$-TPD profiles of all the samples, and the peak temperatures are ranged between 50 and 600 °C, indicating that the acid sites on surface were the weak and strong strength (Yang et al, 2005 and Yoon et al., 2007). The total acid sites of Cu-TiO$_2$ were listed in Table 4.15, which loading of copper did not have a significant effect on the overall surface acidity of Cu-TiO$_2$.
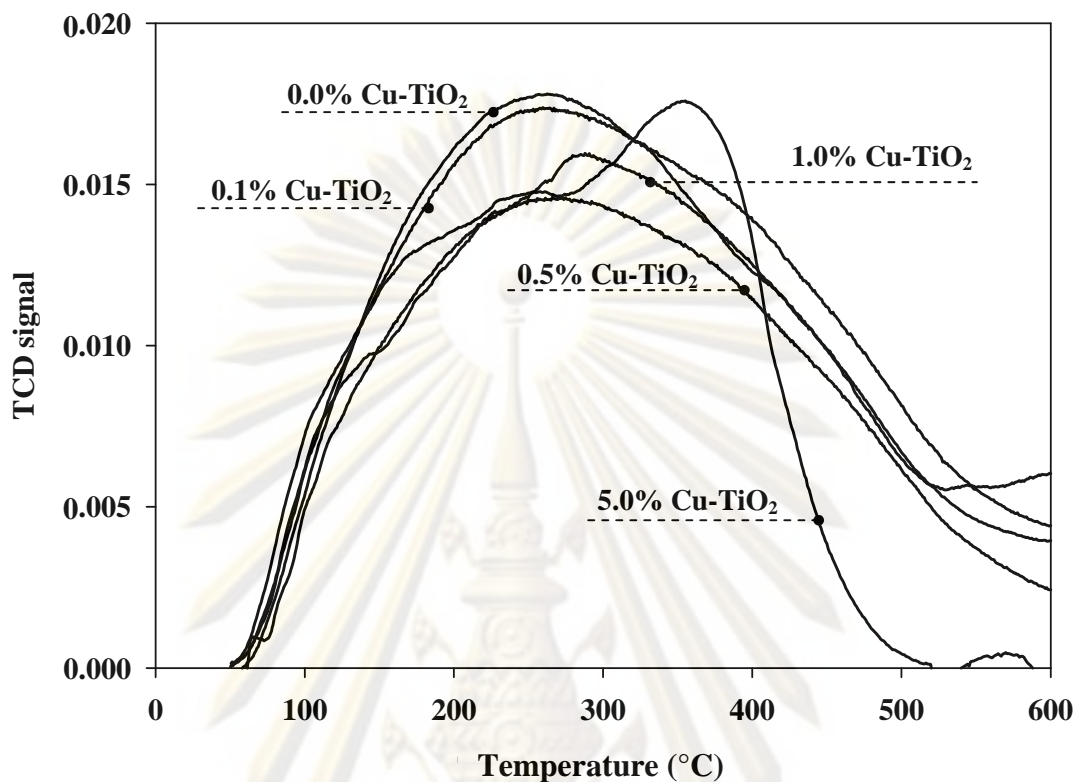
Figure 4.24 NH$_3$-TPD profiles of Cu-TiO$_2$ at various amount of copper loading.

Table 4.15 Surface acidity of Cu-TiO$_2$ samples as determined from NH$_3$-TPD profiles.

Amount of copper loading (mol%)	Total acid site (mmol NH$_3$/g)
0.0	19.87
0.1	22.57
0.5	20.63
1.0	20.38
1.5	24.35

4.3.8 Photoluminescence spectra of Cu-TiO$_2$

The photoluminescence (PL) emission spectra have been widely used to investigate the efficiency of charge carrier trapping, immigration and transfer, and to understand the fate of electron-hole pairs in semiconductor particles (Li et al., 2001). Since PL emission mainly results from the recombination of photo-induced electros and holes. The lower PL intensity indicates that the decreasing in recombination rate. In Figure 4.25 shows PL of Cu-TiO$_2$ at various amount of copper loading. It was observed that, PL spectra exhibit two emission peaks at the wavelength of about 420 and 485 nm. The former peak was due to free excitation emission of TiO$_2$ and the latter peak was due to the surface state such as Ti^{4+}-OH (Nagaveni et al., 2004). As seen Figure 4.25, the PL intensity decreased with increased the loading of copper. This is mainly due to electronic capture of Cu^{2+}. Cu^{2+} easily captures photo-induced electrons to become Cu^{+} which stable chemical state with a full-filed outer electronic ($1s^2\ 2s^2\ 2p^6\ 3s^2\ 3p^6\ 3d^{10}$) (liqiang et al., 2006 and Xu et al. 2008). This results also agree with the results of Choi et al., 2007, which reported that CuO in Cu/TiO$_2$ before the reaction was populated to be reduced during the methanol/water photodecomposition. Therefore, the photo-generated electron-hole pairs were effectively separated rather than undergoing recombination. This reason caused the decreasing in PL intensity after loading of copper to TiO$_2$.

4.3.9 Photo-induced hydrophilicity of Cu-TiO$_2$ films

In figure 4.27 shows the changes in water contact angle of Cu-TiO$_2$ film after UV irradiation for 3 hours. Before irradiation, the films had the initial contact angle about 23-25 degrees. When the films being were irradiated, the contact angle gradually decreased until the angle reached to a steady state value, called saturated contact angle. For TiO$_2$ film, the time needed to reach a saturated contact angle about 5 degrees approximately 120 minutes. When increased copper loading, the saturated contact angle of all Cu-TiO$_2$ films not reach to 5 degrees as to TiO$_2$ films within 180 minutes. So, Cu-TiO$_2$ films possessed worse hydrophilic properties than TiO$_2$ film did.

67
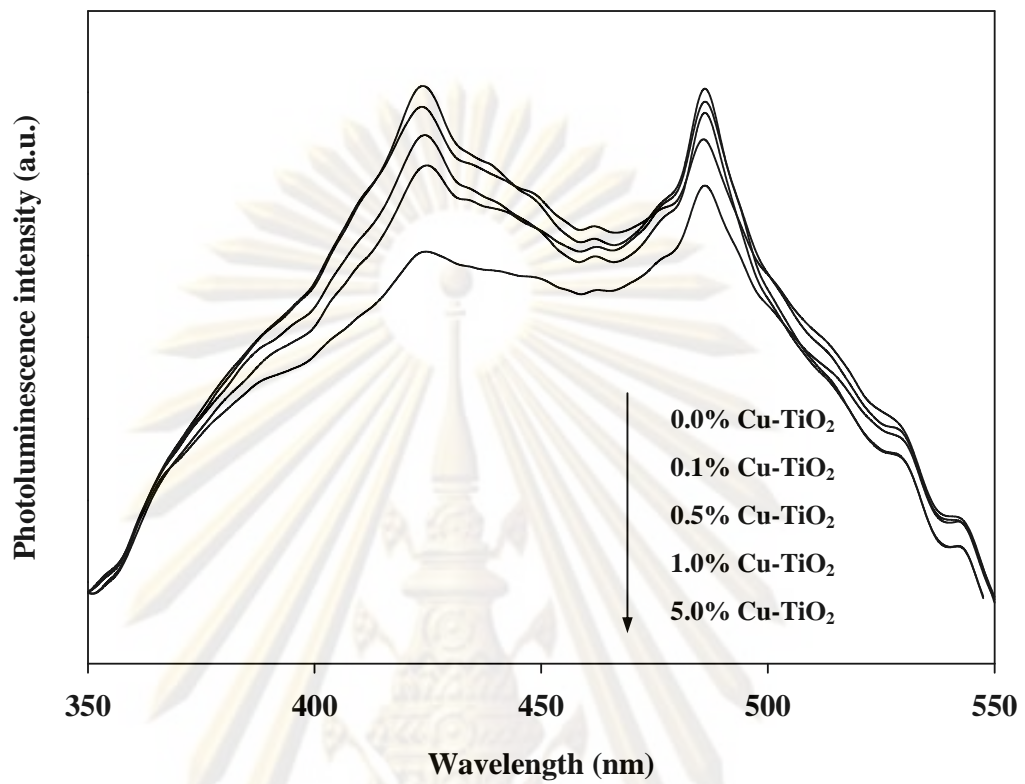
Figure 4.25 PL spectra of Cu-TiO₂ at various amount of copper loading.
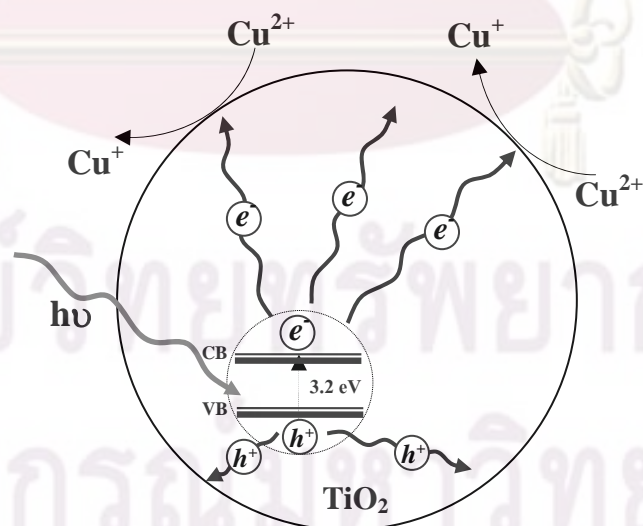
Figure 4.26 Photoreduction of Cu (II) at interfacial of Cu-TiO₂.
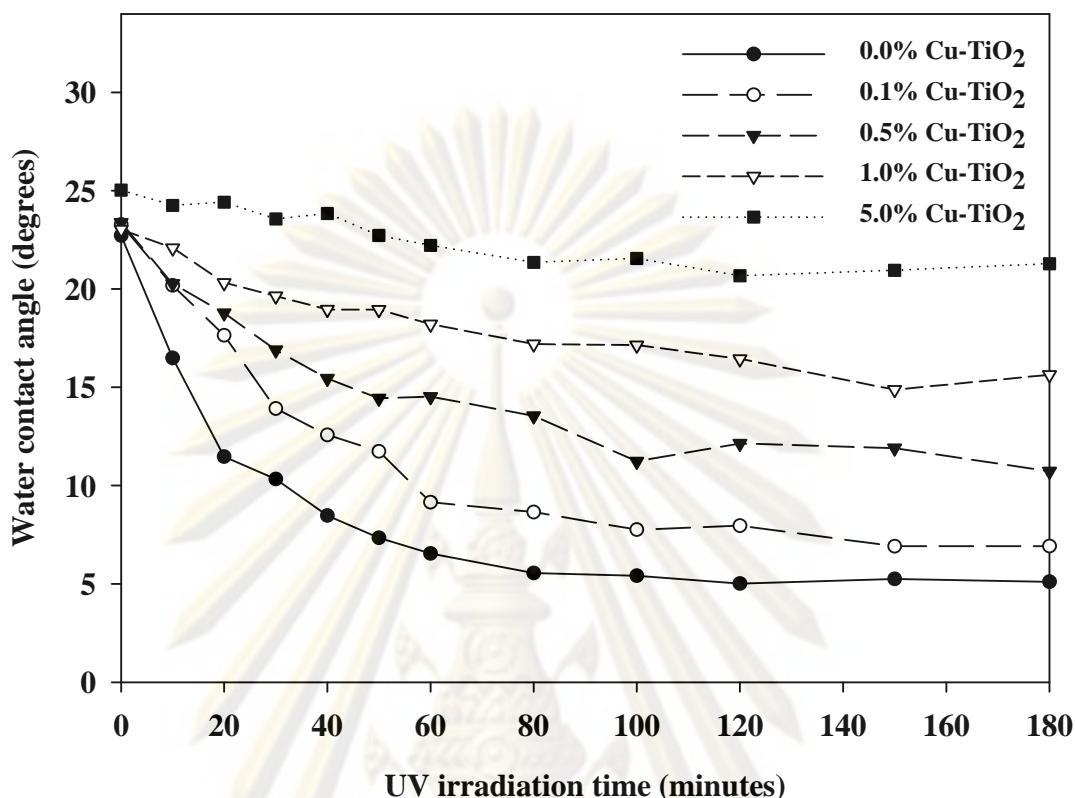
Figure 4.27 Change in contact angle of water droplet on the surface of various Cu-TiO$_2$ films.

According the above discussion in section 4.3.7, Cu^{2+} (CuO) in all Cu-TiO$_2$ films were photo-reduced by photo-induced electrons to higher stable form of Cu^{+} (Cu$_2$O). Thus, the ability of Cu^{2+} to captures photo-induced electrons is higher than that to produces surface oxygen vacancies on TiO$_2$ surface according to the mechanism of photo-induced hydrophilicity. Therefore, the lower surface oxygen vacancies were created, which brought about lower hydrophilic properties of Cu-TiO$_2$ films. Furthermore, CuO itself does not exhibit hydrophilicity (Miyayuchi, 2002). Thus, with increasing content of copper loading, the hydrophilicity of Cu-TiO$_2$ films decreased comparatively to TiO$_2$ film.

4.3.10 The sustainability of hydrophilicity of Cu-TiO$_2$ films after removal of UV irradiation

In order to assess the sustainability of hydrophilic property of Cu-TiO$_2$ film, the films were placed in a dark place with no exposure to light. As seen in Figure 4.28, the ability to retain the hydrophilic property of Cu-TiO$_2$ films after removal of UV irradiation was worse than that of TiO$_2$ film. These findings agreed with observation previously mentioned that the film with better hydrophilic property could retain the hydrophilic property longer.
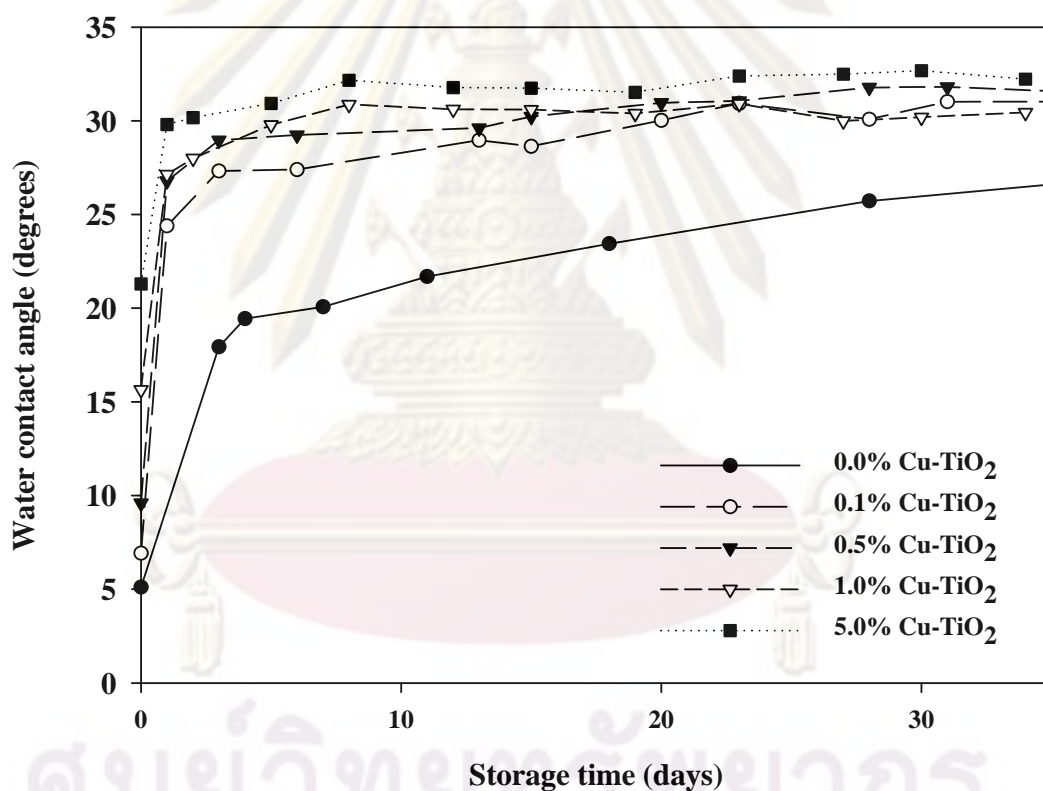
Figure 4.28 Change in contact angle of water droplet on the surface of various Cu-TiO$_2$ films in the absence of UV irradiation.

4.4 Effect of Molybdenum loading to TiO_2 thin films

4.4.1 Phase structures of Mo-TiO_2

The bulk crystalline phases of Mo-TiO_2 samples were investigated using X-ray diffractometer (XRD). In Figure 4.29 presents XRD patterns of Mo-TiO_2 powder after calcined at 350 °C under stagnant air for 2 hours. The amounts of molybdenum loading were 0.1, 0.3, 0.5, 0.7, and 1.0 mol% respectively. The major phase structure of TiO_2 was anatase, which were observed at 2θ of about 25.3° (101), 37.9° (004), 47.9° (200), 54.0° (105), 62.8° (204), and 69.2° (116). Small amount of rutile phase was observed at 2θ of about 27.3° (110) and 33.6° (101). The weak peak at 2θ of about 30° was assigned to brookite (121) phase which was a transitional phase from anatase to rutile in the healing processes (Shen et al., 2008). After molybdenum loading, the major phase structure and crystallinity of TiO_2 still unchanged, indicating that loading of molybdenum did not affect to the crystallization of TiO_2. Furthermore, no diffraction peak corresponding to molybdenum oxide was detected in any samples. This may be due to the amount of molybdenum species very low or uniformly dispersed on TiO_2 surface.

Average cryatallite size of anatase was calculated from the strongest peak of XRD patterns at 2θ about 25.3° (101) using Scherrer's formula. The results were listed in Table 4.16. Loading of molybdenm to TiO_2 did not have the effect on the average crystallite size of anatase.

4.4.2 Oxidation state of molybdenum in Mo-TiO_2

Figure 4.30 shows Mo 3p XPS spectra of Mo-TiO_2 that contained 10 mol% Mo. It was observed that, the Mo 3p spectra consisted of two peaks spin-orbital splitting photoelectron (Mo $3p_{3/2}$ and Mo $3p_{1/2}$), which located at the binding energies of 398.0 and 415.6 eV respectively. These were assigned to Mo^{6+} (Zhang et al., 2008). Therefore, it was clearly indicated that, Mo^{6+} was existence in form of MoO_3.
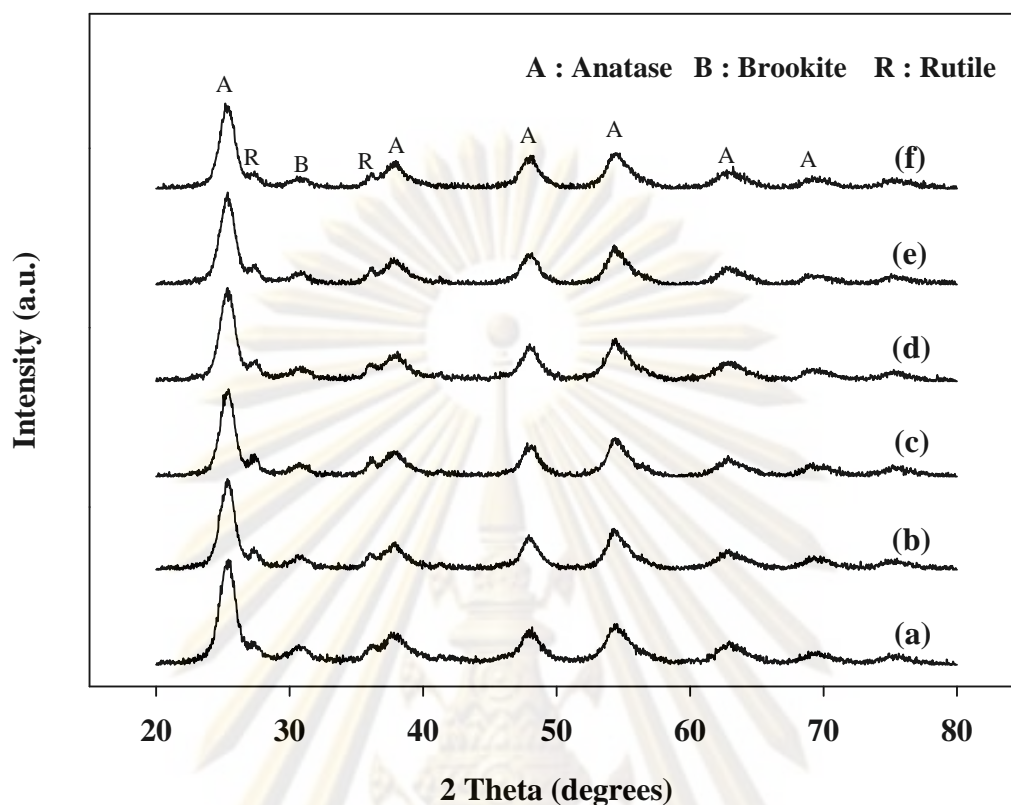
Figure 4.29   X-ray diffraction patterns of Mo-TiO$_2$ with various Mo loading when
(a) 0.0 mol%, (b) 0.1 mol%, (c) 0.3 mol%, (d) 0.5 mol%, (e) 0.7 mol%,
and (f) 1.0 mol% Mo.

Table 4.16 Crystallite size of anatase in Mo-TiO$_2$ at various amount of molybdenum
loading.

Amount of molybdenum loading (mol%)	Crystallite size (nm)
0.0	6.0
0.1	6.3
0.3	6.3
0.5	6.2
0.7	6.1
1.0	6.1
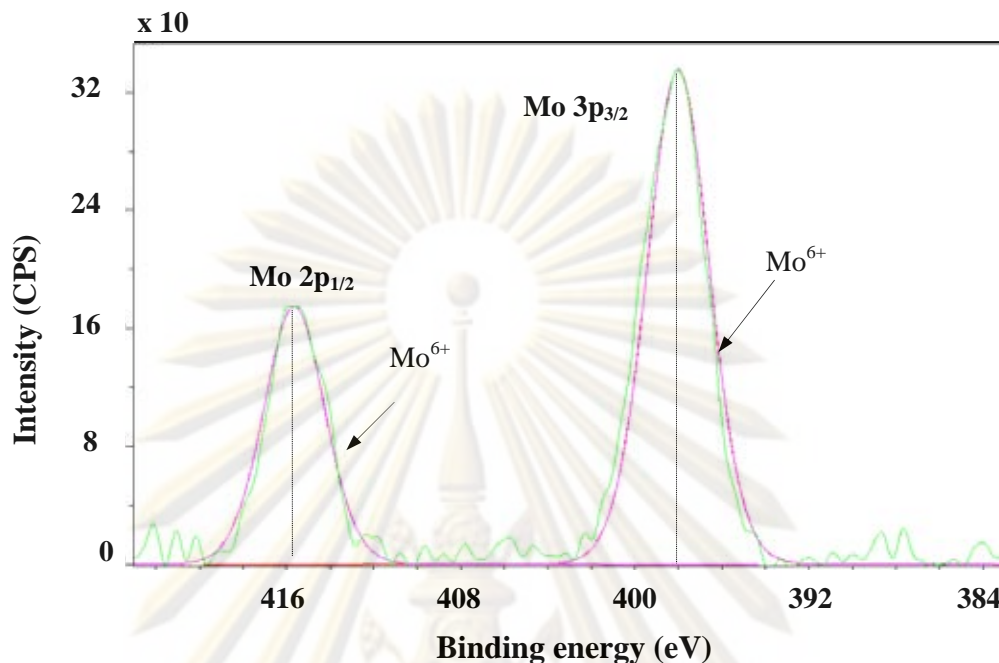
Figure 4.30 Mo 3d XPS spectra of Mo-TiO$_2$ that contained 10 mol% Mo.

4.4.3 Molybdenum content in Mo-TiO$_2$

The amount of molybdenum contents in Mo-TiO$_2$ sample was determined using inductively coupled-plasma optical emission spectroscopy (ICP-OES) and the results are shown in Table 4.17. As seen in Table 4.17, the real mole percentages of molybdenum were found in Mo-TiO$_2$ samples was higher than that the expected values only slightly.

Table 4.17 The amount of molybdenum contents in Mo-TiO$_2$.

Amount of molybdenum loading (mol%)	Amount of molybdenum from ICP (mol%)
0.1	0.113
0.3	0.346
0.5	0.570
0.7	0.745
1.0	1.163

4.4.4 Specific surface area of Mo-TiO$_2$

The most common procedure for determining surface area of a solid is based on adsorption and condensation of nitrogen at liquid nitrogen temperature using static vacuum procedure. This method is also called BET (Brunauer Emmett Teller) method. Specific surface areas of Mo-TiO$_2$ at various amount of molybdenum loading were listed in Table 4.18. Specific surface area of TiO$_2$ was 103.8 m^2/g. After molybdenum loading, surface areas were decreased. However, the amount of molybdenum loading did not have a significant effect on the specific surface area, which was appeared in the range of 80.8-89.4 m^2/g.

4.4.5 Surface morphology of Mo-TiO$_2$ thin films

AFM was used to characterize the morphology and uniformly of surface. Figure 4.31 shows AFM images of Mo-TiO$_2$ film surface that contained various amount of molybdenum. It was observed that, that loading of molybdenum into TiO$_2$ did not have a significant effect on the grain size of TiO$_2$. Analysis of AFM images suggested that average roughness of the Mo-TiO$_2$ films surface appeared in the range of 1.693-2.960 nm (see Table 4.19).

Table 4.18 Specific surface area of Mo-TiO$_2$ at various amount of molybdenum loading.

Amount of molybdenum loading (mol%)	Specific surface area (m^2/g)
0.0	103.8
0.1	83.6
0.3	81.9
0.5	80.8
0.7	89.4
1.0	84.9

4.4.6 Light absorption characteristic of Mo-TiO$_2$ thin films

Figure 4.32 show UV-Vis absorption spectra of Mo-TiO$_2$ films in wavelength range of 300-700 nm. All films showed transmittance of light over 80 % in visible region. The fast decreased in transmittance below 380 nm is due to absorption of light, which was caused by the excitation of electrons from the valance band to conduction of TiO$_2$ (Yu et al., 2002). When increased molybdenum loading, the absorption edge of Mo-TiO$_2$ films were shifted toward longer wavelength (red-shifted), this indicated that decreasing in band gap energy. To calculate the band gap energy of Mo-TiO$_2$ film, the graph of $(-2.303 h \upsilon \log T)^{1/2}$ versus $h\upsilon$ was plotted and extrapolated in a linear part leading to the band gap energy (see in APPENDIX D). It was found that the band gap energies of TiO$_2$ and TiO$_2$ that contained molybdenum of 0.1, 0.3, 0.5, 0.7, and 1.0 were 3.23, 3.20, 3.20, 3.18, 3.17 mol% and 3.16 respectively.
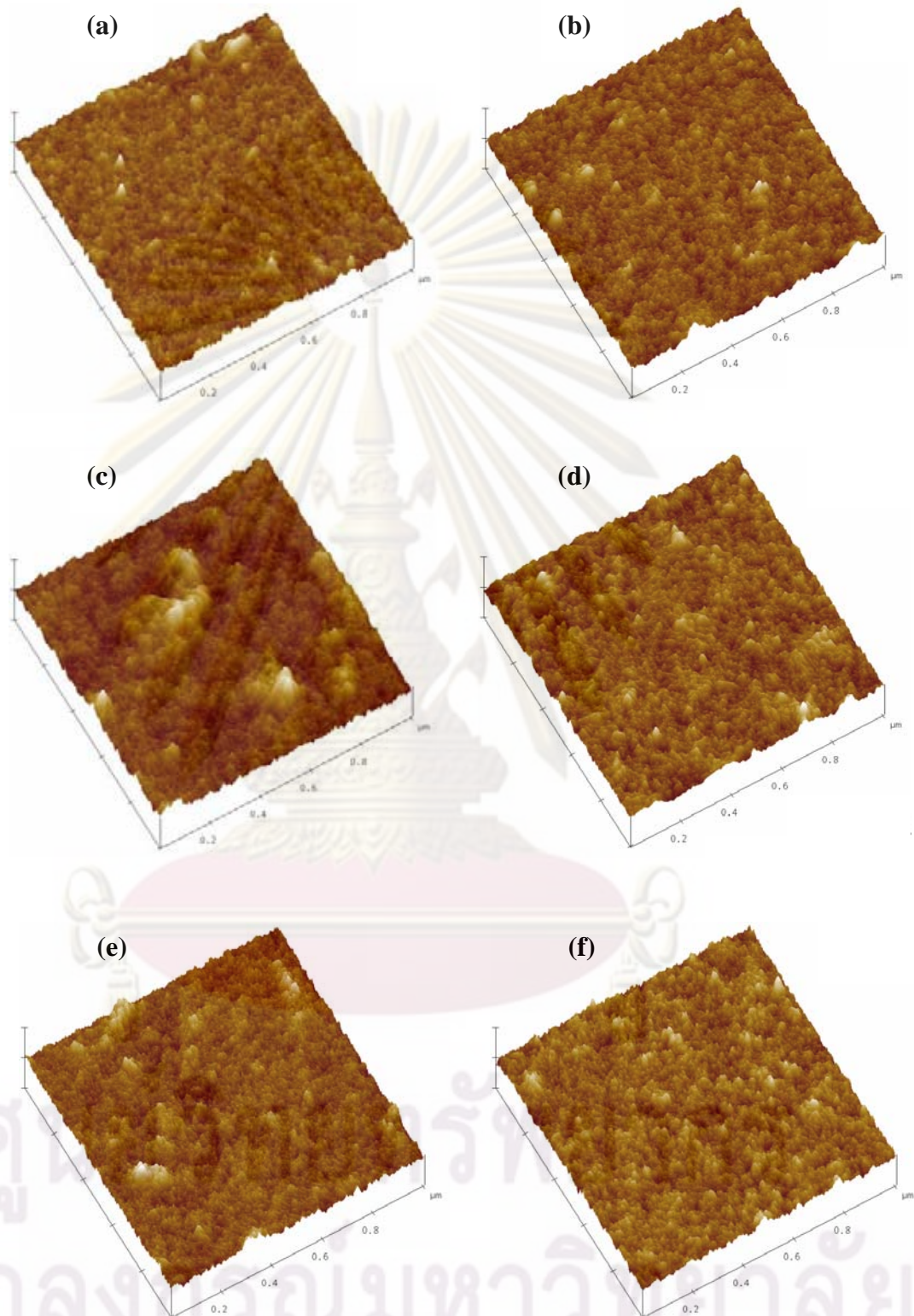
Figure 4.31 AFM images of Mo-TiO$_2$ film surface that contained (a) 0.0 mol%, (b) 0.1 mol%, (c) 0.3 mol%, (d) 0.5 mol%, (e) 0.7 mol%, and (f) 1.0 mol % Mo.

Table 4.19 Average roughness of Mo-TiO$_2$ films as determined from AFM images.

Amount of molybdenum loading (mol%)	Average roughness (RMS) (nm)
0.0	1.864
0.1	1.693
0.3	2.960
0.5	1.766
0.7	2.061
1.0	1.853
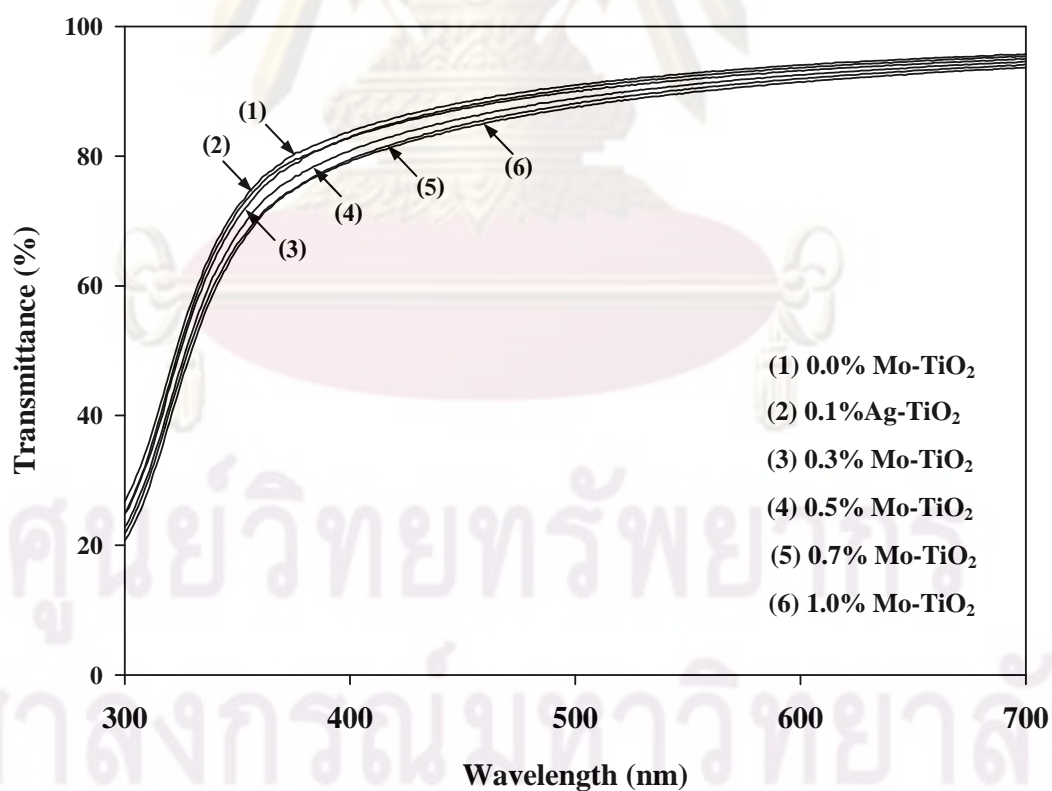
Figure 4.32 UV-Vis spectra of Mo-TiO$_2$ thin films coated on glass surface.

4.4.7 Surface acidity of Mo-TiO$_2$

Temperature-programmed desorption (TPD) of probe molecules like ammonia and pyridine is a popular method for determining the acidity of solid catalysts as well as acid strength sites (Yang et al, 2005). In this investigation, the acidity measurement was carried out using NH$_3$-TPD. In Figure 4.33 presents NH$_3$-TPD profiles of Mo-TiO$_2$ with various amount of molybdenum loading. There was only one asymmetric broad peak on the NH$_3$-TPD profiles of all the samples, and the peak temperatures are ranged between 50 and 600 °C, indicating that the acid sites of the samples were weak and strong strength (Yang et al, 2005 and Yoon et al., 2007). The total acid sites of Mo-TiO$_2$ were listed in Table 4.20. After molybdenum loading, total acid site decreased. However, the amount of molybdenum loading did not have a significant effect on the surface acidity of Mo-TiO$_2$.
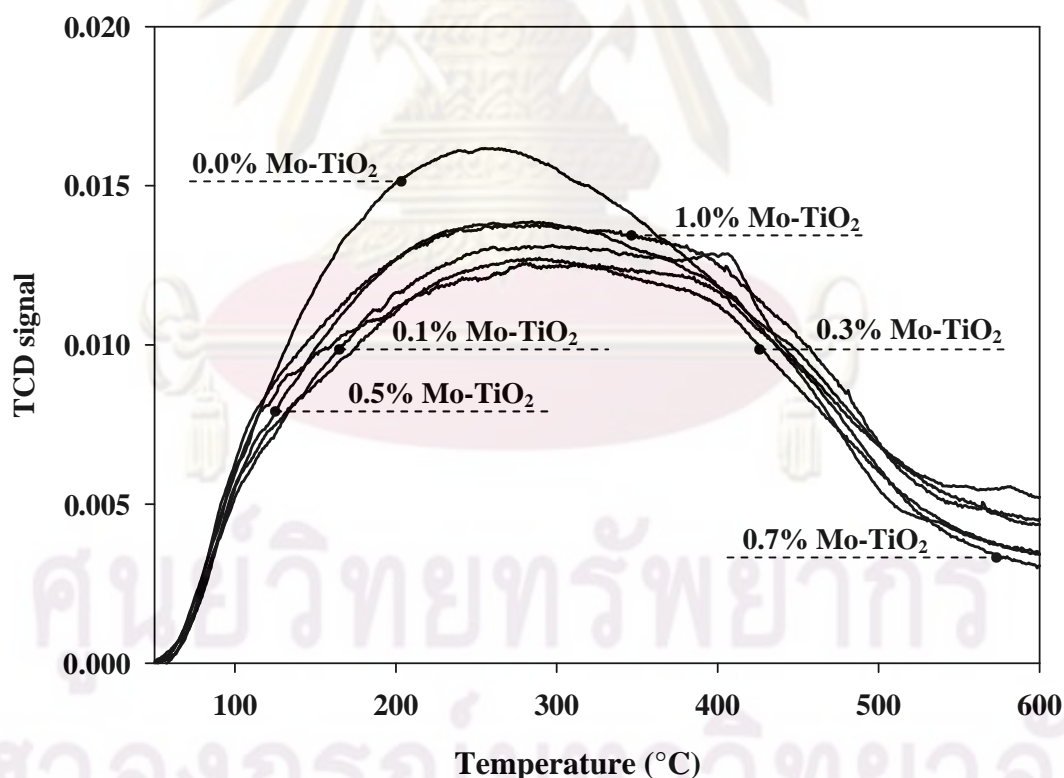
Figure 4.33 NH$_3$-TPD profiles of Mo-TiO$_2$ at various amount of molybdenum loading.

Table 4.20 Surface acidity of Mo-TiO$_2$ samples as determined from NH$_3$-TPD
profiles.

Amount of molybdenum loading (mol%)	Total acid site (mmol NH$_3$/g)
0.0	21.24
0.1	17.71
0.3	17.25
0.5	17.73
0.7	18.18
1.0	18.93

4.4.8 Photoluminescence spectra of Mo-TiO$_2$

The photoluminescence (PL) emission spectra have been widely used
to investigate the efficiency of charge carrier trapping, immigration and transfer, and
to understand the fate of electron-hole pairs in semiconductor particles (Li et al.,
2001). The PL emission mainly results from the recombination of photo-induced
electros and holes. The lower PL intensity indicates that the decreasing in
recombination rate. In Figure 4.34 shows PL of Mo-TiO$_2$ at various amount of Mo
loading. It was observed that, PL spectra exhibited two emission peaks at the
wavelength of about 420 and 485 nm. The former peak was due to free excitation
emission of TiO$_2$ and the latter peak was due to the surface state such as Ti^{4+}-OH
(Nagaveni et al., 2004). As seen Figure 4.34, the photoluminescence intensity
decreased with increasing the loading of molybdenum. This was attributed to
molybdenum species can act as traps for photo-induced electrons. Therefore, the
photo-generated electron-hole pairs were effectively separated rather than undergoing
recombination. This reason caused the decreasing in PL intensity after loading of
molybdenum to TiO$_2$.
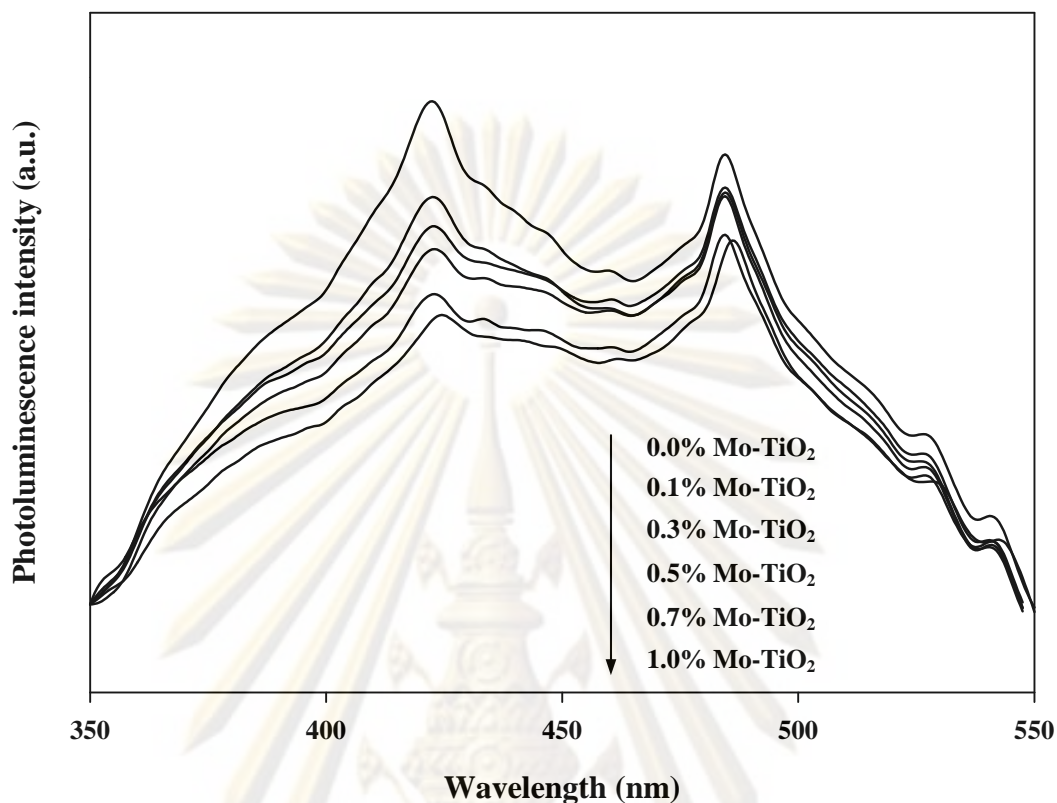
Figure 4.34 PL spectra of Mo-TiO$_2$ at various amount of molybdenum loading.

4.4.9 Photo-induced hydrophilicity of Mo-TiO$_2$ films

In figure 4.35 shows the changes in water contact angle of Mo-TiO$_2$ film after UV irradiation for 3 hours. Before irradiation, the films had the initial contact angle about 18-21 degrees. When the films being were irradiated, the contact angle gradually decreased until the angle reached to a steady state value, called saturated contact angle. For TiO$_2$ film, the time needed to reach a saturated contact angle about 5 degrees approximately 120 minutes. When increased Mo loading, the saturated contact angle of all Mo-TiO$_2$ films about 10 degrees, which higher than that TiO$_2$ films. So Mo-TiO$_2$ film possessed worse hydrophilic properties than TiO$_2$ film did. This was attributed to the ability of molybdenum to captures photo-induced electrons is higher than that to produces surface oxygen vacancies on TiO$_2$ surface according to the mechanism of photo-induced hydrophilicity. Therefore, the lower surface oxygen vacancies were created, which brought about lower hydrophilic

properties of Mo-TiO$_2$ films. Furthermore, MoO$_3$ itself does not exhibit hydrophilicity (Miyayuchi, 2002). Thus, with increasing content of molybdenum loading, the hydrophilicity of Mo-TiO$_2$ films decreased comparatively to TiO$_2$ film.

4.1.10 The sustainability of hydrophilicity of the films after removal of UV irradiation

In order to assess the sustainability of hydrophilic property of Mo-TiO$_2$ film, the films were placed in a dark place with no exposure to light. As seen in Figure 4.36, the ability to retain the hydrophilic property of Mo-TiO$_2$ films after removal of UV irradiation was worse than that of TiO$_2$ film. These findings agreed with observation previously mentioned that the film with better hydrophilic property could retain the hydrophilic property longer.
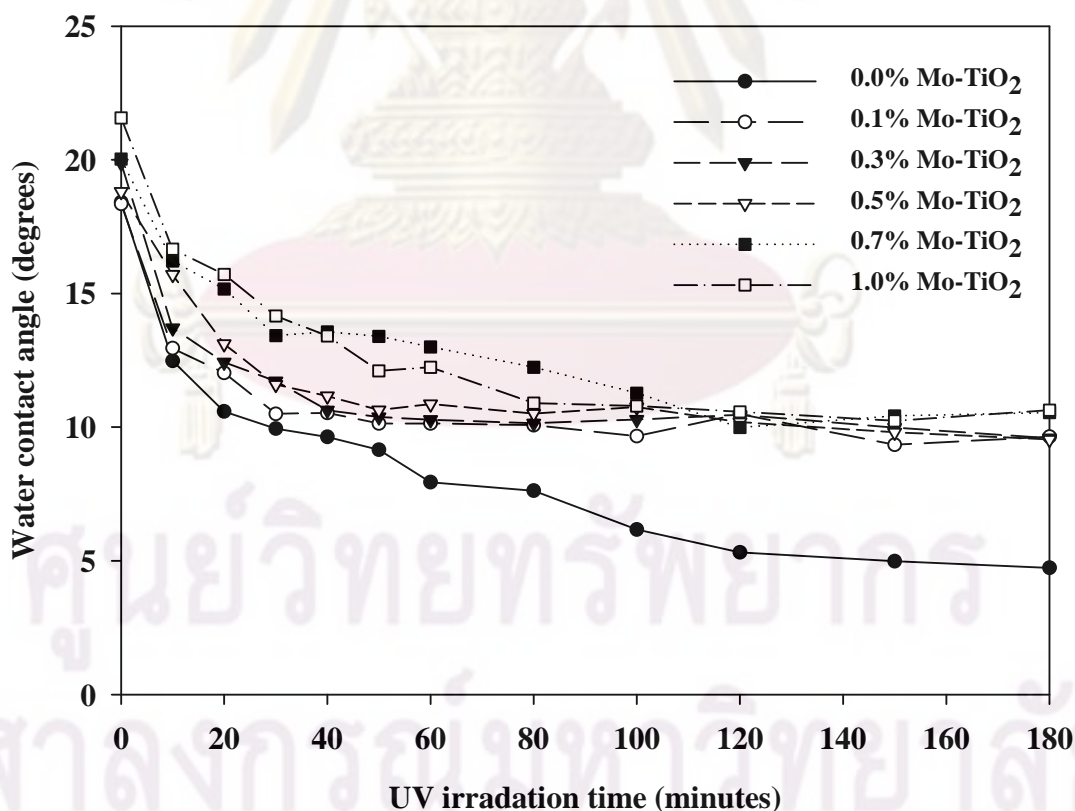
Figure 4.35 Change in contact angle of water droplet on the surface of various Mo-TiO$_2$ films.
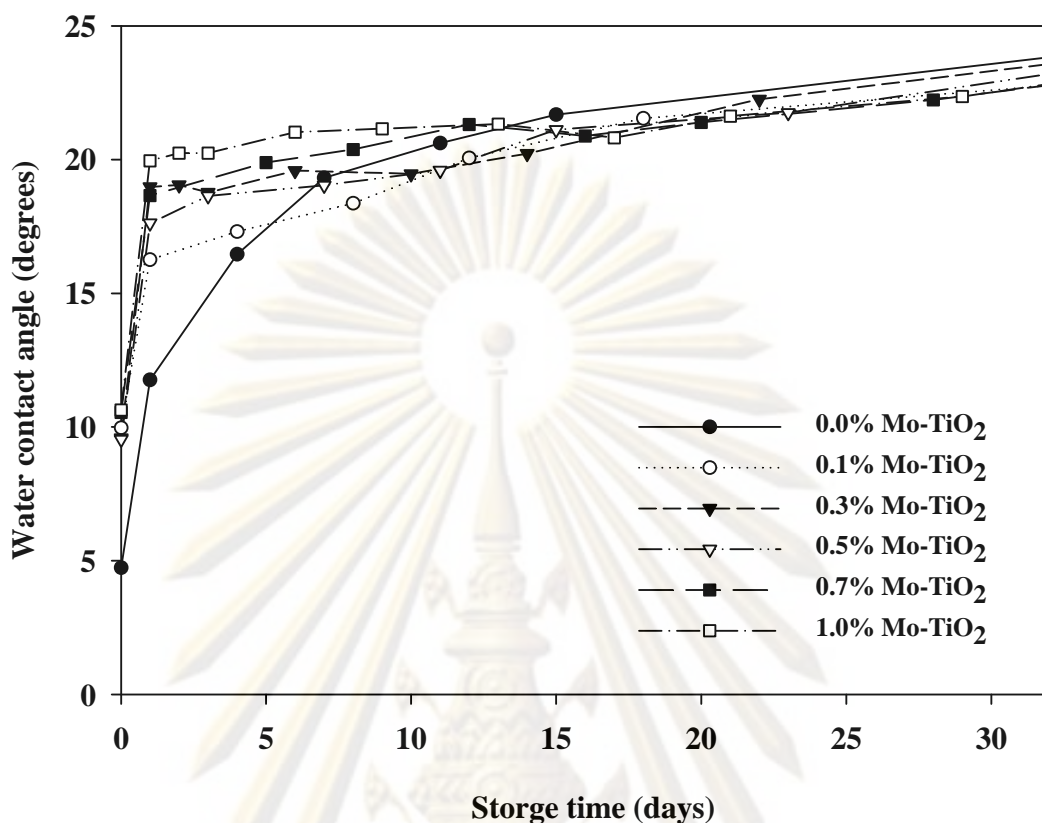
Figure 4.36 Change in contact angle of water droplet on the surface of various Mo-TiO$_2$ films in the absence of UV irradiation.

4.5 Reduction behavior of metal loaded-TiO$_2$

According to the result of photo-induced hydrophilicity, adding of silver or tungsten enhanced the hydrophilic property of the films but neither adding of copper or molybdenum did not enhance the hydrophilic property. In order to investigate the overall conclusion of metal loading to the hydrophilic property of the film that may be correlated to the reduction behavior of metal species. Therefore, temperature programmed-reduction (TPR) was performed and the result of the TPR profiles of Ag-, W-, Cu-, and Mo-TiO$_2$ were shown in Figure 4.37. As seen in the TPR profile of Ag-TiO$_2$, the reduction peak was observed at the temperature around 100 °C which was due to the reduction of dispersed Ag$^+$ species (Nanba et al., 2008). For W-TiO$_2$ sample, only one reduction peak was observed at the temperature around 520 °C. This peak was due to the reduction of W^{6+} to W^{5+} and then to W^{4+} (Engweiler et al. 1996 and Benitez et al., 2002). Moreover, the tail of the TPR profile does not reach to the

base line at the end of experiment. This was due to further reduction to W^0 at the temperature higher than 800 °C. For Cu-TiO$_2$ sample, two reduction peaks were observed at the temperature around 260 °C and 406 °C. The former peak was due to the reduction of highly dispersed CuO species interacting with TiO$_2$ and the letter peak was due to the reduction from bulk CuO crystallites (Xiaoyuan et al, 2004 and Luo et al., 2005). For Mo-TiO$_2$ sample, two steps of reduction were observed at the temperatures around 445 °C and 776 °C. This two reduction peaks were due to the reduction of Mo^{6+} in both tetrahedral and octahedral coordinate to Mo^{4+} (Arnoldy et al., 1984 and Chary et al., 2001). Moreover, the reduction peak of Mo^{4+} to Mo^0 will be appeared at the temperature higher than 800 °C, which cannot observe in this experiment condition. According to the result from the TPR profile and photo-induced hydrophilicity, if the reduction behavior (easy to reduce) has been correlate with the hydrophilic property, the reduction should be in the order of Cu-TiO$_2$~Mo-TiO$_2$> Ag-TiO$_2$~W-TiO$_2$. However, as seen in Figure 4.37, the reduction was in the order of Ag-TiO$_2$>Cu-TiO$_2$>Mo-TiO$_2$>W-TiO$_2$ respectively. Thus, the reduction behavior of metal species did not correlated to the hydrophilic property of the film.
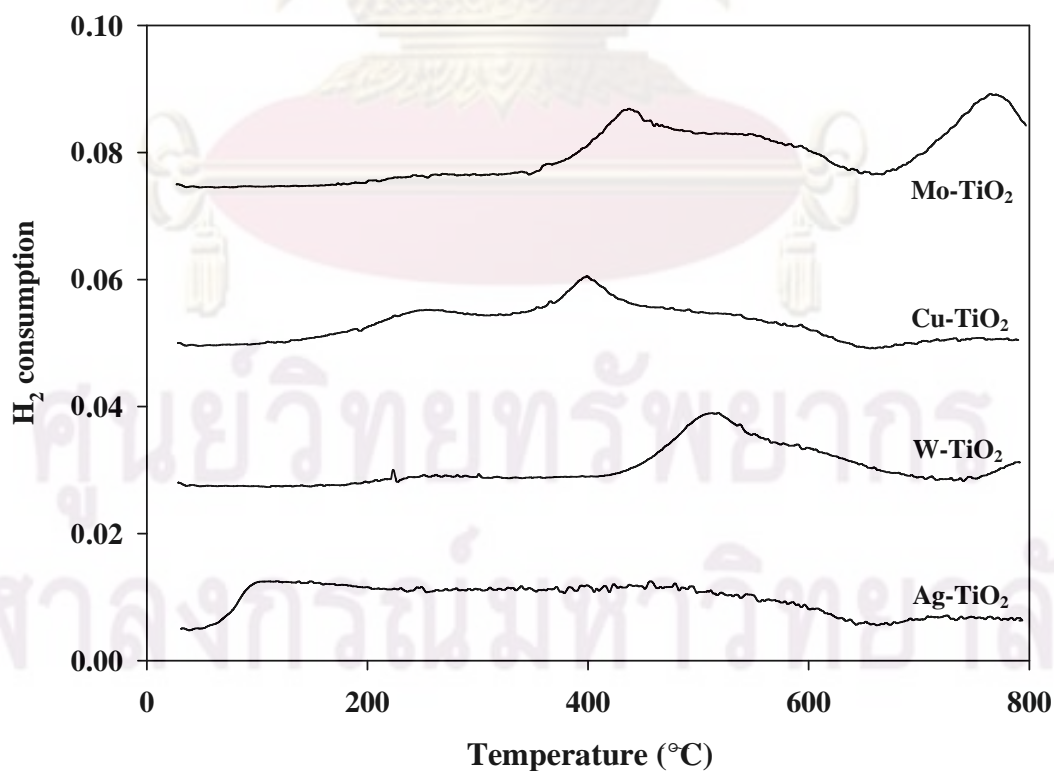
Figure 4.37 TPR profiles of metal loaded-TiO$_2$ that contained 1.0 mol% metal.

CHAPTER V

CONCLUSIONS AND RECOMMENDATIONS

5.1 Conclusions

In this study, to investigate the effect of metal (Ag, W, Cu, or Mo) loading to TiO_2 on photo-induced hydrophilicity of TiO_2 thin films and their abilities to retain hydrophilicity after removal of UV irradiation. The overall conclusions are the following;

5.1.1 TiO_2 film containing 3.0-5.0 mol% silver or 1.0-1.5 mol% tungsten possessed the best hydrophilic properties because the recombination of photo-generated electrons and holes were effectively inhibited, which agreed with the results from photoluminescence spectra.

5.1.2 Adding of copper (0.1-5.0 mol%) and molybdenum (0.1-1.0 mol%) to TiO_2 films did not improve the hydrophilicity of the thin films because the photo-generated electrons were captured by their metal oxide instead of creating surface oxygen vacancies on TiO_2 surface. Furthermore, neither CuO nor MoO_3 possessed hydrophilicity. An increase in the content of copper or molybdenum in TiO_2 worsened the hydrophilic property of the film.

5.1.3 The better the hydrophilic property of the thin film, the longer the ability of the thin film to retain its hydrophilicity after removal UV irradiation.

5.2 Recommendations

The following recommendations for future studies are proposed.

5.2.1 The film sample was used in another application such as decomposition the hydrocarbon compound, treats the water and air pollution.

5.2.2 Other preparation for prepare TiO_2 thin film should be tried.

REFFERENCE

Arnoldy, P., Jonge, J. C. M., and Moulijn, J. A. Temperature-programed reduction of molybdenum (VI) oxide and molybdenum (IV) oxide. The Journal of Physical Chemistry 89 (1985): 4517–4526.

Bellardita, M., Addamo, M., Paola, A. D., and Palmisano, L. Photocatalytic behaviour of metal-loaded TiO_2 aqueous dispersions and films. Chemical Physics 339 (2007): 94–103.

Benitez, V. M. and Figoli, N. S. About the importance of surface W species in WO_x/Al_2O_3 during n-butene skeletal isomerization. Catalysis Communications 3 (2002): 487–492.

Chai, S. Y., Kim, Y. J., and Lee, W. I. Photocatalytic WO_3/TiO_2 nanoparticles working under visible light. Journal of Electroceramics 17 (2006): 909–912.

Chary, K. V. R., Reddy, K. R., and Kumar C. P. Dispersion and reactivity of molybdenum oxide catalysts supported on titania. Catalysis Communications 2 (2001): 277–284.

Choi, H. J. and Kang, M. Hydrogen production from methanol/water decomposition in a liquid photosystem using the anatase structure of Cu loaded TiO_2. International Journal of Hydrogen Energy 32 (2007): 3841–3848.

Colo´n, G., Maicu, M., Hidalgo, M. C., and Navı´o, J. A. Cu-doped TiO_2 systems with improved photocatalytic activity. Applied Catalysis B: Environmental 67 (2006): 41–51.

Djaoued, Y., Thibodeau, M., Robichaud, J., Balaji, S., Priya, S., Tchoukanova, N., and Bates, S .S. Photocatalytic degradation of domoic acid using nanocrystalline TiO_2 thin films. Journal of Photochemistry and Photobiology A: Chemistry 193 (2008): 271–283.

Du, Y. K., Gan, Y. Q., Yang, P., Zhao, F., Hua, N. P., and Jiang, L. Improvement in the heat-induced hydrophilicity of TiO_2 thin films by doping Mo(VI) ions. Thin Solid Films 491 (2005): 133–136.

Engweiler, J., Harf, J., and Baiker, A. WO$_x$/TiO$_2$ catalysts prepared by grafting of tungsten alkoxides: morphological properties and catalytic behavior in the selective reduction of NO by NH$_3$. Journal of catalysis 159 (1996): 259–269.

Fujishima, A., Rao, T. N., and Tryk, D. A. Titanium dioxide photocatalysis. Journal of Photochemistry and Photobiology C: Photochemistry Reviews 1 (2000): 1–21.

Fujishima, A. and Zhang, X. Titanium dioxide photocatalysis: present situation and future approaches. Comptes Rendus Chimie 9 (2006): 750–760.

Fujishima, A., Zhang, X., and Tryk, D. A. TiO$_2$ photocatalysis and related surface phenomena. Surface Science Reports 63 (2008): 515–582.

Gennes, P. G. Wetting: statics and dynamics. Reviews of Modern Physics 57 (1985): 827–863.

Guan, K. Relationship between photocatalytic activity, hydrophilicity and self-cleaning effects of TiO$_2$/SiO$_2$ films. Surface & Coating Technology 191 (2005): 155–160.

He, C., Yu, Y., Hu, X., and Larbot, A. Influence of silver doping on the photocatalytic activity of titania films. Applied Surface Science 200 (2002): 239–274.

Hou, X. G., Huanga, M. D., Wub, X. L., and Liub, A. D. Preparation and studies of photocatalytic silver-loaded TiO$_2$ films by hybrid sol–gel method. Chemical Engineering Journal 146 (2009): 42–48.

Irie, H. and Hashimoto, K. Photocatalytic active surfaces and photo-induced high hydrophilicity/high hydrophobicity. The Handbook of Environmental Chemistry 2 (2005): 425–450.

Iwasaki, M., Hara, M., Kawada, H., Taday, H., and Ito, S. Cobalt ion-doped TiO$_2$ photocatalyst response to visible light. Journal of Colloid and Interface Science 224 (2000): 202–204.

Jiang, X. and Chen, X. Crystallization behavior and hydrophilic performances of V$_2$O$_5$–TiO$_2$ films prepared by sol–gel dip-coating. Journal of Crystal Growth 270 (2004): 547–552.

Jing, H. and Gao, L. Enhancing the UV inducing hydrophilicity of TiO$_2$ thin film by doping Fe ions. Material Chemistry and Physics 77 (2002): 878–881.

Ke, D., Liu, H., Peng, T., Liu, X., and Dai, K. Preparation and photocatalytic activity of WO_3/TiO_2 composite particles. Material Letters 62 (2008): 447–450.

Lee, Y. C., Hong, Y. P., Lee, H. Y., Kim, H., Jin, J. Y., Ko, K. H., Jung, H. S., and Hong, K. S. Photocatalysis and hydrophilicity of doped TiO_2 thin films. Journal of Colloid and Interface Science 267 (2003): 127–131.

Li, H., Zhao, G., Han, G., and Song, B. Hydrophilicity and photocatalysis of $Ti_{1-x}V_xO_2$ films prepared by sol–gel method. Surface & Coatings Technology 201 (2007): 7615–7618.

Li, J., Liu, L., Yu, Y., Tang, Y., Li, H., and Du, F. Preparation of highly photocatalytic active nano-size TiO_2–Cu_2O particle composites with a novel electrochemical method. Electrochemistry Communications 6 (2004): 940–943.

Linsebigler, A. L., Lu, G., and Yates, J. T. J. Photocatalysis on TiO_2 surfaces: principles, mechanisms, and selected Results. Chemical Reviews 95 (1995): 735–758.

Liqiang, J., Yichuna, Q., Baiqia, W., Shudana, Li, Baojianga, J., Libina, Y., Wei, F., Honggang, F., and Jiazhong, S. Review of photoluminescence performance of nano-sized semiconductor materials and its relationships with photocatalytic activity. Solar Energy Materials & Solar Cells 90 (2006): 1773–1787.

Litter, M. I. Heterogeneous photocatalysis Transition metal ions in photocatalytic suystems. Applied Catalysis B: Environmental 23 (1999): 89–114.

Li, X. Z., Li, F. B., Yang, C. L., and Ge, W. K. Photocatalytic activity of WO_x-TiO_2 under visible light irradiation. Journal of Photochemistry and Photobiology A: Chemistry 141 (2001): 209–217.

Luo, M., F., Fang, P., He, M., and Xie, Y. L. In situ XRD, Raman, and TPR studies of CuO/Al_2O_3 catalysts for CO oxidation. Journal of Molecular Catalysis A: Chemical 239 (2005): 243–248.

Mardare, D., Tasca, M., Delibas, M., and Rusu, G.I. On the structural properties and optical transmittance of TiO_2 r.f. sputtered thin films. Applied Surface Science 156 (2000): 200–206.

Miyauchi, M., Nakajima, A., Fujishima, K. Hashimoto, K., and Watanabe, T. Photoinduced surface reactions on TiO_2 and $SrTiO_3$ films: photocatalytic

oxidation and photoinduced hydrophilicity. Chemistry of Materials 12 (2000): 3–5.

Miyauchi, M., Nakajima, A., Watanabe, T., and Hashimoto, K. Photocatalysis and photoinduced hydrophilicity of various metal oxide thin films. Chemistry of Materials 14 (2002): 2812-2816.

Nagaveni, K, Hegde, M. S., and Madras G. Structure and Photocatalytic activity of $Ti_{1-x}M_xO_{2\pm\delta}$ (M = W, V, Ce, Zr, Fe, and Cu) synthesized by solution combustion method. The Journal of Physical Chemistry B 108 (2004): 20204-20212.

Nanba, T., Masukawa, S., Uchisawa J., and Obuchi, A. Effect of support materials on Ag catalysts used for acrylonitrile decomposition. Journal of Catalysis 259 (2008): 250–259.

Ohara, C., Hongo, T., Yamazaki, A., and Nagoya, T. Synthesis and characterization of brookite/anatase complex thin film. Applied Surface Science 254 (2008): 6619–6622.

Paola, A. D., Garcia-Lopez, E., Marcia, G., Martin, C., Palmisano, L., Rives, V., and Venezia, A. M. Surface characterisation of metal ions loaded TiO_2 photocatalysts: structure–activity relationship. Applied Catalysis B: Environmental 48 (2004): 223–233.

Sakai, N., Fujishima, A., Watanabe, T., and Hashimoto, K. Enhancement of the photoinduced hydrophilic conversion rate of TiO_2 film electrode surfaces by anodic polarization. The Journal of Physical Chemistry B 105 (2001): 3023–3026.

Sakai, N., Fujishima A., Watanabe, T., and Hashimoto, K. Quantitative evaluation of the photoinduced hydrophilic conversion properties of TiO_2 thin film surfaces by the reciprocal of contact angle. The Journal of Physical Chemistry B 107 (2003): 1028–1035.

Sakai, N., Wang, R., Fujishima, A., Watanabe, T., and Hashimoto, K. Effect of ultrasonic treatment on highly hydrophilic TiO_2 surfaces. Langmuir 14 (1998): 5918–5920.

Sakthivela, S., Shankarb, M. V., Palanichamy, M., Arabindoob, B., Bahnemanna, D. W., and Murugesan, V. Enhancement of photocatalytic activity by metal

deposition: characterisation and photonic efficiency of Pt, Au and Pd deposited on TiO$_2$ catalyst. Water Research 38 (2004): 3001–3008.

Sharma, S. D., Singh, D., Saini, K. K, Kant, C., Sharma, V., Jain, S. C., and Sharma, C. P. Sol–gel-derived super-hydrophilic nickel doped TiO$_2$ film as active photo-catalyst. Applied Catalysis A: General 314 (2006): 40–46.

Shen, Y., Xiong, T., Li, T., and Yang, K. Tungsten and nitrogen co-doped TiO2 nano-powders with strong visible light response. Applied Catalysis B: Environmental 83 (2008): 177–185.

Sonawane, R. S., Kale, B. B., and Dongare, M. K. Preparation and photo-catalytic activity of Fe–TiO$_2$ thin films prepared by sol–gel dip coating. Materials Chemistry and Physics 85 (2004): 52–57.

Song, H., Jiang, H., Liu, X., and Meng, G. Efficient degradation of organic pollutant with WOx modified nano TiO$_2$ under visible irradiation. Journal of Photochemistry and Photobiology A: Chemistry 181 (2006): 421–428.

Su, C., Hong, B. -Y., and Tseng, C. -M. Sol–gel preparation and photocatalysis of titanium dioxide. Catalysis Today 96 (2004): 119–126.

Sun, R. D., Nakajima, A., Fujishima, A., Watanabe, T., and Hashimoto, K. Photoinduced surface wettability conversion of ZnO and TiO$_2$ thin films. The Journal of Physical Chemistry B 105 (2001): 1984–1990.

Tian, H., Ma, J., Li, K., and Li, J. Photocatalytic degradation of methyl orange with W-doped TiO$_2$ synthesized by a hydrothermal method. Materials Chemistry and Physics 112 (2008): 47–51.

Wang, R., Sakai, N., Fujishima A., Watanabe, T., and Hashimoto, K. Studies of surface wettability conversion on TiO$_2$ single-crystal surfaces. The Journal of Physical Chemistry B 103 (1999): 2188-2194.

Wang, W., Zhang, J., Huang, H., Wu, Z., Zhang, Z. Investigation of monolayer dispersion of MoO$_3$ supported on titanate nanotubes. Applied Surface Science 254 (2008): 1725–1729.

Wang, X. P., Yu, Y., Hu, X. F., and Gao L. Hydrophilicity of TiO$_2$ films prepared by liquid phase deposition. Thin Solid Films 371 (2000): 148–152.

Weng, W., Ma, M., Du, P., Zhao, G., Shen, G., Wang, J., and Han, G. Superhydrophilic Fe doped titanium dioxide thin films prepared by a spray pyrolysis deposition. Surface & Coatings Technology 198 (2005): 340– 344.

Xiaoyuan, J., Guanghui, D., Liping, L., Yingxu, C., and Xiaoming Z. Catalytic activities of CuO/TiO_2 and $CuO-ZrO_2/TiO_2$ in NO + CO reaction. Journal of Molecular Catalysis A: Chemical 218 (2004): 187–195.

Xia, X. H., Gao, Y., Wang, Z., and Jia, Z. J. Structure and photocatalytic properties of copper-doped rutile TiO_2 prepared by alow-temperature process. Journal of Physicsand Chemistry of Solids 69 (2008): 2888–2893.

Xin, B., Jing, L., Ren, Z., Wang, B., and Fu, Honggang. Effects of simultaneously doped and deposited Ag on the photocatalytic activity and surface states of TiO_2. The Journal of Physical Chemistry B 109 (2005): 2805-2809.

Xin, B., Ren, Z., Hu, H., Zhang, X, Dong, C., Shi, K., Jing, L., and Fu, H. Photocatalytic activity and interfacial carrier transfer of $Ag–TiO_2$ nanoparticle films. Applied Surface Science 252 (2005): 2050–2055.

Xin, B., Ren, Z., Wang, P., Liu, J., Jing, Li., and Fu, H. Study on the mechanisms of photoinduced carriers separation and recombination for $Fe^{3+}–TiO_2$ photocatalysts. Applied Surface Science 253 (2007): 4390–4395.

Xin, B., Wang, P., Ding, D., Liu, J., Ren, Z., and Fu, H. Effect of surface species on $Cu-TiO_2$ photocatalytic activity. Applied Surface Science 254 (2008): 2569–2574.

Xu, Y. H, Liang, D. H., Liu, M. L., and Liu, D. Z. Preparation and characterization of $Cu_2O–TiO_2$: Efficient photocatalytic degradation of methylene blue. Materials Research Bulletin 43 (2008): 3474–3482.

Yang, X. L., Dai, W. L., Guo, C., Chena, H., Cao, Y., Li, H., He, H., and Fan, K. Synthesis of novel core-shell structured WO_3/TiO_2 spheroids and its application in the catalytic oxidation of cyclopentene to glutaraldehyde by aqueous H_2O_2. Journal of Catalysis 234 (2005): 438–450.

Yang, X., Xu, L., Yu, X., and Guo, Y. One-step preparation of silver and indium oxide co-doped TiO_2 photocatalyst for the degradation of rhodamine B. Catalysis Communications 9 (2008): 1224–1229.

Yuan, Z., Zhang, J., Li, B., and Li, J. Effect of metal ion dopants on photochemical properties of anatase TiO_2 films synthesized by a modified sol-gel method. Thin Solid Films 515 (2007): 7091–7095.

Yu, J. C., Yu, J., Ho, W., and Zhao, J. Light-induced super-hydrophilicity and photocatalytic activity of mesoporous TiO_2 thin films. Journal of Photochemistry and Photobiology A: Chemistry 148 (2002a): 331–339.

Yu, J. G., Yu, H. G., Cheng, B., Zhao, X. J., Yu, J. C., and Ho, W. K. The effect of calcination temperature on the surface microstructure and photocatalytic activity of TiO_2 thin films prepared by liquid phase deposition. The Journal of Physical Chemistry B 107 (2003): 13871-13879.

Yu, J., Xiong, J., Cheng, B., and Liu, S. Fabrication and characterization of Ag–TiO_2 multiphase nanocomposite thin films with enhanced photocatalytic activity. Applied Catalysis B: Environmental 60 (2005): 211–221.

Yu, J., Yu, C., J., Ho, W., and Jianga, Z. Effects of calcination temperature on the photocatalytic activity and photo-induced super-hydrophilicity of mesoporous TiO_2 thin films. New Journal of Chemistry 26 (2002b): 607–613.

Yu, J. and Zhao, X. Effect of surface treatment on the photocatalytic activity and hydrophilic property of the sol-gel derived TiO_2 thin films. Materials Research Bulletin 36 (2001): 97–107.

Yu, J., Zhao, X., Zhao, Q., and Wang, G. Preparation and characterization of super-hydrophilic porous TiO_2 coating films. Materials Chemistry and Physics 68 (2001): 253–259.

Yu, J., Zhou, M., Yu, H., Zhang, Q., and Yu, Y. Enhanced photoinduced super-hydrophilicity of the sol–gel-derived TiO_2 thin films by Fe-doping. Materials Chemistry and Physics 95 (2006): 193–196.

Zheng, J., Yu, H., Li, X., and Zhang, S. Enhanced photocatalytic activity of TiO_2 nano-structured thin film with a silver hierarchical configuration. Applied Surface Science 254 (2007): 1630–1635.

APPENDICES

APPENDIX A

CALCULATION OF THE CRYSTALLITE SIZE

Calculation of the crystallite size

The crystallite size was calculated from the width at half-height of the diffraction peak of XRD pattern using the Debye-Scherrer formula according to Equation A.1;

$$D = \frac{K\lambda}{\beta \cos\theta} \tag{A.1}$$

where D is crystallite size (Å)

  K is crystallite-shape factor (0.9)

  λ is X-ray wavelength (1.5418 Å for Cu Kα)

  θ is diffraction angle (degree)

  β is X-ray diffraction broadening (radian)

The X-ray diffraction broadening (β) is the pure width of a powder diffraction, free of all broadening due to the experimental equipment. Standard α-alumina is used to observe the instrumental broadening since its crystallite size is larger than 2000 Å. The X-ray diffraction broadening (β) can be obtained by using Warren's formula;

$$\beta^2 = B_M^2 - B_S^2 \tag{A.2}$$

$$\beta = \sqrt{B_M^2 - B_S^2}$$

where B_M is the measured peak width in radians at half peak height

  B_S is the corresponding width of a standard material

Example: Calculation of the crystallite size of titanium dioxide.

In Figure A.1, the half-height width of 101 diffraction peak

$$= 1.80813^o$$

$$= 0.03156 \text{ radian}$$

The corresponding half-height width of peak $= 0.004 \text{ radian}$

The pure width $= \sqrt{B_M^2 - B_S^2}$

$$= \sqrt{0.03156^2 - 0.004^2}$$

$$= 0.03132 \text{ radian}$$

$\beta = 0.03132 \text{ radian}$

$2\theta = 25.28^o$

$\theta = 12.64^o$

$\lambda = 1.5418 \text{ Å}$

The crystallite size $= \dfrac{0.9 \times 1.5418}{0.03132 \cos 12.64}$

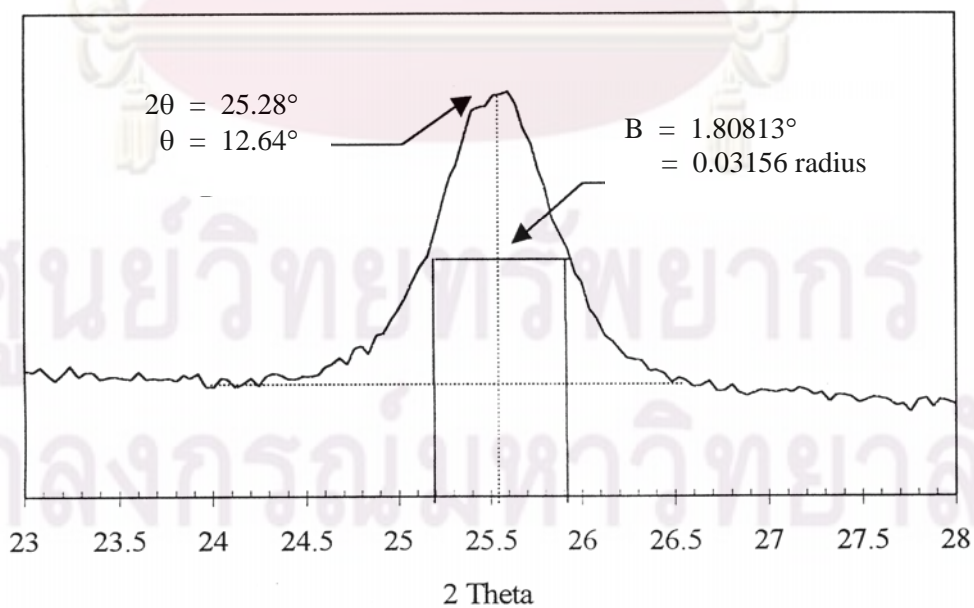$$= 45.40 \text{ Å}$$

$$= 4.5 \text{ nm}$$

Figure A.1 The 101 diffraction peak of TiO_2 for calculation of the crystallite size.
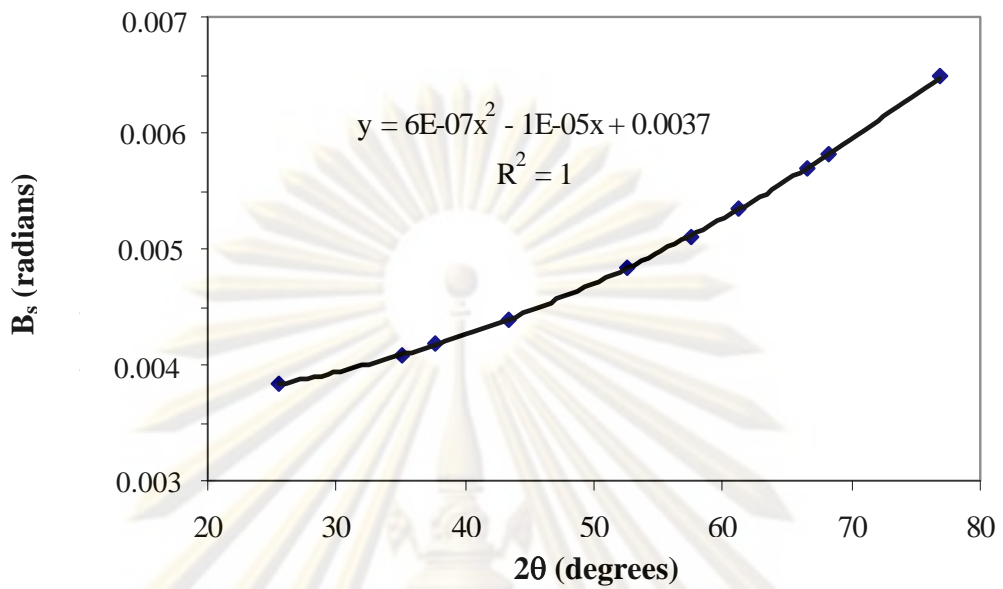
Figure A.2 The plot indicating the value of line broadening due to the equipment. The data were obtained by using α-alumina as standard.

APPENDIX B

DETERMINATION OF LATTICE PARAMETERS
OF TITANIUM DIOXIDE

Interplanar spacing (d-spacing) can be calculated from the Bragg's law according to Equation B.1;

$$2d_{hkl} \sin\theta = n\lambda \qquad\qquad (B.1)$$

where d_{hkl} is the distance between crystal planes (Å)

   θ is the diffraction angle (degree)

   λ is X-ray wavelength (1.5418 Å for Cu K_α)

   a, b and c are lattice parameters (for anatase, $a = b \neq c$) (Å)

   (h k l) is Miller's index

So, at a fixed-wavelength (controlled by the XRD machine: target, filter, etc.) for a certain value of d-spacing (characteristic of samples). After obtaining the d-spacing of each plane, a-cell and c-cell of lattice parameter in tetragonal crystal system (see Figure B.1) can be calculated according to Equation B.2;

$$d_{hkl} = \frac{a}{[h^2 + k^2 + l^2(\frac{a^2}{c^2})]^{\frac{1}{2}}} \qquad\qquad (B.2)$$
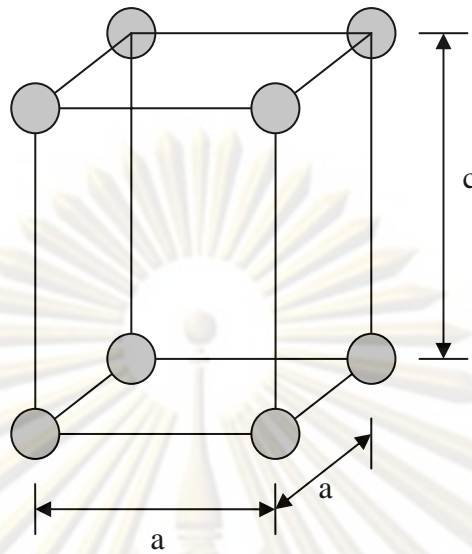
Figure B.1 Tetragonal crystal structure of titanium dioxide.

Example: Calculation the lattice parameter of titanium dioxide

To calculation the lattice parameter of anatase TiO_2, we select the (101) and (200) plane for determine the d-spacing values. The steps for calculation as followed below;

1. From the diffraction patterns of 0.0% Ag-TiO_2, the diffraction angle of anatase TiO_2 in (101) and (200) plans were 25.38° and 48.26° respectively. So, substitute in Equation (B.1);

$$d_{101} = \frac{(1)(1.5418)}{(2)[\sin(25.38/2)]} = 3.5093 \text{ Å}$$

$$d_{200} = \frac{(1)(1.5418)}{(2)[\sin(48.26/2)]} = 1.8857 \text{ Å}$$

2. The d-spacing of (200) plane is used to determine a-cell parameter;

$$a \quad = \quad (2)(d_{200}) \quad = \quad (2)(1.8857) \quad = \quad 3.7714 \text{ Å}$$

3. The c-cell parameter can be determined from Equation (B.2);

$$c \quad = \quad (-\frac{(d_{101})^2 (a)^2}{((d_{101})^2 - (a)^2)})^{1/2}$$

$$= \quad (-\frac{(3.5093)^2 (3.7714)^2}{((3.5093)^2 - (3.7714)^2)})^{1/2}$$

$$= \quad 9.5792 \text{ Å}$$

3. So, the crystal volume of TiO_2 can be calculated from;

$$\text{Crystal volume} = (a)^2(c)$$

$$= (3.7714)^2(9.5792)$$

$$= 136.2530 \text{ Å}^3$$

Table B.1 Summary of lattice parameters and crystal volume from XRD analysis.

Sample	d_{101} (Å)	d_{200} (Å)	a-cell parameter (Å)	c-cell parameter (Å)	Crystal volume (Å)
0.0% Ag-TiO$_2$	3.5093	1.8857	3.7714	9.5792	136.2530
0.1% Ag-TiO$_2$	3.5174	1.8872	3.7744	9.6991	138.1732
0.5% Ag-TiO$_2$	3.5257	1.8879	3.7759	9.8492	140.4217
1.0% Ag-TiO$_2$	3.5120	1.8872	3.7744	9.5864	136.5678
3.0% Ag-TiO$_2$	3.5147	1.8857	3.7714	9.6917	137.8535
5.0% Ag-TiO$_2$	3.5202	1.8879	3.7759	9.7315	138.7439
0.0% W-TiO$_2$	3.5120	1.8924	3.7847	9.4221	134.9631
0.1% W-TiO$_2$	3.5147	1.8983	3.7966	9.2947	133.9767
0.5% W-TiO$_2$	3.5093	1.8983	3.7966	9.1953	132.5441
1.0% W-TiO$_2$	3.5065	1.8953	3.7907	9.2314	132.6467
1.5% W-TiO$_2$	3.5120	1.8961	3.7921	9.3099	133.8805
0.0% Cu-TiO$_2$	3.5093	1.8857	3.7714	9.5792	136.2530
0.1% Cu-TiO$_2$	3.5174	1.8946	3.7892	9.4589	135.8094
0.5% Cu-TiO$_2$	3.5120	1.8909	3.7818	9.4681	135.4106
1.0% Cu-TiO$_2$	3.5229	1.8916	3.7832	9.6640	138.3210
5.0% Cu-TiO$_2$	3.5257	1.8938	3.7877	9.6467	138.3976
0.0% Mo-TiO$_2$	3.5038	1.8894	3.7788	9.3562	133.6014
0.1% Mo-TiO$_2$	3.5147	1.8983	3.7966	9.2947	133.9767
0.3% Mo-TiO$_2$	3.5038	1.8938	3.7877	9.2248	132.3440
0.5% Mo-TiO$_2$	3.5120	1.8953	3.7907	9.3320	134.0930
0.7% Mo-TiO$_2$	3.5120	1.8894	3.7788	9.5149	135.8668
1.0% Mo-TiO$_2$	3.5079	1.8938	3.7877	9.2999	133.4212

APPENDIX C

DATA AND CALCULATION OF ACID SITE

Table C.1 Reported total peak area from Micromeritrics Chemisorb 2750

Sample	Weight (g)	Total peak area
0.0% Ag-TiO$_2$	0.1026	5.2705
0.1% Ag-TiO$_2$	0.1056	5.3526
0.5% Ag-TiO$_2$	0.1001	5.1601
1.0% Ag-TiO$_2$	0.1010	4.8433
3.0% Ag-TiO$_2$	0.1011	4.5922
5.0% Ag-TiO$_2$	0.1011	4.2448
0.0% W-TiO$_2$	0.1025	3.9456
0.1% W-TiO$_2$	0.1020	4.2178
0.5% W-TiO$_2$	0.1011	4.4608
1.0% W-TiO$_2$	0.1023	4.7393
1.5% W-TiO$_2$	0.1004	5.4885
0.0% Cu-TiO$_2$	0.1039	4.4569
0.1% Cu-TiO$_2$	0.1021	4.9759
0.5% Cu-TiO$_2$	0.1010	4.4983
1.0% Cu-TiO$_2$	0.1009	4.4389
5.0% Cu-TiO$_2$	0.1002	5.2699
0.0% Mo-TiO$_2$	0.1010	4.6309
0.1% Mo-TiO$_2$	0.1020	3.8995
0.3% Mo-TiO$_2$	0.1018	3.7916
0.5% Mo-TiO$_2$	0.1009	3.8633
0.7% Mo-TiO$_2$	0.1016	3.9885
1.0% Mo-TiO$_2$	0.1011	4.1324

Example: Calculation of total acid sites.

1. Conversion of total peak area (see Table C.1) to peak volume;

Conversion from Micrometrics Chemisorb 2750 is equal 77.5016 mL/ unit area. Therefore, total peak volume is derived from

$$
\begin{aligned}
\text{Total peak volume} \quad &= \quad 77.5016 \text{ x total peak area} \\
&= \quad 77.5016 \text{ x } 5.2705 \\
&= \quad 397.9304 \text{ mL}
\end{aligned}
$$

2. Calculation for adsorbed volume of 15% NH_3;

$$
\begin{aligned}
\text{Adsorbed volume of 15\% } NH_3 &= \quad 0.15 \text{ x total peak volume} \\
&= \quad 0.15 \text{ x } 397.9304 \text{ mL} \\
&= \quad 59.6896 \text{ mL}
\end{aligned}
$$

3. Calculation of total acid sites;

$$
\text{Total acid sites} \quad = \quad \frac{(absorbed\ volume, ml) \times 101.325\ kPa}{(8.314\,\frac{Pa \cdot ml}{K \cdot \mu mol}) \times 298\ K \times (weight\ of catalyst, g)}
$$

For pure titania sample, 0.1026 g of this sample was measured, therefore

$$
\begin{aligned}
\text{Total acid sites} \quad &= \quad \frac{59.6896\ mL \times 101.325\ kPa}{(8.314\,\frac{Pa \cdot mL}{K \cdot \mu mol}) \times 298 K \times (0.1026\ g)} \\
&= \quad 23792.57\ \mu mol\ NH_3 / g \\
&= \quad 23.79\ mmol\ NH_3 / g
\end{aligned}
$$

APPENDIX D

CALCULATION OF OPTICAL BAND GAP ENERGY

In the visible region, the absorption coefficient (α) is influenced by the scattering of light on the surface roughness (being a transparent material in this domain, the light scattering dominates over the absorption), and it can be obtained from the approximate relation according to Equation D.1 (Mardare et al., 2000)

$$T = \frac{(1-R)^2 \exp(-\alpha(\lambda)d)}{1-R^2 \exp(-2\alpha(\lambda)d)} \tag{D.1}$$

where T is the transmittance

        R is the reflectance

        d is the thickness of the film

        λ is the wavelength

        α is the absorption coefficient

However, at shorter wavelength close to the optical band gap, the scattering losses are dominated by the fundamental absorption and the following relation is often used according to Equation D.2 (Djaoued et al., 2007)

$$\alpha = -2.303 \frac{\log T}{d} \tag{D.2}$$

Above the threshold of fundamental absorption near absorption edge, the dependence of α on incident light energy is known to obey the relation according to Equation D.3

$$\alpha h\upsilon = \alpha_0 (h\upsilon - E_g)^n \tag{D.3}$$

$h\upsilon$ is the photon energy

α_0 is a constant which not depend on photo energy

E_g is optical band gap energy of film

n is characteristic value

The value of n may be taken $n = 2$, a characteristic value for the indirect allowed transition which dominates over the optical absorption (Mardare et al., 2000). Substitute Equation D.2 into D.3, so Equation D.4 can be became

$$(-2.303h\upsilon\log T)^{\frac{1}{2}} = B(h\upsilon - E_g) \qquad\qquad (D.4)$$

where B is a constant. The graph of $(-2.303h\upsilon\log T)^{\frac{1}{2}}$ versus $h\upsilon$ will present a linear part that can be extrapolated to zero, leading to the band gap energy (E_g).

Example: Calculation of optical band gap energy of the films

Figure D.1 shows the graph of $(-2.303h\upsilon\log T)^{\frac{1}{2}}$ versus $h\upsilon$ of various W-TiO$_2$ films. After the linear part were extrapolated, the band gap energy were obtained and results were listed in Table D.1
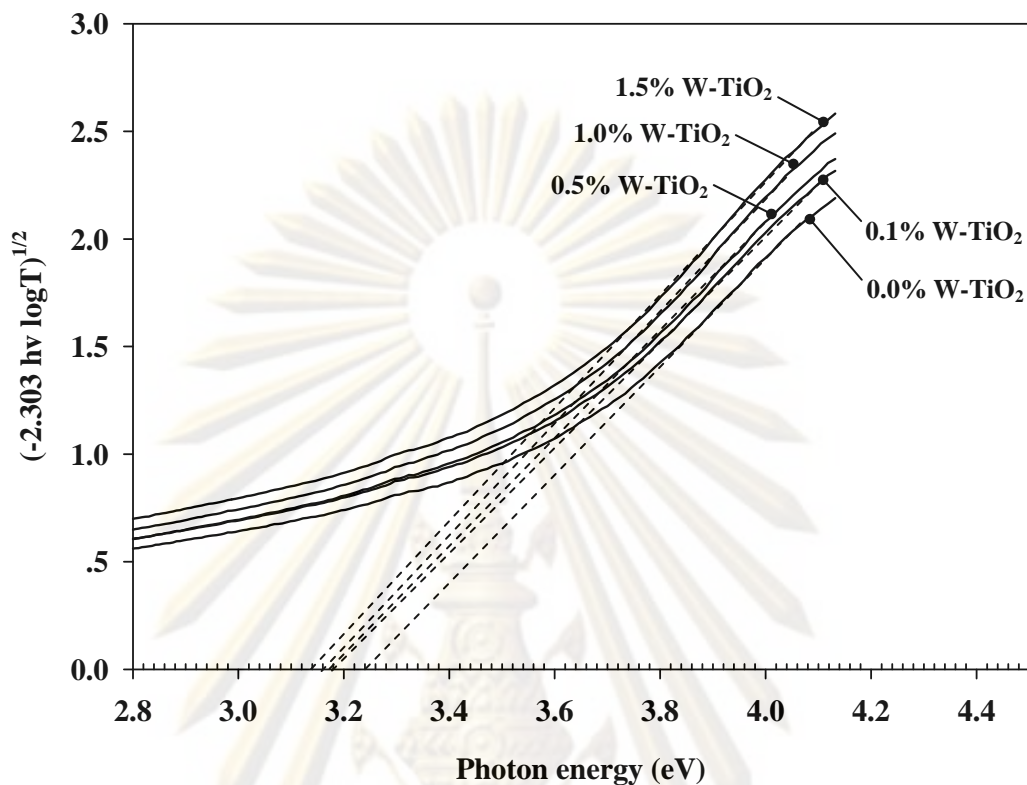
Figure D.1 Optical band gap energy of W-TiO$_2$ films

Table D.1 Band gap energy of various W-TiO$_2$ films

Samples	Band gap energy (eV)
0.0% W-TiO$_2$	3.24
0.1% W-TiO$_2$	3.18
0.5% W-TiO$_2$	3.17
1.0% W-TiO$_2$	3.16
1.5% W-TiO$_2$	3.14

APPENDIX E

CALCULATION OF THE CONTACT ANGLE

The contact angle of sample was calculated from height and radius of water droplet using trigonometry formula according to Equation E.1

$$Contact\ angle\ =\ 2\arctan\frac{h}{r} \qquad\qquad (E.1)$$

where h is water droplet height

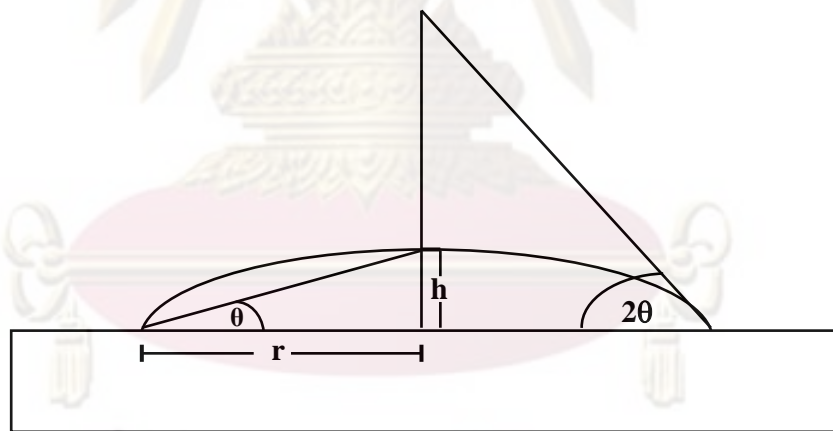r is water droplet radius

2θ is contact angle

Figure E.1 The shape and dimension of water droplet on the surface.

LIST OF PUBLICATION

Piyaphong Phromsalee and Akawat Sirisuk. Effect of silver loading on photo-induced hydrophilicity of titanium dioxide thin films. 2nd SUT graduate conference, Suranaree University of Technology, January 21-22, 2009.

VITA

Mr. Piyaphong Phromsalee was born on October 20, 1984 in Rayong province, Thailand. He received the Bachelor Degree of Chemical Engineering from Faculty of Engineering, Srinakharinwirot University, in 2007. He pursued his Master's study at Center of Excellence on Catalysis and Catalytic Reaction Engineering, Department of Chemical Engineering, Faculty of Engineering, Chulalongkorn University in June, 2007.